

Editorial corner – a personal view

Plastics and composites based on renewable resources: end-of-life recycling and recovery issues

*P. Krawczak**

Department of Polymers and Composites Technology & Mechanical Engineering, Ecole des Mines de Douai,
941 rue Charles Bourseul, BP 10838, 59508 Douai, France

Environmental concerns undoubtedly drive the ‘greening’ of the plastics and composites industry. Thermoplastics and thermosetting resins from renewable resources derived from plants or micro-organisms, eventually reinforced with natural fillers or fibres, are developing significantly and the demand is increasing steadily. The world-wide scientific and industrial community is struggling for many years to improve industrial processability and properties of polylactide (PLA), polyhydroxyalkanoate (PHA), thermoplastic starch, soybean oil based polymers, etc. Applications in the packaging or transportation industries are more and more numerous. Many factors have contributed to the market acceptance of such green plastics and composites: Reduced dependence on fossil-fuel, reduced environmental pollution during their production (i.e. less CO₂ and greenhouse gases in the atmosphere), fight against ‘visual’ pollution of landscape (as ‘by product’ of land-filling with post consumer goods and scraps) and oceans.

Many biobased materials are biodegradable or compostable and therefore theoretically offer an outlet for overflowing solid-waste streams. Land-filling would not necessarily be avoided, but the degradation time is expected to be highly reduced. Great!

One should however keep in mind that recovery and recycling of post-consumer and post-industrial plastic and composites goods, waste and scraps are now well structured in the packaging and automotive

industries. Bottles and containers are collected, cars are dismantled, plastics and composites sorted and reground to be further used as fillers or commingled with virgin materials to manufacture new goods. Similar efforts are currently made in other industrial sectors (aeronautics, yachting/marine ...). ‘Green’ labels are awarded to petroleum-based products which warrant recycling or recyclability.

Unfortunately the green plastics, resins and composites based on renewable resources cannot currently be treated by the existing recycling/recovery plants. Paradoxically, this might be a brake to the further industrial development of these materials.

The end-of-life treatment of plastics and composites based on renewable resources has to be considered urgently as biodegradability and renewability does not necessarily mean eco-friendliness. Otherwise the benefit gained from production and usage of these ‘new’ materials will be lost on the long term.



Prof. Dr. Patricia Krawczak
Member of International Advisory Board

*Corresponding author, e-mail: krawczak@ensm-douai.fr
© BME-PT and GTE

Self healing in polymers and polymer composites. Concepts, realization and outlook: A review

Y. C. Yuan¹, T. Yin¹, M. Z. Rong², M. Q. Zhang^{2*}

¹Key Laboratory for Polymeric Composite and Functional Materials of Ministry of Education, OFCM Institute, School of Chemistry and Chemical Engineering, Zhongshan University, Guangzhou 510275, P. R. China

²Materials Science Institute, Zhongshan University, Guangzhou 510275, P. R. China

Received 10 February 2008; accepted in revised form 21 February 2008

Abstract. Formation of microcracks is a critical problem in polymers and polymer composites during their service in structural applications. Development and coalescence of microcracks would bring about catastrophic failure of the materials and then reduce their lifetimes. Therefore, early sensing, diagnosis and repair of microcracks become necessary for removing the latent perils. In this context, the materials possessing self-healing function are ideal for long-term operation. Self-repairing polymers and polymer composites have attracted increasing research interests. Attempts have been made to develop solutions in this field. The present article reviews state-of-art of the achievements on the topic. According to the ways of healing, the smart materials are classified into two categories: (i) intrinsic self-healing ones that are able to heal cracks by the polymers themselves, and (ii) extrinsic in which healing agent has to be pre-embedded. The advances in this field show that selection and optimization of proper repair mechanisms are prerequisites for high healing efficiency. It is a challenging job to either invent new polymers with inherent crack repair capability or integrate existing materials with novel healing system.

Keywords: smart polymers, polymer composites, self-healing, cracks

1. Introduction

Polymers and polymer composites have been widely used in tremendous engineering fields because of their advantages including light weight, good processibility, chemical stability in any atmospheric conditions, etc. However, long-term durability and reliability of polymeric materials are still problematic when they serve for structural application [1]. Exposure to harsh environment would easily lead to degradations of polymeric components. Comparatively, microcracking is one of the fatal deteriorations generated in service, which would bring about catastrophic failure of the materials and hence significantly shorten lifetimes of the structures.

Since the damages deep inside materials are difficult to be perceived and to repair in particular, the materials had better to have the ability of self-healing. In fact, many naturally occurring portions in animals and plants are provided with such function [2–6]. In the case of healing of a skin wound, for example, the defect is temporarily plugged with a fibrin clot, which is infiltrated by inflammatory cells, fibroblasts, and a dense capillary plexus of new granulation tissue. Subsequently, proliferation of fibroblasts with new collagen synthesis and tissue remodeling of the scar become the key steps. For healing of a broken bone, similar processes are conducted, including internal bleeding forming a fibrin clot, development of unorganized fiber mesh, calcification of fibrous cartilage, conversion of cal-

*Corresponding author, e-mail: ceszmq@mail.sysu.edu.cn
© BME-PT and GTE

cification into fibrous bone and lamellar bone. Clearly, the natural healing in living bodies depends on rapid transportation of repair substance to the injured part and reconstruction of the tissues. Having been inspired by these findings, continuous efforts are now being made to mimic natural materials and to integrate self-healing capability into polymers and polymer composites. The progress has opened an era of new intelligent materials.

On the whole, researches in this field are still in the infancy. More and more scientists and companies are interested in different aspects of the topic. Innovative measures and new knowledge of the related mechanisms are constantly emerging. Therefore, it might be the right time to review the attempts carried out so far in different laboratories in the world. According to the ways of healing, self-healing polymers and polymer composites can be classified into two categories: (i) intrinsic ones that are able to heal cracks by the polymers themselves, and (ii) extrinsic in which healing agent has to be pre-embedded.

2. Intrinsic self-healing

The so-called intrinsic self-healing polymers and polymer composites are based on specific performance of the polymers and polymeric matrices that enables crack healing under certain stimulation (mostly heating). Autonomic healing without external intervention is not available in these materials for the time being. As viewed from the predominant molecular mechanisms involved in the healing processes, the reported achievements consist of two modes: (i) physical interactions, and (ii) chemical interactions.

2.1. Self-healing based on physical interactions

Compared to the case of thermosetting polymers, crack healing in thermoplastic polymers received more attention at an earlier time. Wool and co-workers systematically studied the theory involved [7, 8]. They pointed out that the healing process goes through five phases: (i) surface rearrangement, which affects initial diffusion function and topological feature; (ii) surface approach, related to healing patterns; (iii) wetting, (iv) diffusion, the main factor that controls recovery of mechanical

properties, and (v) randomization, ensuring disappearance of cracking interface. In addition, Kim and Wool [9] proposed a microscopic model for the last two phases on basis of reptation model that describes longitudinal chain diffusion responsible for crack healing.

Accordingly, Jud and Kaush [10] tested crack-healing behavior in a series of poly(methyl methacrylate) (PMMA) and poly(methyl methacrylate-co-methyl ethylacrylate) (MMA-MEA copolymer) samples of different molecular weights and degrees of copolymerization. They induced crack healing by heating samples above the glass transition temperature under slight pressure. It was found that full resistance was regained during short term loading experiments. The establishment of mechanical strength should result from interdiffusion of chains and formation of entanglements for the glassy polymer [11]. Wool [12] further suggested that the recovery of fracture stress is proportional to $t^{1/4}$ (where t is the period of heating treatment). Jud *et al.* [13] also performed re-healing and welding of glassy polymers (PMMA and styrene-acrylonitrile copolymer (SAN)) at temperatures above the glass transition temperatures, and found that the fracture toughness, K_{Ii} , in the interface increased with contact time, t , as $K_{Ii} \propto t^{1/4}$ as predicted by the diffusion model.

It is worth noting that whereas craze healing occurs at temperature above and below the glass transition temperature [14], crack healing happens only at or above the glass transition temperature [15]. In order to reduce the effective glass transition temperature of PMMA, Lin *et al.* [16] and Wang *et al.* [17] treated PMMA with methanol and ethanol, respectively. They reduced the glass transition temperature to a range of 40–60°C, and found that there were two distinctive stages for crack healing: the first one corresponding to the progressive healing due to wetting, while the second related to diffusion enhancement of the quality of healing behavior.

Besides simple heating induced healing, thermo-mechanical healing is valid for some specific polymers, like poly(ethylene-co-methacrylic acid) (EMAA) copolymers [18]. EMAA films prove to be able to heal upon ballistic puncture and sawing damages. This occurs through a heat generating frictional process, which heats the polymer to the viscoelastic melt state and provides the ability to rebond and repair damage. In contrast, low speed

friction event fails to produce sufficient thermal energy favorable to healing. As a result, thermomechanical healing is not active in the material.

Unlike thermoplastics, heating induced healing of thermosetting polymers depends on crosslinking of unreacted groups. Healing of epoxy, for instance, has to proceed above the glass transition temperature [19]. Then, the molecules at the cracking surfaces would interdiffuse and the residual functional groups react with each other. A 50% recovery of impact strength can thus be obtained [20]. During the repair study of vinyl ester resin, Raghavan and Wool reported critical strain energy release rate, G_{IC} , for the interfaces after crack healing (i.e. annealing above the glass transition temperature) is 1.7% of the virgin value. Lower crosslink density favors the repair effect [21].

Thermoplastic/thermosetting semi-interpenetrating network is factually a material associated with repeatable self-healing ability. The group of Jones introduced a soluble linear polymer to a thermosetting epoxy resin [22–24]. The selected thermoplastic is poly(bisphenol-A-co-epichlorohydrin), which is highly compatible with the matrix diglycidyl ether of bisphenol-A based resin. Upon heating a fractured resin system, the thermoplastic material would mobilize and diffuse through the thermosetting matrix, with some chains bridging closed cracks and thereby facilitating healing. When this healable resin was compounded with crossply glass fiber, effective healing of composites transverse cracks and delamination has been demonstrated. The requirements for such thermal diffusion of a healing agent were summarized as follows [23]. (i) The healing agent should be reversibly bonded (e.g. through hydrogen bonding) to the crosslinked network of the cured resin below the minimum healing temperature to limit its effect on thermomechanical properties. (ii) The healing agent should become mobile above this minimum healing temperature so that it can diffuse across a hairline crack, such as a transverse crack, to provide a recovery in strength. (iii) The addition of the linear chain molecule should not significantly reduce the thermomechanical properties of the resin matrix.

2.2. Self-healing based on chemical interactions

In fact, cracks and strength decay might be caused by structural changes of atoms or molecules, like chain scission. Therefore, inverse reaction, i.e. recombination of the broken molecules, should be one of the repairing strategies. Such method does not focus on cracks healing but on ‘nanoscopic’ deterioration. One example is polycarbonate (PC) synthesized by ester exchange method. The PCs were treated in a steam pressure cabin at 120°C prior to the repair [25]. As a result, molecular weight of the PCs dropped by about 88 to 90%. After drying them in a vacuum cabin, the repairing treatment was done in an oven at 130°C with N₂ atmosphere under reduced pressure. The reduced tensile strength due to the deterioration treatment can thus be gradually recovered. The repairing mechanism was considered as the following procedures. Firstly the carbonate bond was cut by hydrolysis, and then the concentration of the phenoxy end increased after deterioration. The (–OH) end-group on the chain was substituted by sodium ion. The (–ONa) end might attack a carbonate bond at the end of one of the other chains, leading to recombination of these two chains with the elimination of the phenol from PC (Figure 1). The repairing reaction was accelerated by weak alkaline, such as sodium carbonate. It suggested that two conditions are required for the PC to recombine the polymer chains. One is the chemical structure of the chain end and the other is the catalyst (Na₂CO₃) for acceleration of the reaction.

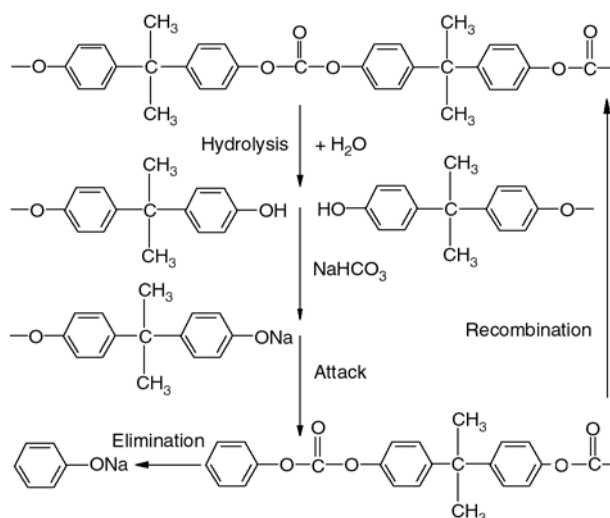


Figure 1. Hydrolysis and recombination reaction of PCs with the catalyst of NaCO₃

Another example is poly(phenylene ether) (PPE) in which the repairing agent was regenerated by oxygen [26]. The polymer chain of the PPE was cut by a deterioration factor (such as heat, light, and external mechanical force) to produce a radical on the end of the scission chain. Subsequently, a hydrogen donor stabilized the radical. The catalyst existing in the system, Cu (II), would react with each end of the scission chains to form a complex. Then, the chains combined by eliminating two protons from the ends, and the copper changed from Cu (II) to Cu (I). Afterward, two Cu (I) reacted with an oxygen molecule to be oxidized to Cu (II), and an oxygen ion reacted with two protons to form a water molecule that evaporated from the specimen.

The above examples show that PC or PPE might be probably designed as a self-repairing material by means of the reversible reaction. The deterioration is expected to be minimized if the recovery rate is the same as the deterioration rate. However, the systems in these studies are not sufficient for construction of real self-repairing composites because the recovery of the broken molecules needs higher temperature and other rigorous conditions. A much more effective catalyst should be found, which is able to active the recombination of degraded oligomers at room temperature.

Thermally reversible crosslinking behavior has been known for quite a while. Wudl *et al.* combined this with the concept of ‘self-healing’ in making healable polymers [27, 28]. They synthesized highly cross-linked polymeric materials with multifuran and multi-maleimide via Diels-Alder (DA) reaction. At temperatures above 120°C, the ‘intermonomer’ linkages disconnect (corresponding to retro-DA reaction) but then reconnect upon cooling (i.e. DA reaction). This process is fully reversible and can be used to restore fractured parts of the polymers. The polymers are transparent and possess mechanical properties comparable to commercial epoxy and unsaturated polyester. In principle, an infinite number of crack healing is available without the aid of additional catalysts, monomers and special surface treatment.

In a latter work by Liu and Hsieh [29], Wudl’s approach was modified. The multifunctional furan and maleimide compounds were prepared in simple routes, using epoxy compounds as precursors. The furan and maleimide monomers could be therefore considered as epoxy-based compounds, so as to

incorporate the advantage characteristics of epoxy resins, including solvent and chemical resistance, thermal and electrical characters, and good adherence, to their corresponding cured polymers. Besides, Liu and Chen prepared polyamides possessing furan pendent groups (PA-F) from reacting furfuryl amine with maleimide containing polyamides (PA-MI) via a Michael addition reaction [30]. Thermally reversible cross-linked polyamides were obtained from PA-MI and PA-F polyamides by means of DA and retro-DA reactions. The thermally reversible cross-linked polyamides also exhibited a self-repairing property as well as the ability of mechanical property recovery. To quantify the degree of structural restoration after damages have been repaired, characterization of healing efficiency is necessary but no specific testing standard is available now. Different testing procedures sometimes give different results [23]. When Wudl’s group measured healing efficiency of their thermally reversible crosslinked polymers, fracture toughness from compact tension (CT) tests was used [27]. Values for the original and healed fracture toughness were determined by the propagation of the starter crack along the middle plane of the specimen at the critical load. In consideration of the difficulties in (i) precise registration of the fracture surface and (ii) protection of pre-notching, Plaisted and Nemat-Nasser [31] applied double cleavage drilled compression (DCDC) to evaluate mending efficiency of the reversibly cross-linked polymer based on Diels-Alder cycloaddition. The testing geometry allowed for controlled incremental crack growth so that the cracked sample remained in one piece after the test, improving ability to realign the fracture surfaces prior to healing.

3. Extrinsic self-healing

In the case of extrinsic self-healing, the matrix resin itself is not a healable one. Healing agent has to be encapsulated and embedded into the materials in advance. As soon as the cracks destroy the fragile capsules, the healing agent would be released into the crack planes due to capillary effect and heals the cracks. In accordance with types of the containers, there are two modes of the repair activity: (i) self-healing in terms of healant loaded pipelines, and (ii) self-healing in terms of healant loaded microcapsules. Taking the advantages of crack trig-

gered delivery of healing agent, manual intervention (e.g. heating that used to be applied for intrinsic self-healing) might be no longer necessary.

3.1. Self-healing in terms of healant loaded pipelines

3.1.1. Hollow glass tubes and glass fibers

The core issue of this technique lies in filling the brittle-walled vessels with polymerizable medium, which should be fluid at least at the healing temperature. Subsequent polymerization of the chemicals flowing to the damage area plays the role of crack elimination. Dry first identified the potential applicability of hollow glass tubes [32–35]. Similar approach was adopted by Motuku *et al.* [36] and Zhao *et al.* [37]. Because the hollow glass capillaries have diameters (on millimeter scale) much larger than those of the reinforcing fibers in composites, they have to act as initiation for composites failure [38]. Instead, Bleay *et al.* employed hollow glass fiber (with an external diameter of 15 μm and an internal diameter of 5 μm) to minimize the detrimental effect associated with large diameter fibers [38]. Complete filling of healing agent into the tiny tubes was achieved by vacuum assisted capillary action filling technique.

Accordingly, three types of healing system were developed (Figure 2) [32–48]. (i) Single-part adhe-

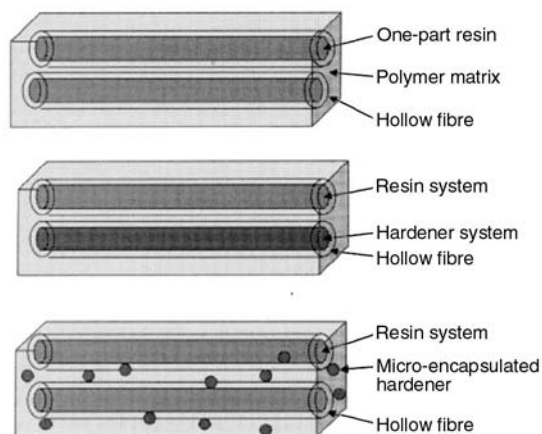


Figure 2. Schematic diagram of repair concept for polymer matrix composites using pre-embedded hollow tubes [38] (Reprinted from Composites Part A: Applied Science and Manufacturing, Vol 32, Bleay S. M., Loader C. B., Hawyes V. J., Humberstone L., Curtis P. T.: A smart repair system for polymer matrix composites, 1767–1776, Copyright (2001), with permission from Elsevier)

sive. All hollow pipettes contained only one kind of resin like epoxy particles (that can be flowable upon heating and then cured by the residual hardener) or cyanoacrylate (that can be consolidated under the induction of air). (ii) Two-part adhesive. In general, epoxy and its curing agent were used in this case. They were filled into neighboring hollow tubes, respectively. (iii) Two-part adhesive. One component was incorporated into hollow tubes and the other in microcapsules.

With the aid of the pre-embedded healing system in hollow pipettes, Motuku and co-workers studied the healing ability of glass fiber/unsaturated polyester composites subjected to low velocity impact [36, 43]. The species of healing agent, characteristic parameters of the hollow pipes (amount, type of tubing materials and spatial distribution), composites panel thickness, and impact energy level were found to be critical to the healing efficiency. Meanwhile, Bleay *et al.* proved that the epoxy based composites reinforced by hollow glass fibers containing solvent diluted two-part epoxy became repairable as assessed by compression after impact test [38].

Recently, Trask *et al.* [47] considered the placement of self-healing hollow glass fibers layers within both glass fibre/epoxy and carbon fibre/epoxy composite laminates to mitigate damage and restore mechanical strength. The hollow fibers were bespoke with diameters between 30 and 100 μm and a hollowness of approximately 50%. The study revealed that after the laminates were subjected to quasi-static impact damage, a significant fraction of flexural strength can be restored by the self repairing effect of a healing resin stored within hollow fibers. More details of such healing system can be found in ref. [44–46, 48]. For example, Pang *et al.* added UV fluorescent dye to the healing resin within the hollow fibers so that bleeding of the repair substance in the composites can be visualized [44].

On the other hand, step type multi-mode quartz optical fiber consisting of hollow fiber, cladding and coating have been successfully applied in smart structures. When the materials were damaged, the pre-embedded optical fibers had to be ruptured leading significant reduction in the output light intensity. This helped to locate the cracked portions. In case the hollow optical fibers were infused with uncured resin and embedded within polymer

composites, real-time monitor, diagnosis and repair of damages would be simultaneously completed. Guided by this idea, Yang and co-workers manufactured glass fiber laminates with self-diagnosis and self-healing functionality, in which ethyl cyanoacrylate served as the healant. Recoveries of initial tensile strength of about 1/3 and initial compressive strength of about 2/3 proved the feasibility of this approach [49–51].

Property matching is important for hollow glass fibers/matrix polymer pairs, which decides breakage of the hollow fibers and release of healing agent. Zhao *et al.* showed that for the epoxy/polyamide compounds with healing agent loaded hollow plastic fiber, the plastic tubes did not fracture even when the matrix was completely broken [37]. No healing effect could be observed as a result. One of the possible solutions of this problem lies in covering the hollow repair fiber with a thin polymeric layer [39, 52]. By tuning species and thickness of the polymer coating, one might be able to control fracture mode and time of the containers, giving out healant at the right moment.

Flowability of the released healing agent inside materials to be healed is another problem that might be encountered in practice. Besides diffusivity of the healing agent itself, internal pressure within the repair tubes should also be considered. Having carefully studied dependences of the spillage of healing fluid and the repair area, Zhao and co-workers indicated that 95% of the crack planes can be healed when the internal pressure reached 0.2 MPa [37].

3.1.2. Three-dimensional microvascular networks

In conventional extrinsic self-healing composites it is hard to perform repeated healing, because rupture of the embedded healant-loaded containers would lead to depletion of the healing agent after the first damage. To overcome this difficulty, Toohey *et al.* proposed a self-healing system consisting of a three-dimensional microvascular network capable of autonomously repairing repeated damage events [53]. Their work mimicked architecture of human skin. When a cut in the skin triggers blood flow from the capillary network in the dermal layer to the wound site, a clot would rapidly form, which serves as a matrix through which cells

and growth factors migrate as healing ensues. Owing to the vascular nature of this supply system, minor damage to the same area can be healed repeatedly. The 3D microvascular networks were fabricated by deposition of fugitive ink (a mixture of Vaseline/microcrystalline wax (60/40 by weight)) in terms of direct-write assembly [54] through a cylindrical nozzle. Then, the yielded multilayer scaffold was infiltrated with epoxy resin. When the resin was consolidated, structural matrix was obtained. With the help of heating and light vacuum, the fugitive ink was removed and 3D microvascular networks were created. By inserting a syringe tip into an open channel at one end of the microvascular networks, fluidic polymerizable healing agent was injected into the networks.

The healing chemistry of this method used ring-opening metathesis polymerization of dicyclopentadiene (DCPD) monomer by Grubbs' catalyst, benzylidenebis(tricyclohexylphosphine) dichlororuthenium, which was used successfully in microencapsulated composites [55]. In the crack plane, the healing agent interacted with the catalyst particles in the composites to initiate polymerization, rebonding the crack faces autonomously. After a sufficient time period, the cracks were healed and the structural integrity of the coating was restored. As cracks reopened under subsequent loading, the healing cycle was repeated.

By means of four-point bending configuration monitored with an acoustic-emission sensor, the above approach proved to be feasible. The authors imagined extending this approach further to integrate pumps, valves and internal reservoirs, as well as to introduce new functionalities, including self-diagnosis or self-cooling, through the circulation of molecular signals, coolants or other species [53].

To provide theoretical understanding how to vascularize a self-healing composite material so that healing fluid reaches all the crack sites that may occur randomly through the material, Bejana *et al.* studied the network configuration that is capable of delivering fluid to all the cracks the fastest [56]. When crack site dimension and total volume of the channels were fixed, it was argued that the network must be configured as a grid and not as a tree. In addition, it is beneficial to use a grid structure that has two channel sizes, D_1 and D_2 , provided that the ratio D_1/D_2 is optimized. The crack-filling time can

be reduced to 50% of the time required when the grid contains channels of only one size.

3.2. Self-healing in terms of healant loaded microcapsules

The principle of this approach resembles the afore-said pipelines but the containers for storing healing agent are replaced by fragile microcapsules. Because the technique of microencapsulation has been rapidly developed since its emergency in 1950s [57–59] and mass production of microcapsules can be easily industrialized, self-healing composites might be thus used in practice accordingly. Jung *et al.* prepared a self-healing polyester composite with pre-embedded polyoxymethylene urea (PMU) microspheres [60]. The crack repair agent is mostly composed of styrene monomers and high molecular weight polystyrene. The latter helps to lower the rate of diffusion of styrene or diethenyl benzene into polyester matrix. The system of 23% polystyrene ($M_n = 2.5 \cdot 10^5$), 76.99% styrene and a trace amount of inhibitor proved to offer the optimum healing efficiency. Jung *et al.* also tried to utilize epoxide monomer loaded PMU microcapsules for rebinding the cracked faces in polyester matrix [60]. Solidification of the epoxy resin (i.e. the repair action) was triggered by the naturally occurring functional sites or embedded amine in the composites. In a latter work by White *et al.* [61], it was considered that the method was not feasible as the amine groups did not retain sufficient activity. Zako *et al.* proposed an intelligent material system using 40% volume fraction unmodified epoxy particles to

repair microcracks and delamination damage in a glass/epoxy composite laminate [62]. By heating to 120°C, the embedded epoxy particles (~50 μm) would melt, flow to the crack faces and repair the damage with the help of the excessive amine in the composite. In addition to the poor activity of the amine as mentioned above, manual intervention (i.e. heating) was necessary in this case.

We reported a two-component healant consisting of epoxy-loaded microcapsules as the polymerizable part and 2-methylimidazole/CuBr₂ complex (CuBr₂(2-MeIm)₄) as the latent hardener, which was pre-dispersed in composites' matrix to fabricate self-healing composites [63]. As soon as cracks destroyed the capsules, the epoxy oligomer would be released into the crack planes due to capillary effect and cured under initiation of the latent hardener at a temperature ranging from 130 to 180°C. The features of this healing system lie in the following. (i) When the healing agent is applied to epoxy based composites, the miscibility between the crack adhesive and matrix is guaranteed because of identity of their species. (ii) The latent hardener possesses long-term stability and is hardly affected by the surrounding environment [64, 65]. Moreover, it can be well pre-dissolved in uncured composites' matrix, leading to homogenous distribution of the reagent on the molecular scale. Thus the epoxy released from the ruptured microcapsules might meet the latent hardener everywhere (Figure 3). The two-component healant is able to take effect in the woven glass fabric/epoxy composite laminates [63, 66].

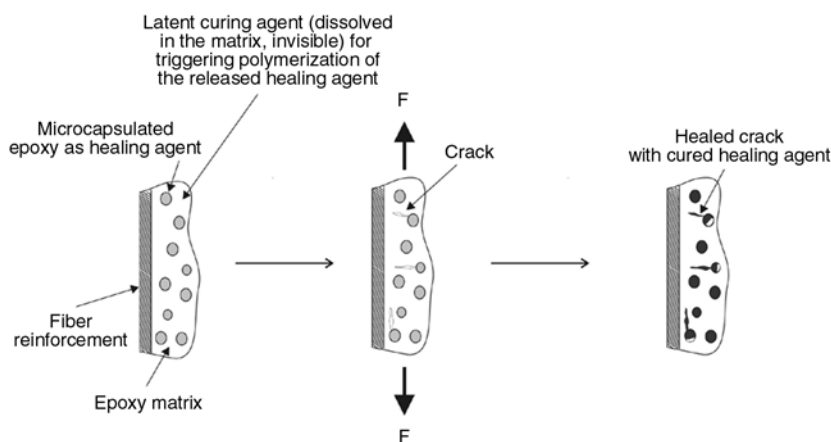


Figure 3. Schematic drawing of the principle of self-healing epoxy based laminates with epoxy loaded microcapsules and latent hardener [63] (Reprinted from Composites Science & Technology, Vol 67, Yin T., Rong M. Z., Zhang M. Q., Yang G. C.: Self-healing epoxy composites – Preparation and effect of the healant consisting of microencapsulated epoxy and latent curing agent, 201–212, Copyright (2007), with permission from Elsevier)

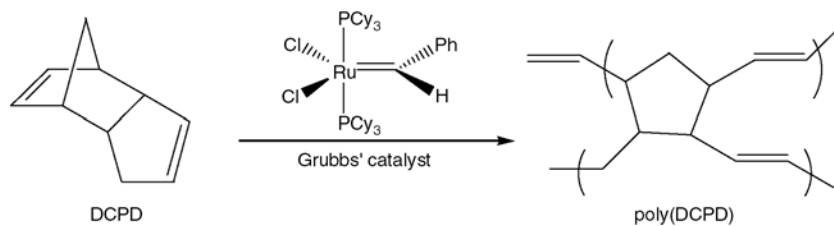


Figure 4. Ring opening metathesis polymerization of DCPD

The group of White *et al.*, the pioneer in developing self-healing polymeric materials, systematically investigated self-healing strategy based on ring opening metathesis polymerization (ROMP) of microencapsulated dicyclopentadiene (DCPD) and reported a series of important findings [55, 67–78]. Healing is triggered when damage in the form of a crack ruptures the microcapsules, causing DCPD to be released into the crack plane where it comes in contact and mixes with the pre-embedded Grubbs' catalyst (Figure 4). For increasing catalysis efficiency, the catalyst was encapsulated by wax and recrystallized, respectively [70, 71]. Delamination damage in woven glass/epoxy composites was found to be repaired by the healing agent [72, 73]. In addition, fatigue crack growth in epoxy can also be retarded by the released fluid [74–76].

Effect of DCPD loaded microcapsule size on the performance of self-healing polymers was studied [78]. Rule *et al.* indicated that the amount of liquid that microcapsules deliver to a crack face changed linearly with microcapsule diameter for a given weight fraction of capsules. Self-healing performance reached maximum levels only when sufficient healing agent was available to entirely fill the crack. Based on these relationships, the size and weight fraction of microcapsules can be rationally chosen to give optimal healing of a predetermined crack size. By using this strategy, self-healing was demonstrated with smaller microcapsules and with lower weight fractions of microcapsules. Blaiszik *et al.* further produced smaller capsules (down to 220 nm) using sonication techniques and an ultra-hydrophobe to stabilize the DCPD droplets [79]. It is believed that the nanocapsules will make self-healing materials responsive to damage initiated at a scale that is not currently possible and compatible with composites where the reinforcement spacing requires smaller capsules for applications such as self-healing thin films, coatings, and adhesives.

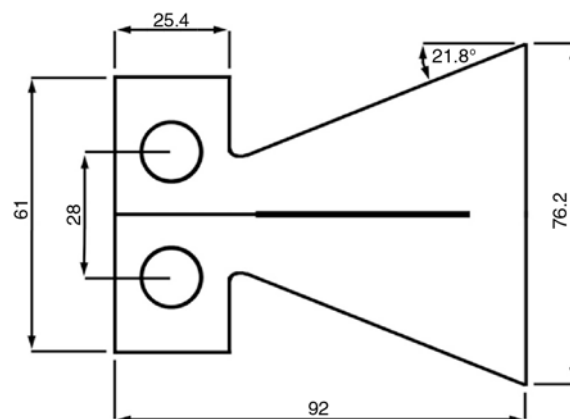


Figure 5. Schematic drawing of a TDCB specimen [78] (Reprinted from *Polymer*, Vol 48, Rule J. D., Sottos N. R., White S. R., Effect of microcapsule size on the performance of self-healing polymers, 3520–3529, Copyright (2007), with permission from Elsevier)

Comparison of fracture toughness of original specimen with that of healed one used to be a measure of healing effect. Conventional single-edge notched bending (SENB) and compact tension (CT) tests might be problematic in this case, as the pre-notches would be partly closed after healing process and an accurate measurement cannot be guaranteed. To overcome the difficulty, White *et al.* proposed a testing protocol with a tapered double cantilever beam (TDCB) configuration (Figure 5) [67, 69]. The specific geometry ensures that the measured fracture toughness is nearly independent of pre-crack length, so that healing efficiency can be precisely determined.

The researches so far suggest that one of the key issues of self-healing composites by means of microencapsulation lies in rigidity of the shell substance and matrix. Like the case of hollow tubes discussed hereinbefore, crack trigger in microsphere embedded composites depends on matching of deformation characteristics of the related materials. Route of crack propagation is a function of the stiffness ratio of microcapsules and matrix [55]. If

the inclusion has higher modulus than the matrix, the approaching crack tends to pass by the microcapsules; conversely, the crack could penetrate the microcapsules when the matrix is stiffer. On the other hand, simulation experiments manifest that the difference in fracture toughness of the microcapsules and matrix should be less than $0.11 \text{ MPa}\cdot\text{m}^{1/2}$ [80]. Otherwise, cracks would not pass through the microcapsules.

The other critical factors include (i) good adhesion between microencapsulated healing agent and the matrix, (ii) size and concentration of microencapsulated healing agent, (iii) rate and degree of polymerization of the released healing agent, and (iv) shell thickness and core content of the microencapsulated healing agent.

In contrast to the above methods, Cho *et al.* dispersed phase-separated droplets of hydroxyl end-functionalized polydimethylsiloxane (HOPDMS) and polydiethoxysiloxane (PDES) into a vinyl ester matrix, in which the catalyst, di-*n*-butyltin dilaurate (DBTL), contained within polyurethane microcapsules, were pre-embedded [81]. Polycondensation of HOPDMS with PDES occurred when they met the tin-catalyst from the broken capsules induced by mechanical damage. This system possesses some advantages, including (i) the healing chemistry remains stable in humid or wet environments, (ii) the chemistry is stable to an elevated temperature ($>100^\circ\text{C}$), enabling healing in higher-temperature thermoset systems, (iii) the components are widely available and comparatively low in cost, and (iv) the concept of phase separation of the healing agent simplifies processing, as the healing agent can now be simply mixed into the polymer matrix.

As for crack repair in elastomer, Keller *et al.* incorporated poly(urea-formaldehyde) (UF) walled microcapsules, which contained the constituent resin and initiator, respectively, into poly(dimethyl siloxane) (PDMS) [82]. The resin microcapsules were loaded with high-molecular weight vinyl functionalized PDMS and platinum catalyst complexes, while the initiator microcapsules contained a PDMS copolymer with active sites that would link to the vinyl functionalized resin via the action of the platinum catalyst. Damage triggering and healing events took place in an analogous way to the original self-healing epoxy described above. A propagating tear in the PDMS material intersected

both resin and initiator microcapsules and ruptured them. The liberated healing fluids then wicked onto the tear plane through capillary action and mix. A crosslinking reaction, the same reaction that polymerized the matrix material, occurred and formed an adhesive polymer layer that rebonded the tear faces. This self-healing material system possesses the unique feature that the healed polymer in the crack plane is the same as the host matrix.

In addition to the polymerizable healing agent, Caruso *et al.* used solvents to heal cracks in thermoset materials [83]. Chlorobenzene was encapsulated by urea-formaldehyde and embedded in epoxy matrix. It is believed that the solvent would induce crosslinking of the incompletely cured resin and heal cracks. The technique might be an economical, simple, and potentially robust alternative to the recovery of virgin properties of a material after crack damage has occurred.

4. Conclusions

Achievements in the field of self-healing polymers and polymer composites are far from satisfactory, but the new opportunities that were found during research and development have demonstrated it is a challenging job to either invent new polymers with inherent crack repair capability or integrate existing materials with novel healing system. Interdisciplinary studies based on tight collaboration among scientists are prerequisites for overcoming the difficulties. Comparatively, extrinsic self-healing techniques might be easier for large-scale usage for the moment. The works and outcomes in this aspect have broadened the application possibility of polymeric materials. Also, the extended service life of components made from these intelligent materials would contribute to reduce waste disposal. It is undoubtedly important for building up a sustainable society.

Besides the approaches described in the above text (Table 1), ongoing attempts are continuously presenting new concepts. For example, Lee *et al.* considered solid-state devices that integrate ductile polymeric layers and brittle semiconductor or metal films [84]. Using computer simulations, they showed that adding nanoparticles to the polymers yielded materials in which the particles became localized at nanoscale cracks and effectively form 'patches' to repair the damaged regions. Trau *et al.*

Table 1. Self-healing in polymers and polymer composites

Category of materials to be repaired	Materials to be repaired	Healing system	Trigger mechanism	Healing mechanism	Assessment of healing effect	Ref.
Thermoplastic	Poly(methyl methacrylate), etc.	Bulk	Heating or solvent induced	Chain interdiffusion and entanglements	Compact tension (CT) test or photography	[10, 16, 17]
Thermoplastic	Poly(ethylene-co-methacrylic acid)	Bulk	Thermomechanically induced melting	Chain interdiffusion and entanglements	Visual inspection after sawing, cutting and puncture	[18]
Thermoplastic	Polycarbonate	Bulk (weak alkali/hydrolyzed chains)	Steam	Weak alkali catalyzed polymerization	Molecular weight and mechanical strength	[25]
Thermoplastic	Poly(phenylene ether)	Bulk (copper ion/oxygen/scission chains)	Heating	Copper ion catalyzed polymerization	Molecular weight	[26]
Thermoset	Epoxy	Bulk	Heating	Post-curing of residual functional groups	Impact strength	[19, 20]
Thermoplastic/thermoset semi-interpenetrating network	Poly(bisphenol-A-co-epichlorohydrin)/epoxy	Bulk	Heating	Chain interdiffusion and entanglements	CT and impact tests; photography	[22, 23]
Thermally reversible crosslinking network	Crosslinked multifuran/multimaleimide	Bulk	Heating	Diels-Alder reaction	CT and double cleavage drilled compression	[27, 28, 31]
Thermoset	Epoxy, fiber/unsaturated polyester, and fiber/epoxy	Cyanoacrylate, epoxy, unsaturated polyester, etc.	Crack induced breakage of hollow tubes containing healant	Curing of healant	Tensile, flexural and impact tests; photography; ultrasonic C-scan	[32–48]
Thermoset	Epoxy	Dicyclopentadiene/Grubbs' catalyst	Crack induced damage of 3D microvascular networks, releasing healant	Ring-opening metathesis polymerization of healant	Four-point bending	[53]
Thermoset	Unsaturated polyester	Styrene or epoxy	Crack induced rupture of microencapsulated healant	Polymerization or curing of healant	Mechanical strength and visual inspection	[60]
Thermoset	Glass fiber/epoxy	Epoxy granules	Heating	Curing of healant	Three-point bending and tensile fatigue	[62]
Thermoset	Epoxy and woven glass fiber/epoxy	Epoxy/latent hardener	Crack induced rupture of microencapsulated epoxy	Curing of healant	Single edge notched bend (SENB) and double cantilever beam (DCB) tests	[63]
Thermoset	Epoxy, fiber/unsaturated polyester, and fiber/epoxy	Dicyclopentadiene/Grubbs' catalyst	Crack induced rupture of microencapsulated healant	Ring-opening metathesis polymerization of healant	Tapered double cantilever beam (TDCB), DCB and fatigue tests	[55, 67–78]
Thermoset	Unsaturated polyester	Phase-separated polysiloxane droplets/tin catalyst	Crack induced rupture of microencapsulated catalyst	Polycondensation of polysiloxanes	TDCB	[81]
Elastomer	Silicone rubber	Polysiloxane/platinum catalyst/initiator	Crack induced rupture of microencapsulated healant and initiator	Polycondensation of polysiloxanes	Tear strength	[82]
Thermoset	Epoxy	Solvent (chlorobenzene)	Crack induced rupture of microencapsulated solvent	Solvent induced crosslinking of incompletely cured resin	TDCB	[83]

proposed healing under electric field in terms of electrohydrodynamic aggregation of colloidal dielectric particles [85]. By creating a semi-interpenetrating network composed of a crosslinked thermoset and a thermoplastic, Karger-Kocsis considered that both shape memory and self healing functions can be combined [86]. In such a intelligent material, the thermoplastic polymer (amorphous or semicrystalline) offers ‘switching’ and ‘healing’ effects, whereas the crosslinked thermoset acts as the fixing phase.

From a long-term point of view, synthesis of brand-new polymers accompanied by intrinsic self-healing function through molecular design would be a reasonable solution. Recent exploration has shown the prospects of this trend, but the automatic trigger mechanism remains open. Working out the solutions would certainly push polymer sciences and engineering forward.

Acknowledgements

The authors are grateful to the support of the Natural Science Foundation of China (Grants: 50573093, U0634001).

References

- [1] Riefsnyder K. L., Schulte K., Duke J. C.: Long term failure behavior of composite materials. *ASTM Special Technical Publications*, **813**, 136–159 (1983).
- [2] Trask R. S., Williams H. R., Bond I. P.: Self-healing polymer composites: Mimicking nature to enhance performance. *Bioinspiration and Biomimetics*, **2**, 1–9 (2007).
- [3] Hastings G. W., Mahmud E. A.: Intelligent orthopaedic materials. *Journal of Intelligent Material Systems and Structure*, **4**, 452–457 (1993).
- [4] Martin P.: Wound healing-aiming for perfect skin regeneration. *Science*, **276**, 75–81 (1997).
- [5] Caplan A. I.: Bone development, cell and molecular biology of vertebrate hard tissues. *Ciba Foundation Symposium*, **136**, 3–21 (1988).
- [6] Albert S. F., Wong E.: Electrical stimulation of bone repair. *Clinics in Podiatric Medicine and Surgery*, **8**, 923–935 (1981).
- [7] Wool R. P., O’Connor K. M.: A theory of crack healing in polymers. *Journal of Applied Physics*, **52**, 5953–5963 (1981).
- [8] Wool R. P., Yuan B-L., McGarel O. J.: Welding of polymer interfaces. *Polymer Engineering and Science*, **29**, 1340–1367 (1989).
- [9] Kim Y. H., Wool R. P.: A theory of healing at a polymer-polymer interface. *Macromolecules*, **16**, 1115–1120 (1983).
- [10] Jud K., Kaush H. H.: Load transfer through chain molecules after interpenetration at interfaces. *Polymer Bulletin*, **1**, 1697–1707 (1979).
- [11] Kaush H. H., Jud K.: Molecular aspects of crack formation and healing in glassy polymers. *Plastics and Rubber Processing and Applications*, **2**, 265–268 (1982).
- [12] Wool R. P.: Relation for healing, fracture, self-diffusion and fatigue of random coil polymers. *American Chemical Society, Polymer Preprints*, **23**, 62–63 (1982).
- [13] Jud K., Kausch H. H., Williams J. G.: Fracture mechanics studies of crack healing and welding of polymers. *Journal of Materials Science*, **16**, 204–210 (1981).
- [14] McGarel O. J., Wool R. P.: Craze growth and healing in polystyrene. *Journal of Polymer Science, Part B: Polymer Physics*, **25**, 2541–2560 (1987).
- [15] Wool R. P., Rockhill A. T.: Molecular aspects of fracture and crack healing in glassy polymers. *American Chemical Society, Polymer Preprints*, **21**, 223–224 (1980).
- [16] Lin C. B., Lee S., Liu K. S.: Methanol-induced crack healing in poly(methyl methacrylate). *Polymer Engineering and Science*, **30**, 1399–1406 (1990).
- [17] Wang P-P., Lee S., Harmon J.: Ethanol-induced crack healing in poly(methyl methacrylate). *Journal of Polymer Science, Part B: Polymer Physics*, **32**, 1217–1227 (1994).
- [18] Kalista S. J., Ward T. C.: Thermal characteristics of the self-healing response in poly(ethylene-co-methacrylic acid) copolymers. *Journal of the Royal Society: Interface*, **4**, 405–411 (2007).
- [19] Outwater J. O., Gerry D. J.: On the fracture energy, rehealing velocity and refracture energy of cast epoxy resin. *Journal of Adhesion*, **1**, 290–298 (1969).
- [20] Wool R. P.: *Polymer interfaces: Structure and strength*. Hanser, Munich, (1994).
- [21] Jayarama R., Wool R. P.: Interfaces in repair, recycling, joining and manufacture of polymers and polymer composites. *Journal of Applied Polymer Science*, **71**, 775–785 (1999).
- [22] Hayes S. A., Jones F. R., Marshiya K., Zhang W.: A self-healing thermosetting composite material. *Composites, Part A: Applied Science and Manufacturing*, **38**, 1116–1120 (2007).
- [23] Hayes S. A., Zhang W., Branthwaite M., Jones F. R.: Self-healing of damage in fibre-reinforced polymer-matrix composites. *Journal of the Royal Society: Interface*, **4**, 381–387 (2007).
- [24] Hayes S. A., Jones F. R.: Self healing composite materials. UK Patent, GB0500242.3. (2004).
- [25] Takeda K., Unno H., Zhang M.: Polymer reaction in polycarbonate with Na₂CO₃. *Journal of Applied Polymer Science*, **93**, 920–926 (2004).
- [26] Takeda K., Tanahashi M., Unno H.: Self-repairing mechanism of plastics. *Science and Technology of Advanced Materials*, **4**, 435–444 (2003).

- [27] Chen X., Dam M. A., Ono K., Mal A., Shen H., Nutt S. R., Sheran K., Wudl F.: A thermally re-mendable cross-linked polymeric material. *Science*, **295**, 1698–1702 (2002).
- [28] Chen X., Wudl F., Mal A. K., Shen H., Nutt S. R.: New thermally remendable highly cross-linked polymeric materials. *Macromolecules*, **36**, 1802–1807 (2003).
- [29] Liu Y-L., Hsieh C-Y.: Crosslinked epoxy materials exhibiting thermal remendability and removability from multifunctional maleimide and furan compounds. *Journal of Polymer Science, Part A: Polymer Chemistry*, **44**, 905–913 (2006).
- [30] Liu Y-L., Chen Y-W.: Thermally reversible crosslinked polyamides with high toughness and self-repairing ability from maleimide- and furan-functionalized aromatic polyamides. *Macromolecular Chemistry and Physics*, **208**, 224–232 (2007).
- [31] Plaisted T. A., Nemat-Nasser S.: Quantitative evaluation of fracture, healing and re-healing of a reversibly cross-linked polymer. *Acta Materialia*, **55**, 5684–5696 (2007).
- [32] Dry C.: Passive tunable fibers and matrices. *International Journal of Modern Physics, B*, **6**, 2763–2771 (1992).
- [33] Dry C.: Matrix cracking repair and filling using active and passive modes for smart timed release of chemicals from fibers into cement matrices. *Smart Materials and Structures*, **3**, 118–123 (1994).
- [34] Dry C., McMillan W.: Three-part methylmethacrylate adhesive system as an internal delivery system for smart responsive concrete. *Smart Materials and Structures*, **5**, 297–300 (1996).
- [35] Dry C.: Procedures developed for self-repair of polymer matrix composite materials. *Composite Structures*, **35**, 263–269 (1996).
- [36] Motuku M., Vaidya U. K., Janowski C. M.: Parametric studies on self-repairing approaches for resin infused composites subjected to low velocity impact. *Smart Materials and Structures*, **8**, 623–638 (1999).
- [37] Zhao X. P., Zhou B. L., Luo C. R., Wang J. H., Liu J. W.: A model of intelligent material with self-repair function (in Chinese). *Chinese Journal of Materials Research*, **10**, 101–104 (1996).
- [38] Bleay S. M., Loader C. B., Hawyres V. J., Humberstone L., Curtis P. T.: A smart repair system for polymer matrix composites. *Composites, Part A: Applied Science and Manufacturing*, **32**, 1767–1776 (2001).
- [39] Dry C., Sottos N. R.: Passive smart self-repair in polymer matrix composite materials. *Proceedings of SPIE – The International Society for Optical Engineering*, **1916**, 438–444 (1993).
- [40] Dry C., McMillan W.: Crack and damage assessment in concrete and polymer matrices using liquids released internally from hollow optical fibers. *Proceedings of SPIE – The International Society for Optical Engineering*, **2718**, 448–451 (1996).
- [41] Dry C., Haven P.: Smart-fiber-reinforced matrix composites. US patent 5803963, USA (1998).
- [42] Dry C., Line S., Winona M.: Self-repairing reinforced matrix materials. US patent 7022179 B1, USA (2006).
- [43] Motuku M., Janowski G. M., Vaidya U. K., Mahfuz H., Jeelani S.: Low velocity impact characterization of unreinforced vinyl ester 411-350 and 411-C50 resin systems. *Polymer and Polymer Composites*, **7**, 383–407 (1999).
- [44] Pang J. W. C., Bond I. P.: A hollow fibre reinforced polymer composite encompassing self-healing and enhanced damage visibility. *Composites Science and Technology*, **65**, 1791–1799 (2005).
- [45] Pang J. W. C., Bond I. P.: ‘Bleeding composites’-damage detection and self-repair using a biomimetic approach. *Composites, Part A: Applied Science and Manufacturing*, **36**, 183–188 (2005).
- [46] Trask R. S., Bond I. P.: Biomimetic self-healing of advanced composite structures using hollow glass fibres. *Smart Materials and Structures*, **15**, 704–710 (2006).
- [47] Trask R. S., Williams G. J., Bond I. P.: Bioinspired self-healing of advanced composite structures using hollow glass fibres. *Journal of the Royal Society: Interface*, **4**, 363–371 (2007).
- [48] Williams G., Trask R. S., Bond I. P.: A self-healing carbon fibre reinforced polymer for aerospace applications. *Composites, Part A: Applied Science and Manufacturing*, **38**, 1525–1532 (2007).
- [49] Yang H., Liang D., Tao B., Qiu H.: Application and influence of hollow optical fiber embedded in fiber glass/epoxy composite materials (in Chinese). *Transactions of Nanjing University of Aeronautics and Astronautics*, **17**, 130–134 (2000).
- [50] Yang H., Liang D. K., Tao B. Q., Huang M. S., Qiu H.: Research on the performance and application of hollow-center optical fiber in smart material (in Chinese). *Materials Science and Engineering*, **18**, 27–30 (2000).
- [51] Yang H., Liang D. K., Tao B. Q., Qiu H., Cao Z. X.: Research on self-diagnose and self-repair using hollow-center optical fiber in smart structure (in Chinese). *Journal of Functional Materials*, **32**, 419–424 (2001).
- [52] Hiemstra D. L., Sottos N. R.: Thermally induced interfacial microcracking in polymer matrix composites. *Journal of Composite Materials*, **27**, 1030–1051 (1993).
- [53] Toohy K. S., Sottos N. R., Lewis J. A., Moore J. S., White S. R.: Self-healing materials with microvascular networks. *Nature Materials*, **6**, 581–585 (2007).
- [54] Therriault D., Shepherd R. F., White S. R., Lewis J. A.: Fugitive inks for direct-write assembly of three-dimensional microvascular networks. *Advanced Materials*, **17**, 394–399 (2005).
- [55] White S. R., Sottos N. R., Geubelle P. H., Moore J. S., Kessler M. R., Sriram S. R., Brown E. N., Viswanathan S.: Autonomic healing of polymer composites. *Nature*, **409**, 794–797 (2001).

- [56] Bejan A., Lorente S., Wang K-M.: Networks of channels for self-healing composite materials. *Journal of Applied Physics*, **100**, 033528/1–033528/6 (2006).
- [57] Gardner G. L.: Manufacturing encapsulated products. *Chemical Engineering Progress*, **62**, 87–91 (1966).
- [58] Fanger G. O.: What good are microcapsules? *Chemtech*, **4**, 397–405 (1974).
- [59] Song J., Chen L., Li X. J.: Microencapsulation and its application (in Chinese). Chemical Engineering Press, Beijing, (2001).
- [60] Jung D., Hegeman A., Sottos N. R., Geubelle P. H., Whites S. R.: Self-healing composites using embedded microspheres. in 'Proceedings of the ASME International Mechanical Engineering Congress and Exposition, Dallas, USA', Vol MD-80, 265–275 (1997).
- [61] White S. R., Sottos N. R., Geubelle P. H., Moore J. S., Siriram S. R., Kessler M. R., Brown E. N.: Multifunctional autonomically healing composite material. US Patent 6 858 659, USA, (2005).
- [62] Zako M., Takano N.: Intelligent material systems using epoxy particles to repair microcracks and delamination damage in GFRP. *Journal of Intelligent Material Systems and Structure*, **10**, 836–841 (1999).
- [63] Yin T., Rong M. Z., Zhang M. Q., Yang G. C.: Self-healing epoxy composites- Preparation and effect of the healant consisting of microencapsulated epoxy and latent curing agent. *Composites Science and Technology*, **67**, 201–212 (2007).
- [64] Dowbenko R., Anderson C. C., Chang W. H.: Imidazole complexes as hardeners for epoxy adhesives. *Industrial and Engineering Chemistry Product Research and Development*, **10**, 344–351 (1971).
- [65] Ibonai M., Kuramochi T.: Curing of epoxy resin by use of imidazole/metal complexes (in Japanese). *Reinforced Plastics*, **26**, 69–73 (1975).
- [66] Yin T., Zhou L., Rong M. Z., Zhang M. Q.: Self-healing woven glass fabric/epoxy composites with the healant consisting of micro-encapsulated epoxy and latent curing agent. *Smart Materials and Structures*, **17**, 015019/1–015019/8 (2008).
- [67] Brown E. N., Sottos N. R., White S. R.: Fracture testing of a self-healing polymer composite. *Experimental Mechanics*, **42**, 372–379 (2002).
- [68] Brown E. N., White S. R., Sottos N. R.: Microcapsule induced toughening in a self-healing polymer composite. *Journal of Materials Science*, **39**, 1703–1710 (2004).
- [69] Rule J. D., Sottos N. R., White S. R., Moore J. S.: The chemistry of self-healing polymers. *Education in Chemistry*, **42**, 130–132 (2005).
- [70] Rule J., Brown E. N., Sottos N. R., White S. R., Moore J. S.: Wax-protected catalyst microspheres for efficient self-healing materials. *Advanced Materials*, **72**, 205–208 (2005).
- [71] Jones A. S., Rule J. D., Moore J. S., White S. R., Sottos N. R.: Catalyst morphology and dissolution kinetics of self-healing polymers. *Chemistry of Materials*, **18**, 1312–1317 (2006).
- [72] Kessler M. R., White S. R.: Self-activated healing of delamination damage in woven composites. *Composites, Part A: Applied Science and Manufacturing*, **32**, 683–699 (2001).
- [73] Kessler M. K., Sottos N. R., White S. R.: Self-healing structural composite material. *Composites, Part A: Applied Science and Manufacturing*, **34**, 743–753 (2003).
- [74] Brown E. N., White S. R., Sottos N. R.: Retardation and repair of fatigue cracks in a microcapsule toughened epoxy composite- Part I: Manual infiltration. *Composites Science and Technology*, **65**, 2466–2473 (2005).
- [75] Brown E. N., White S. R., Sottos N. R.: Retardation and repair of fatigue cracks in a microcapsule toughened epoxy composite- Part II: In situ self-healing. *Composites Science and Technology*, **65**, 2474–2480 (2005).
- [76] Jones A. S., Rule J. D., Moore J. S., Sottos N. R., White S. R.: Life extension of self-healing polymers with rapidly growing fatigue cracks. *Journal of the Royal Society Interface*, **4**, 395–403 (2007).
- [77] Wilson G. O., Moore J. S., White S. R., Sottos N. R., Andersson H. M.: Autonomic healing of epoxy vinyl esters via ring opening metathesis polymerization. *Advanced Functional Materials*, **18**, 44–52 (2008).
- [78] Rule J. D., Sottos N. R., White S. R.: Effect of microcapsule size on the performance of self-healing polymers. *Polymer*, **48**, 3520–3529 (2007).
- [79] Blaiszik B. J., Sottos N. R., White S. R.: Nanocapsules for self-healing materials. *Composites Science and Technology*, **68**, 978–986 (2008).
- [80] Yang Y., Zhang H., Zhang J., Wang S-H., Duan C-J., He Y-J.: The experiment study of fracture mechanics on self-healing composite material containing microcapsules (in Chinese). *Materials Review*, **21**, 143–147 (2007).
- [81] Cho S. H., Andersson H. M., White S. R., Sottos N. R., Braun P. V.: Polydimethylsiloxane-based self-healing materials. *Advanced Materials*, **18**, 997–1000 (2006).
- [82] Keller M. K., White S. R., Sottos N. R.: A self-healing poly(dimethyl siloxane) elastomer. *Advanced Functional Materials*, **17**, 2399–2404 (2007).
- [83] Caruso M. M., Delafuente D. A., Ho V., Moore J. S., Sottos N. R., White S. R.: Solvent-promoted self-healing materials. *Macromolecules*, **40**, 8830–8832 (2007).
- [84] Lee J. Y., Buxton G. A., Balazs A. C.: Using nanoparticles to create self-healing composites. *Journal of Chemical Physics*, **121**, 5531–5540 (2004).
- [85] Trau M., Sankaran S., Saville D. A., Aksay I. A.: Electric-field-induced pattern formation in colloidal dispersions. *Nature*, **374**, 437–439 (1995).
- [86] Ratna D., Karger-Kocsis J.: Recent advances in shape memory polymers and composites: A review. *Journal of Materials Science*, **43**, 254–269 (2008).

Suzuki coupling reactions catalyzed by poly(*N*-ethyl-4-vinylpyridinium) bromide stabilized palladium nanoparticles in aqueous solution

L. Z. Ren, L. J. Meng*

School of Chemistry and Chemical Technology, Shanghai Jiao Tong University, 800 Dongchuan Road, Shanghai 200240, P. R. China

Received 21 December 2007; accepted in revised form 24 February 2008

Abstract. In this work, it was investigated to use of poly(*N*-ethyl-4-vinylpyridinium) bromide stabilized palladium nanoparticles in the Suzuki reaction between phenylboronic acid and aryl halides in aqueous solution. The nanoparticles were isolated and re-used several times with low loss of activity.

Keywords: *nanomaterials, Pd, polymer, Suzuki reaction*

1. Introduction

The Suzuki coupling reaction between arylboronic acids and aryl halides is one of the most effective methods for the preparation of biaryl compounds [1, 2], which are an important class of organic compounds useful as precursors to pharmaceuticals, ligands, liquid crystals, and polymers. The classical conditions for performing these coupling reactions involve the use of various Pd/ligand complexes [3, 4] as catalysts in organic solvents. These catalysts include many different kinds of phosphine-based palladium catalysts as well as phosphine-free palladium catalysts. However, phosphine ligands may be toxic or expensive and one serious drawback in the use of homogeneous metal catalysts is that they often are difficult to separate from the reaction mixtures and recycle.

It is of interest to develop new catalysts that are environmentally benign and effective. Stabilized palladium nanoparticles have also been reported as catalysts for the Suzuki coupling reaction [5].

Noble metal colloidal particles have a characteristic large surface-to-volume ratio, and consequently large fractions of the metal atoms are accessible to reactant molecules and available for catalysis. However, unprotected metallic nanoparticles in solution are kinetically unstable with respect to aggregation to larger particles or bulk metal, and must therefore be stabilized by electrostatic or steric protection to keep them from agglomerating. This stabilization of nanoparticles in solution can be achieved by adding a stabilizer, for example surfactants, soluble polymers, quaternary ammonium salts, or polyoxoanions. Palladium nanoparticles stabilized with poly(*N*-vinyl-2-pyrrolidone) [6–8], poly(amidoamine) dendrimers [9, 10], polystyrene-*b*-poly(sodium acrylate) block copolymer [9], Keggin-type polyoxometalate [11], cyclodextrin [12], and poly(*N,N*-dihexylcarbodiimide) [13, 14], have been used to catalyze various Suzuki reactions in different solvents. Use of water as a reaction medium for transition-metal-catalyzed reactions is

*Corresponding author, e-mail: menglingjie@sjtu.edu.cn
© BME-PT and GTE

very attractive for organic synthesis because it is non-toxic, cheap and readily available. However, the reported catalytic activities of the recovered catalysts using water as solvent are too low for them to be reused for practical organic synthesis. Here we have investigated the use of the polycationic poly(*N*-ethyl-4-vinylpyridinium) bromide (pEVPBr) polymer as a stabilizer for palladium nanoparticles by studying the Suzuki reaction.

2. Experimental

2.1. Materials and methods

4-Vinylpyridine (>96%), iodobenzene (>99%), 1-bromo-4-methoxybenzene (>97%), chlorobenzene (>98%), and phenylboronic acid (>97%) were purchased from Fluka. Bromoethane (>98%), PdCl₂, and all solvents were obtained from Shanghai Sinopharm Group Chemical Reagent Co., Ltd. All chemicals were used as received. pEVPBr was synthesized according to Marcilla *et al.* [15]. Pd nanoparticles were investigated by transmission electron microscopy (TEM) on a JEOL 2010 transmission electron microscope. The samples were prepared by placing a drop of the solution on carbon coated copper grids and allowed to dry in air. The particle size and size distribution were determined by manually measuring around 200 particles from enlarged TEM images using ImageJ. The

identity of synthesized compounds was confirmed by ¹H NMR.

2.2. Preparation of pEVPBr-stabilized Pd nanoparticles

An aqueous solution of H₂PdCl₄ (5 mM) was prepared by adding HCl (6 ml, 0.2 M) to PdCl₂ (0.6 mmol) in water (114 ml). Ethanol (20 ml), water (10 ml) and pEVPBr (210 mg) were added to 20 ml of the H₂PdCl₄ solution to yield a pEVPBr:Pd (monomeric unit:metal) ratio of 10:1. The solution was refluxed under air for 3 hours, turning dark brown. The solution was evaporated to dryness under vacuum at 60°C, and the residue re-dissolved in 5 ml of water for later use.

2.3. Suzuki coupling reactions

In a typical Suzuki coupling reaction experiment, iodobenzene (1 mmol), phenylboronic acid (1 mmol) and Na₂CO₃ (3 mmol) were added to ethanol (aq., 30% v/v, 5 ml) in a 10 ml round-bottom flask. The mixture was vigorously stirred and heated to the temperature stated in Table 1, and 0.2 mol% of palladium in the form of pEVPBr-stabilized Pd nanoparticles were added. At the end of the reaction, the reaction mixture was extracted three times with petroleum ether (5 ml). The combined extrac-

Table 1. Product yields for Suzuki coupling reaction catalyzed by pEVPBr-Pd nanoparticles

Entry	R	X	Pd [mol%]	Temperature [°C]	Base	Time [h]	Yield [%]
1	H	I	0.20	90	Na ₂ CO ₃	0.5	59
2	H	I	0.20	90	Na ₂ CO ₃	1	76
3	H	I	0.20	90	Na ₂ CO ₃	2	83
4	H	I	0.20	90	Na ₂ CO ₃	4	90
5	H	I	0.20	90	Na ₂ CO ₃	9	95
6	H	I	0.10	90	Na ₂ CO ₃	9	89
7	H	I	0.05	90	Na ₂ CO ₃	9	85
8 ^a	H	I	0.20	90	Et ₃ N	9	96
9 ^b	H	I	0.20	90	Et ₃ N	9	89
10 ^c	H	I	0.20	90	Et ₃ N	9	82
11 ^d	H	I	0.20	90	Et ₃ N	9	81
12	H	I	0.20	50	Na ₂ CO ₃	9	63
13	H	I	0.20	50	Et ₃ N	9	61
14	4-CH ₃ O	Br	0.20	90	Na ₂ CO ₃	9	68
15	H	Cl	0.20	90	Na ₂ CO ₃	9	35

^athe first run, ^bthe second run, ^cthe third run, ^dthe fourth run

tion was washed with water and the organic phase was separated and concentrated with reduced pressure. The resulting crude was purified by column chromatography on silica gel to give final biphenyl product.

3. Results and discussion

3.1. Characterization of Pd nanoparticles

The Pd nanoparticles displayed good stability under storage, with no palladium black observed even after several months. A typical micrograph of the Pd nanoparticles is shown in Figure 1a. A relatively narrow size distribution, with an average diameter of 3.6 ± 0.7 nm, was observed. Repeated recycling of the catalyst phase, as described below, led to aggregation, yielding larger clusters made up by particles with an average size of 6.5 ± 1.2 nm (Figure 1b).

3.2. Catalytic performance of Pd nanoparticles

The catalytic performance of the pEVPBr-stabilized Pd nanoparticles was evaluated by using the Suzuki coupling reaction in aqueous solution. The results shown in Table 1 reveal that pEVPBr-Pd is a highly active catalyst in the Suzuki reaction under relatively mild conditions. When 0.2 mol% of pEVPBr-Pd as catalyst in aqueous Na_2CO_3 solution

was used to catalyze the reaction between iodobenzene and phenylboronic acid, the yields of biphenyl were 59, 76, 83, 90, and 95% after 0.5, 1, 2, 4, and 9 hours, respectively (entries 1–5). Next, the amount of pEVPBr-Pd and lower reaction temperatures were examined (entries 5, 6, 7, 12, 13). Although the reaction proceeded at 50°C (entries 12 and 13) or when 0.05 mol% of catalyst was used (entries 7), relatively longer reaction times were needed to get full conversion. In addition, 1-bromo-4-methoxybenzene and chlorobenzene were chosen as substrates to perform the Suzuki coupling reaction. However, the yields of using 1-bromo-4-methoxybenzene and chlorobenzene as reactant were lower than that of iodobenzene under the same reaction conditions (entries 14 and 15). Finally, we found that using triethylamine as base is also suitable under these conditions, and this base was used in the recycling experiments. After the reaction mixture was extracted with petroleum ether, the aqueous phase containing the catalyst was separated and ethanol (1.5 ml) was added together with new substrate and triethylamine, to recycle the palladium nanoparticles. After recycling, the Pd nanoparticles became larger than before the reaction; a typical micrograph of the Pd nanoparticles after recycling twice is shown in Figure 1b. Although the catalytic activity gradually diminished due to formation of Pd black, the catalyst can be recycled several times with acceptable yields (entries 8–11).

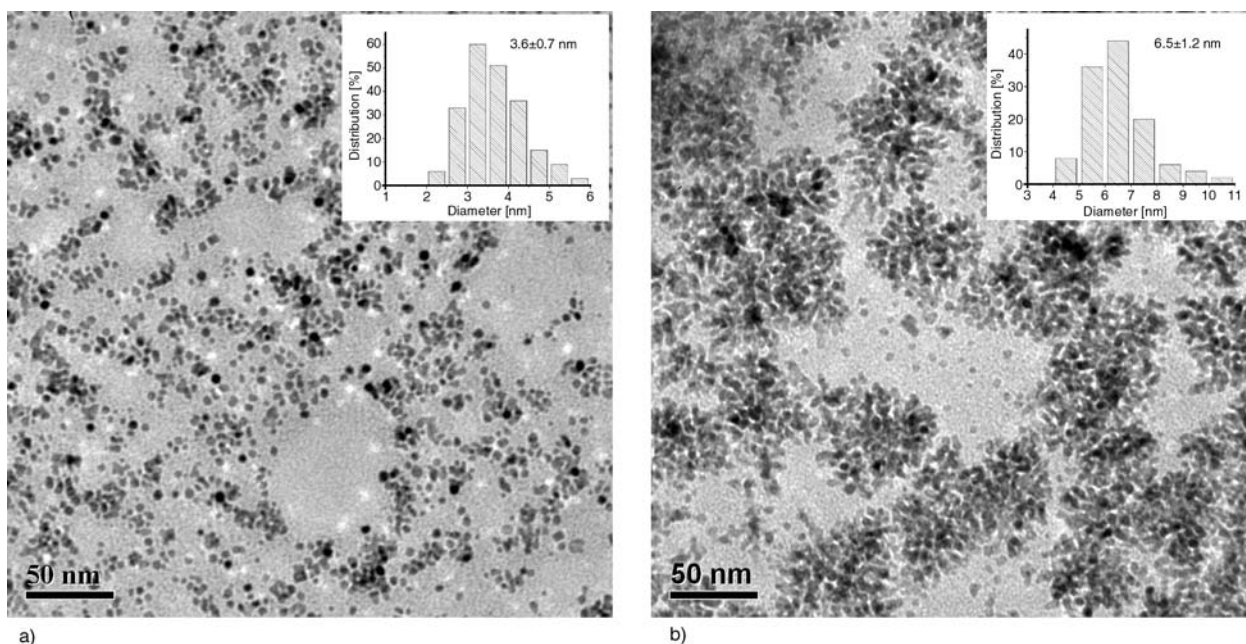


Figure 1. TEM images of pEVPBr-Pd nanoparticles before (a) and after recycling twice (b). The inset shows the particle size distribution

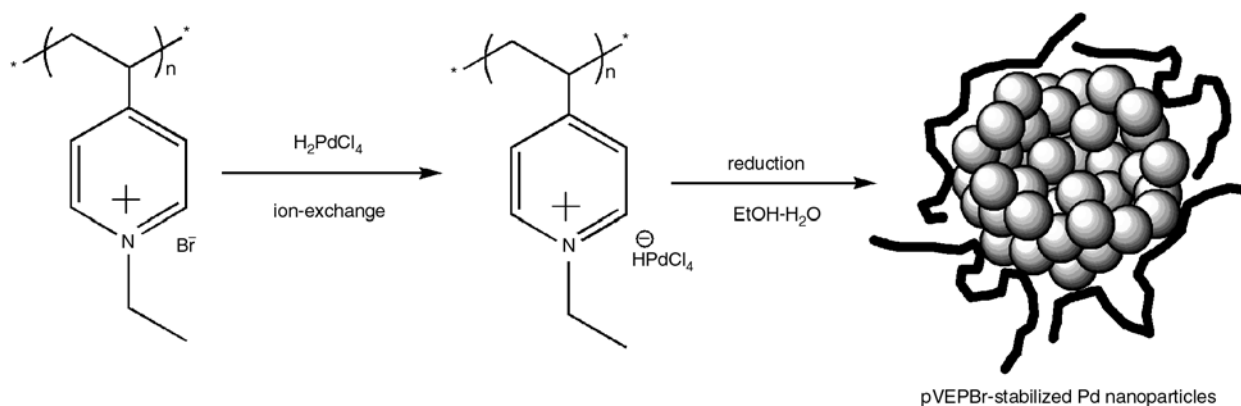


Figure 2. Formation scheme of Pd nanoparticles by using pVEPBr

pVEPBr is a kind of polymer with pyridium groups along a polymeric chain. When the polymer was used in the in situ synthesis of Pd nanoparticles, it can be speculate that the HPdCl_4^- anion was attached to pyridium units of the polymer chain by ion-exchanging and then the ‘metalized’ polymer was reduced with ethanol to produce the Pd nanoparticles (Figure 2). pVEPBr have been shown to be effective stabilizer for preparing narrowly dispersed Pd nanoparticles and for preventing agglomeration of colloidal Pd nanoparticles. Apart from the wide ranging adaptability of polymer, some additional advantages of polycationic pVEPBr polymer are obvious: as high molecular weight stabilizers, additional mechanisms of colloidal stabilization can be invoked, i.e., steric and electrosteric stabilization contributions are added to the standard stabilization by charge repulsion (electrostatic). We believe that the stability of the of the colloidal Pd nanoparticles arises from both eletrostatic and steric effects of pVEPBr.

4. Conclusions

A simple method for preparing pVEPBr-stabilized Pd nanoparticles in aqueous solution has been described. The pVEPBr-stabilized Pd nanoparticles are quite stable and provide high catalytic activity in Suzuki coupling reactions under relatively mild conditions using low amounts of Pd in aqueous solution.

Acknowledgements

We gratefully acknowledge the supports of the National Science Foundation of China (Grant No. 60577049) and Fundamental Key Project (No. 05JC14019).

References

- [1] Suzuki A.: Recent advances in the cross-coupling reactions of organoboron derivatives with organic electrophiles, 1995–1998. *Journal of Organometallic Chemistry*, **576**, 147–168 (1999).
- [2] Miyaura N., Suzuki A.: Palladium-catalyzed cross-coupling reactions of organoboron compounds. *Chemical Reviews*, **95**, 2457–2483 (1995).
- [3] Zim D., Monteiro A. L., Dupont J.: $\text{PdCl}_2(\text{SEt}_2)_2$ and $\text{Pd}(\text{OAc})_2$: Simple and efficient catalyst precursors for the Suzuki cross-coupling reaction. *Tetrahedron Letters*, **41**, 8199–8202 (2000).
- [4] Beletskaya I. P., Cheprakov A. V.: Palladacycles in catalysis – A critical survey. *Journal of Organometallic Chemistry*, **689**, 4055–4082 (2004).
- [5] Roucoux A., Schulz J., Patin H.: Reduced transition metal colloids: A novel family of reusable catalysts? *Chemical Reviews*, **102**, 3757–3778 (2002).
- [6] Li Y., Hong X. M., Collard D. M., El-Sayed M. A.: Suzuki cross-coupling reactions catalyzed by palladium nanoparticles in aqueous solution. *Organic Letters*, **2**, 2385–2388 (2000).
- [7] Li Y., Boone E., El-Sayed M. A.: Size effects of PVP-Pd nanoparticles on the catalytic Suzuki reactions in aqueous solution. *Langmuir*, **18**, 4921–4925 (2002).
- [8] Narayanan R., El-Sayed M. A.: Effect of catalysis on the stability of metallic nanoparticles: Suzuki reaction catalyzed by PVP-palladium nanoparticles. *Journal of the American Chemical Society*, **125**, 8340–8347 (2003).
- [9] Li Y., El-Sayed M. A.: The effect of stabilizers on the catalytic activity and stability of Pd colloidal nanoparticles in the Suzuki reactions in aqueous solution. *Journal of Physical Chemistry, B*, **105**, 8938–8943 (2001).
- [10] Pittelkow M., Moth-Poulsen K., Boas U., Christensen J. B.: Poly(amidoamine)-dendrimer-stabilized Pd(0) nanoparticles as a catalyst for the Suzuki Reaction. *Langmuir*, **19**, 7682–7684 (2003).

- [11] Kogan V., Aizenshtat Z., Popovitz-Biro R., Neumann R.: Carbon-carbon and carbon-nitrogen coupling reactions catalyzed by palladium nanoparticles derived from a palladium substituted Keggin-type polyoxometalate. *Organic Letters*, **4**, 3529–3532 (2002).
- [12] Strimbu L., Liu J., Kaifer A. E.: Cyclodextrin-capped palladium nanoparticles as catalysts for the Suzuki reaction. *Langmuir*, **19**, 483–485 (2003).
- [13] Liu Y. B., Khemtong C., Hu J.: Synthesis and catalytic activity of a poly(*N,N*-dialkylcarbodiimide)/palladium nanoparticle composite: A case in the Suzuki coupling reaction using microwave and conventional heating. *Chemical Communications*, 398–399 (2004).
- [14] Hu J., Liu Y. B.: Pd nanoparticle aging and its implications in the Suzuki cross-coupling reaction. *Langmuir*, **21**, 2121–2123 (2005).
- [15] Marcilla R., Blazquez J. A., Fernandez R., Grande H., Pomposo J. A., Mecerreyes D.: Synthesis of novel polycations using the chemistry of ionic liquids. *Macromolecular Chemistry and Physics*, **206**, 299–304 (2005).

Effect of organic peroxides on the morphological, thermal and tensile properties of EVA-organoclay nanocomposites

S. B. Mishra, A. S. Luyt*

Department of Chemistry, University of the Free State (Qwaqwa Campus), Private Bag X13, Phuthaditjhaba, 9866, South Africa

Received 26 December 2007; accepted in revised form 25 February 2008

Abstract. Nanocomposites were prepared using an ethylene vinyl acetate copolymer (EVA) and organically modified Cloisite® 93A clay in the absence and presence of dicumyl peroxide (DCP) and dibenzyl peroxide (DBP) as cross-linking agents. The results clearly show differences in the EVA-clay morphology of nanocomposites prepared in the absence of organic peroxides, and of those prepared in the presence of respectively DCP and DBP. It seems as if DCP may initiate grafting between the polymer and the clay, which results in an exfoliated morphology. The presence of clay seems to inhibit the initiation of EVA crosslinking by the DBP free radicals. These free radicals probably initiate hydroxylated edge-edge interaction between the clay layers, which gives rise to a flocculated morphology and reduced polymer-clay interaction. There is a good correlation between these morphologies and the thermal stabilities and total crystallinities of the nanocomposites. Clay incorporation and peroxide treatment did not significantly change the tensile properties.

Keywords: nanocomposites, EVA, morphology, thermal properties, tensile properties

1. Introduction

Organic-inorganic hybrids based on layered inorganic compounds, such as clays, and organic polymers have been studied because of exceptional properties like increased modulus [1–3], reduced gas permeability [4, 5], and enhanced thermal stability [6, 7]. Dispersion of the silicate particles in the polymer matrix is improved by replacing the metal cations with ions bearing an aliphatic chain for compatibilizing the silicate. This compatibilization enhances its interaction with the polymer by enlarging the interlayer, and the compatibilized clay is known as an organoclay. In intercalated nanocomposites the penetration of the polymer matrix into the layered silicate occurs in a crystallographically regular fashion, regardless of the clay to polymer ratio [8]. In these nanocomposites the clay platelets are normally interlayered by a few

molecular layers of polymer. Hydroxylated edge-edge interaction of silicate layers results in flocculated nanocomposites, which are similar in nature to intercalated nanocomposites [9].

The exchange capacity of the clay, the polarity of the reaction medium and the chemical nature of the interlayer cations (e.g. onium ions) are a few factors that control whether a particular organoclay hybrid can be synthesized as an intercalated or exfoliated structure. Since clay nanocomposites are able to produce dramatic improvements in a variety of properties, it is important to understand the factors that affect delamination of the clay. In exfoliated nanocomposites, individual clay layers are separated in a continuous polymer matrix by an average distance that depends on clay loading. Usually the clay content of an exfoliated nanocomposite is much lower than that of intercalated nano-

*Corresponding author, e-mail: luytas@qwa.uovs.ac.za
© BME-PT and GTE

composites [9]. The formation of these structures is mainly determined by the preparation methods of the nanocomposites and by the characteristics of the monomer or polymer and clay. For melt blending, the polarity of the chains of the polymer and the basal spacing of the clay are important for the structure of these nanocomposites.

It has been reported [10] that a low (10%) amount of silicate added to the polymer is capable of dramatically reducing the influence of oxygen during thermo-oxidation, independent of whether the morphology is intercalated or exfoliated. Acid catalyzed deacetylation is, however, mostly observed in nitrogen and more evident in exfoliated structures [11]. A non-ionic dispersing agent helps to exfoliate alkylammonium modified montmorillonite into polyethylene, thus enhancing the tensile and gas barrier properties of the polymer. Amphiphilic copolymers intercalate organo-modified tactoids, hence increasing the d-spacing and decreasing the attraction between the silicate layers. This facilitates the exfoliation of highly anisometric layers that enhances the properties of nanocomposites [12].

In the present study, the effects of organic peroxides on the morphology, as well as thermal and tensile properties, of the nanocomposites have been investigated. For this, a fixed amount of organic peroxide was used. The composite samples were prepared by using melt blending followed by extrusion.

2. Experimental

2.1. Materials

Ethylene vinyl acetate copolymer (EVA) with 9% vinyl acetate (VA) content was supplied by Plastamid, Elsie's River, South Africa. The melting point of EVA was 95°C, and the density 0.930 g·cm⁻³.

Cloisite® 93A clay (hydrogenated tallow ammonium salts of Bentonite), supplied by Southern Clay Products, Texas, USA, was used as reinforcement. The as received clay particles were disk-like stacks of thin silicate layers, 1 nm thick and ranging in length from 100 nm to several micrometers. The specific gravity of the clay particles (stacks), according to the suppliers, is 1.6–1.8 g·cm⁻³.

Dicumyl peroxide (DCP) and dibenzyl peroxide (DBP), used as cross-linking agents, were obtained from Aldrich Chemicals (WI, USA).

2.2. Preparation of nanocomposites

The EVA and organoclay were dried in an oven at 80°C overnight. They were melt blended using a Brabender Plastograph (Brabender, Duisberg, Germany) 50 ml mixer followed by extrusion using a Brabender Plastograph (Brabender, Duisberg, Germany) single screw extruder. 1, 2 and 3% by weight of clay were mixed with EVA for respectively 20, 30 and 40 min. at 130°C and 60 r.p.m. For peroxide cured samples, 1% DCP or DBP was added after the initial mixing, followed by 5 min. mixing under the same conditions. The samples were then extruded at a screw speed of 60 r.p.m. at 130°C to obtain films with an average thickness of 0.45±0.05 mm and an average width of 15±1 mm.

2.3. Gel content determination

The gel content of the samples was determined using toluene as solvent. 1–2 g of each composite was wrapped in a stainless steel wire mesh (normal aperture 0.04 mm, wire diameter 0.04 mm) supplied by Meschape Industries in Edenvale, South Africa, and refluxed in the solvent for 12 hours, after which it was dried in an oven at 80±5°C, followed by drying in air overnight. The gel content was determined as shown by Equation (1):

$$\text{Gel content} = \frac{\text{mass of gel after solvent extraction}}{\text{initial sample mass}} \cdot 100 \quad (1)$$

2.4. X-ray diffraction analysis (XRD)

The degree of intercalation or exfoliation was evaluated using X-ray diffractometry (XRD). X-ray diffraction patterns of the nanocomposite samples were obtained using a D8 Advance X-ray Diffractometer with CuK_α radiation, λ = 1.5406 Å (Bruker AXS Inc., Madison, WI, USA). Detector: Na-I scintillation counter with monochromator. The analyses were done in the reflection mode between 2θ = 2 and 10°.

2.5. Tensile testing

A Hounsfield H5KS universal testing machine (Hounsfield, Redhill, England) was used to investigate the tensile strength, tensile modulus and elongation properties of the nanocomposites. Samples of 150 mm×15 mm×0.45 mm were cut for tensile testing. Samples with a gauge length of 50 mm were analyzed at a crosshead speed of 10 mm·min⁻¹. A continuous load-deflection curve was obtained. The averages and standard deviations of 5 tests per sample are reported.

2.6. Thermogravimetric analysis (TGA)

Thermogravimetric analysis was performed in a Perkin Elmer TGA7 thermogravimetric analyser (Perkin Elmer, Wellesley, MA, U.S.A.). The sample mass was 6–8 mg. The analyses were carried out from 30 to 600°C at a heating rate of 10°C·min⁻¹ under nitrogen atmosphere (flow rate 20 ml·min⁻¹).

2.7. Differential scanning calorimetry (DSC)

DSC analyses were performed in a Perkin Elmer DSC7 differential scanning calorimeter (Perkin Elmer, Wellesley, MA, U.S.A.). The analyses were carried out on 5–10 mg samples between 30 and 200°C at heating and cooling rates of 10°C·min⁻¹ under nitrogen atmosphere (flow rate 20 ml·min⁻¹). The onset and peak temperatures of melting, as well as melting enthalpies, were obtained from the second heating cycle.

2.8. Scanning electron microscopy (SEM)

SEM analyses of the nanocomposites were performed using a JEOL WINSEM-6400 electron microscope (JEOL Ltd., Tokyo, Japan). The probe size was 114.98 nm, the probe current 0.02 nA, the noise reduction 64 Fr and the AC voltage 5.0 keV. The surfaces of the samples were coated with gold by an electrode deposition method to impart electrical conductivity before recording the SEM micrographs.

2.9. SEM-EDX (energy dispersive X-ray diffraction)

The SEM-EDX analyses were done in a Shimadzu SSX-550 scanning electron microscope (Shimadzu

Corporation, Kyoto, Japan) at an AC voltage of 15.00 kV and a working distance of 17 mm. SEM-EDX pictures were taken from the same area as the SEM pictures.

2.10. Transmission electron microscopy (TEM)

The samples were prepared using cryo-ultramicrotomy. They were mounted on cryo-pins and frozen in liquid nitrogen. Sections were cut at –100°C using a Reichert FCS (Leica, Vienna, Austria) attached to a Reichert Ultracut S Ultramicrotome. The sections (100–150 nm thick) were collected on copper grids and viewed in a LEO 912 Omega (Carl Zeiss NTS GmbH, Oberkochen, Germany) transmission electron microscope, with an energy filter, operating at 120 kV.

3. Results and discussion

The purpose of this work was to try and establish whether introduction of an organic peroxide to the molten polymer-clay mixture will influence clay delamination and dispersion in the polymer matrix. Such influence may be the result of grafting between the polymer and clay, or crosslinking of the polymer. Although it is known [1] that clay exfoliates better into higher vinyl acetate (VA) containing EVA, we used 9% VA containing EVA so that any effect of the peroxide will not be overshadowed by a strong interaction between the EVA and clay modifier. Dicumyl peroxide (DCP) was used as crosslinking initiator at a temperature well below its optimum decomposition temperature (1 h half-life at 136°C), while dibenzoyl peroxide (DBP) was used at a temperature above its optimum decomposition temperature (1 h half-life at 91°C). Although the DCP may not have decomposed completely under the nanocomposite preparation conditions, there would have been enough decomposition to supply free radicals to the already mixed EVA/organoclay nanocomposites.

The XRD spectra of all the investigated samples are shown in Figure 1 and the 2θ and associated d -spacing values for the clay (001) peaks are summarized in Table 1. Figure 1a compares the spectrum of the pure clay with those of the 1% clay containing composites prepared in the absence and presence of DCP and DBP. The clay shows a (001)

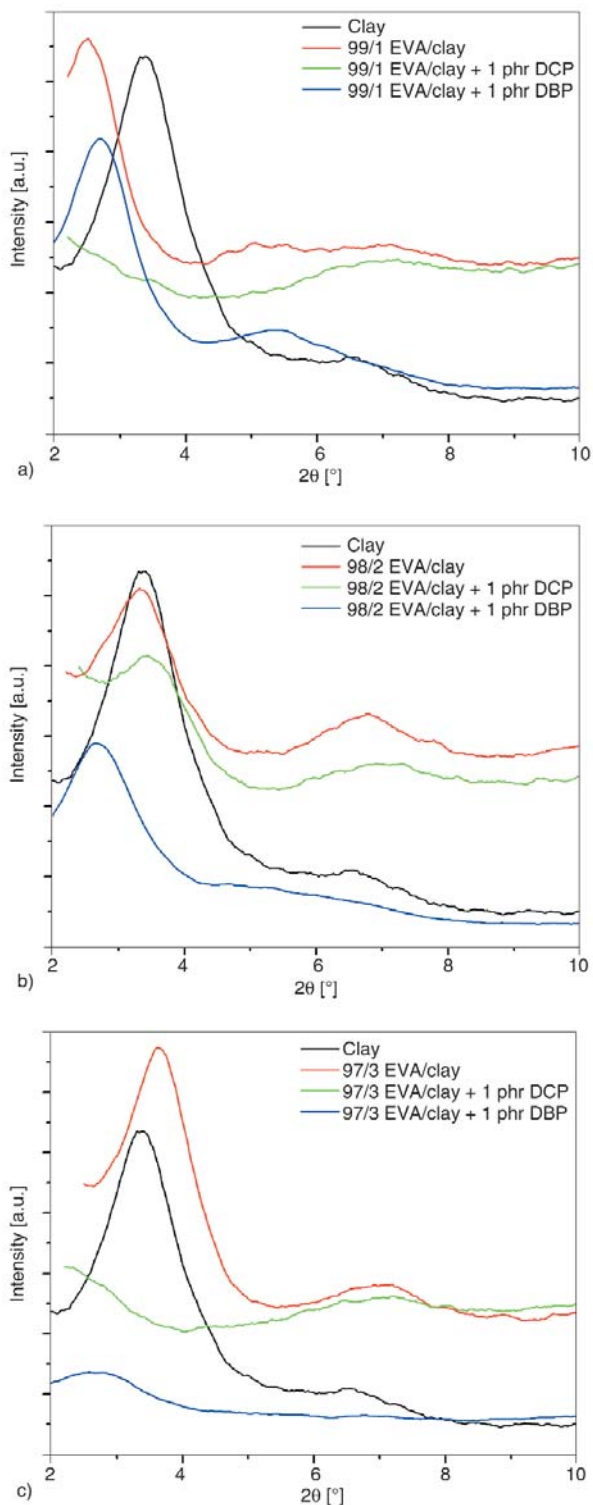


Figure 1. XRD spectra of EVA/clay (absence and presence of 1% peroxide) containing (a) 1% Cloisite 93A, (b) 2% Cloisite 93A, and (c) 3% Cloisite 93A

diffraction peak at $2\theta = 3.4^\circ$ which corresponds to a d -spacing of 2.6 nm, while the EVA/clay sample, containing 1% clay and prepared in the absence of an organic peroxide, shows possible intercalation

Table 1. 2θ and d -spacing values of the (001) diffraction peak of the clay in the different nanocomposites

Sample	2θ [°]	d -spacing [nm]
Clay	3.4	2.6
EVA/clay (1%)	2.4	3.7
EVA/clay (1%)/DCP	no peak	–
EVA/clay (1%)/DBP	2.7	3.3
EVA/clay (2%)	3.3	2.7
EVA/clay (2%)/DCP	3.4	2.6
EVA/clay (2%)/DBP	2.6	3.4
EVA/clay (3%)	3.6	2.5
EVA/clay (3%)/DCP	no peak	–
EVA/clay (3%)/DBP	2.6	3.4

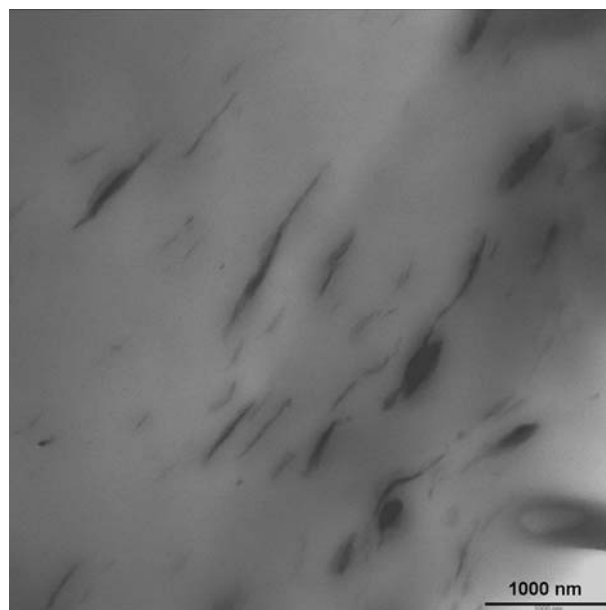


Figure 2. TEM image of a 3% clay containing sample prepared in the absence of peroxide

with an increase in d -spacing to 3.7 nm. In the case of the samples containing 2% (Figure 1b) and 3% (Figure 1c) clay there seems to be no intercalation or exfoliation of the clay in EVA. This was expected as a result of the known weak interaction between organoclay and EVA with low VA content. It is, however, possible that minimal intercalation also occurred in the case of the 1% clay containing sample, because it has been shown that XRD is not a very reliable technique for establishing clay intercalation/exfoliation at low clay contents [13]. This observation is supported by the TEM image in Figure 2 that show the clay particles with little evidence of intercalation and no exfoliation.

For the samples prepared in the presence of DCP there seems to be a much stronger interaction between the EVA and clay. The 1% clay containing

Table 2. Gel content values for samples prepared in the presence of DCP and DBP respectively (mass % of clay initially mixed into sample was subtracted)

Sample	Gel content [%]
Pure EVA	0.2
99/1 w/w EVA/clay + 1 phr DCP	0.4
99/1 w/w EVA/clay + 1 phr DBP	5.9

samples show no (001) diffraction peaks (Figure 1a), indicating exfoliation into the EVA matrix. Gel content measurements on the samples show no gel formation and therefore no, or very little crosslinking, of EVA in the presence of DCP (Table 2). We assume that any available peroxide free radicals may have initiated some form of interaction between the EVA chains and the clay. A suggested mechanism will involve hydrogen abstraction from polymer chains and clay –OH groups by peroxide free radicals, followed by grafting between polymer chains and clay platelets. In the case of the samples containing 2% (Figure 1b) and 3% (Figure 1c) clay there seems to be partial exfoliation (smaller (001) peaks), but no intercalation. The absence of intercalation supports the idea that the polymer interacts with the clay without penetrating the clay layers [14]. The absence of complete exfoliation is the result of increasing clay:DCP ratios, giving rise to reduced interaction between the EVA chains and the clay. Figure 3a shows good exfoliation of the DCP treated, 1%

clay-containing samples, although some small tactoids are visible. Figure 3b does not only show fairly good exfoliation of the clay in the polymer matrix, but also very obvious orientation of the clay platelets in the extrusion direction.

Nanocomposite samples prepared in the presence of DBP show completely different morphologies from those prepared in the presence of DCP (Figure 1). In this case a mixed morphology is clearly observed. The 2θ values of the (001) diffraction peaks are lower, while there is a development of a second peak at higher 2θ values. There are different views as to what may give rise to this additional (001) diffraction peak. Sinha Ray and Okamoto [9] attribute it to flocculation of clay layers caused by hydroxylated edge-edge interaction, while Galimberti *et al.* [14] discuss the possibility that such a peak could appear under certain preparation conditions, and is not necessarily the result of flocculation. The TEM images in Figure 4 indicate a mixed morphology. It is not completely clear why the presence of DBP, which certainly was completely decomposed under the preparation conditions used, did not give rise to exfoliation as in the case of DCP treated samples. The gel content results (Table 2) show the formation of gel when DBP was introduced in the samples, but the extent of gelation is still much lower than expected. In this case there may have been stronger interactions between the polymer and the clay, but there was also polymer crosslinking and possibly hydroxylated edge-edge

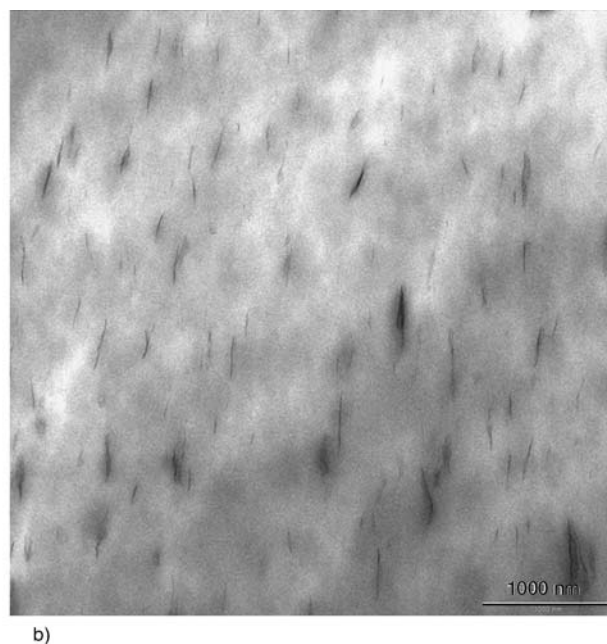
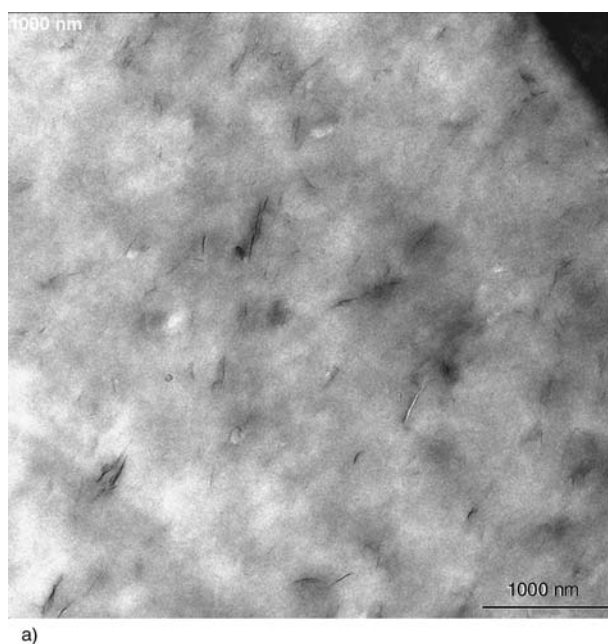


Figure 3. TEM images of (a) 1% clay and (b) 3% clay containing samples prepared in the presence of DCP

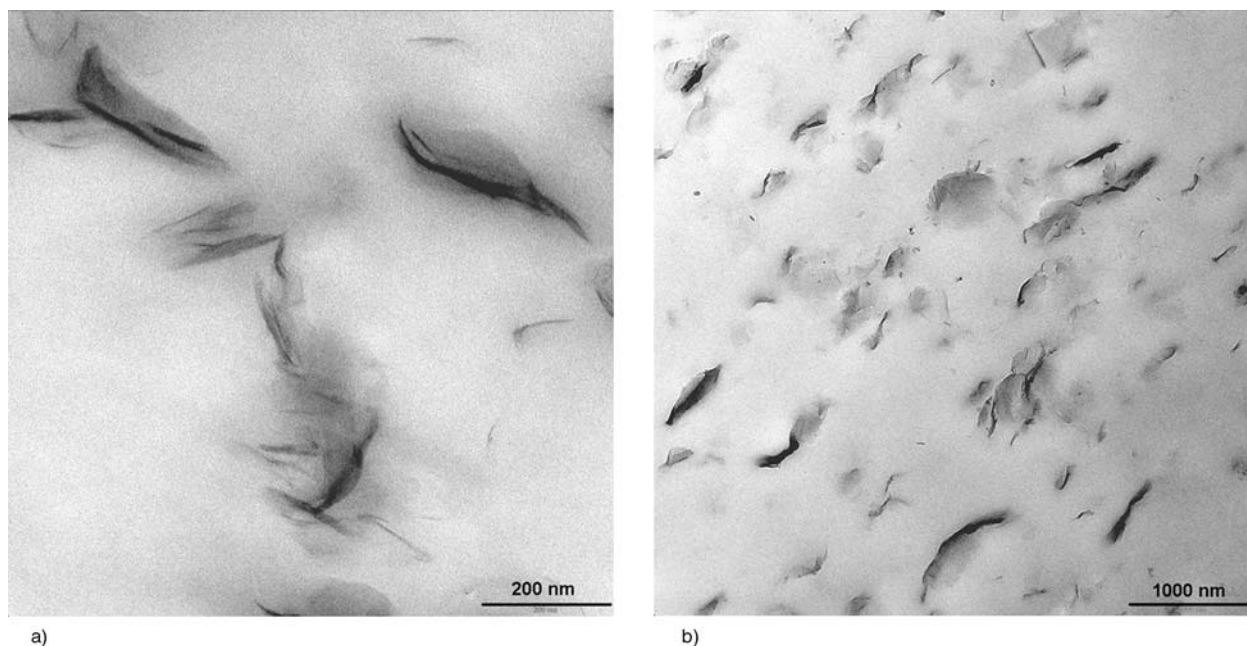


Figure 4. TEM images of (a) 1% clay and (b) 3% clay samples prepared in the presence of DBP

interactions between the clay layers. A combination of these reactions and resulting interactions then gave rise to the observed mixed morphology.

SEM and SEM-EDX images of EVA/clay with DCP are shown in Figure 5. These images show regular leaflet patterns. The SEM-EDX image (Figure 5b), showing silica (in light grey) along the lines of the pattern, indicates a higher clay concentration on the edges of the pattern. We assume that this pattern is the result of some roughness on the surface of the die, combined with the shear forces of extrusion and the attraction forces between the matrix and the clay.

The TGA curves (Figure 6) show a two-step degradation of the nanocomposites. The onset temperature of the first step was found to be in the range of 315–335°C, which corresponds to the release of acetic acid. At temperatures above 380°C, thermal degradation of the ethylene-co-acetylene main chain takes place [11]. The TGA curves clearly show that pure EVA is thermally more stable than any of the nanocomposites, whether prepared in the absence or presence of peroxide. The thermal decomposition of organo-modifier will generate strong acidic sites that will accelerate the deacetylation of EVA in the nanocomposites. These sites

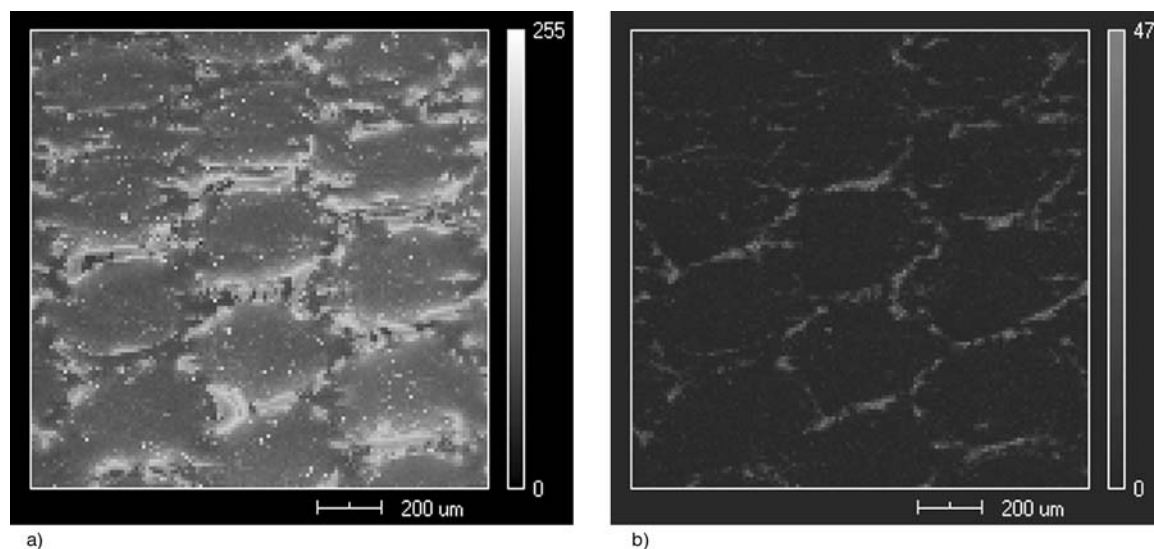


Figure 5. (a) SEM and (b) SEM-EDX images of a 3% clay containing sample prepared in the presence of DCP

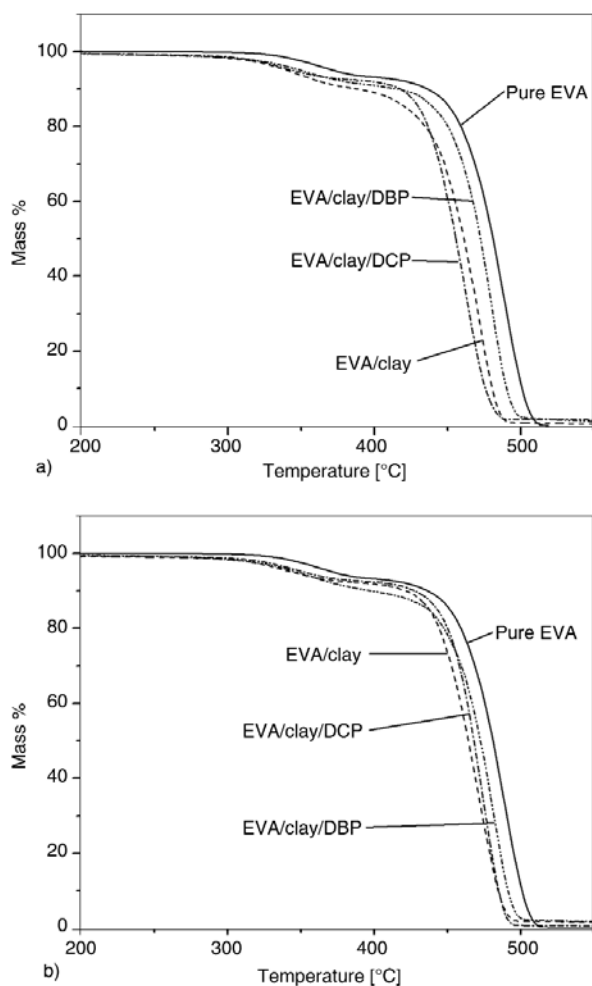


Figure 6. TGA curves of (a) EVA/Cloisite 93A (1%) and (b) EVA/Cloisite 93A (3%) prepared in the absence and in the presence of 1% peroxide

are active when there is intimate contact between the polymer and the silicate layers [8]. This is probably the reason why the exfoliated samples of the DCP treated nanocomposites were the least thermally stable. The DBP treated nanocomposites were observed to have a mixed morphology,

including flocculation and the formation of tactoids. As a result the clay was not well dispersed within the polymer matrix, which reduced the influence of the acidic sites on the deacetylation of EVA. There was, however, no direct relationship between the thermal stability of the nanocomposites and the amount of clay.

Table 3 summarizes the peak temperatures of melting and crystallization, as well as the melting and crystallization enthalpies, of pure EVA and the nanocomposites. These values were obtained from the second heating and cooling cycles of the DSC analyses. The peak temperatures of melting and crystallization of EVA in the different samples show differences, but there is no trend or correlation with the observed morphology. The presence of clay, however, has an influence on the total crystallinity of the EVA matrix. When comparing the melting and crystallization enthalpies of pure EVA and EVA in the nanocomposites (Table 3), it is clear that the nanocomposites have 20–30% lower enthalpy values than pure EVA. It is further clear that the samples prepared in the presence of DBP have higher enthalpy values than those prepared in the presence of DCP. There is a good correlation between the enthalpy (which is an indication of total crystallinity) and the extent of intercalation or exfoliation (as indicated by the XRD and TEM results). The presence of clay, whether non-dispersed, intercalated, flocculated or exfoliated, clearly reduces the EVA chain mobility, resulting in a lower total crystallinity. In the presence of DCP there is more exfoliation, resulting in a much larger EVA-clay interphase which gives rise to more reduced chain mobility and lower total crystallinity. The lower extent of exfoliation, as well as the presence of flocculation, of the clay layers

Table 3. Peak temperatures of melting and crystallization, as well as melting and crystallization enthalpies, of the different nanocomposites

Sample	$T_{p,m}$ [°C]	ΔH_m [J·g ⁻¹]	$T_{p,c}$ [°C]	ΔH_c / J·g ⁻¹
Pure EVA	95.8	57.2	81.3	-65.4
EVA/ clay (1%)	95.7	46.9	78.5	-45.3
EVA/ clay (1%)/DCP	94.2	40.7	78.6	-34.6
EVA/ clay (1%)/DBP	93.7	46.4	79.1	-48.6
EVA/clay (2%)	96.5	45.6	78.8	-43.6
EVA/clay (2%)/DCP	93.7	40.2	76.9	-34.1
EVA/clay (2%)/DBP	95.3	46.4	81.3	-44.8
EVA/clay (3%)	96.5	44.2	79.9	-46.2
EVA/clay (3%)/DCP	93.2	44.3	77.3	-37.9
EVA/clay (3%)/DBP	95.2	47.2	81.3	-42.1

$T_{p,m}$ – peak temperature of melting; $T_{p,c}$ – peak temperature of crystallization; ΔH_m – melting enthalpy; ΔH_c – crystallization enthalpy

Table 4. Tensile properties of the different nanocomposites

Sample	$\sigma_b \pm s\sigma_b$ [MPa]	$E \pm sE$ [MPa]
Pure EVA	6.5 ± 1.5	24.8 ± 3.3
EVA/clay (1%)	6.9 ± 0.4	29.2 ± 1.9
EVA/clay (1%)/DCP	7.3 ± 1.6	29.0 ± 3.3
EVA/clay (1%)/DBP	6.0 ± 1.0	25.4 ± 2.8
EVA/clay (2%)	6.6 ± 0.2	28.0 ± 0.5
EVA/clay (2%)/DCP	7.1 ± 1.6	33.7 ± 4.7
EVA/clay (2%)/DBP	6.5 ± 0.4	26.8 ± 3.9
EVA/clay (3%)	6.0 ± 0.2	25.4 ± 2.3
EVA/clay (3%)/DCP	6.1 ± 0.5	25.9 ± 4.0
EVA/clay (3%)/DBP	6.4 ± 0.3	24.0 ± 0.7

σ_b – stress at break; E – Young's modulus

reduce the EVA-clay interphase and therefore have less influence on the polymer chain mobility. The total crystallinity of the DBP treated samples, as indicated by the melting or crystallization enthalpies, is therefore higher.

The tensile data are shown in Table 4. The tensile modulus of a polymeric material has been shown to improve when nanocomposites are formed with layered silicates [9]. This depends upon the nature of interaction between the polymer matrix and silicate layers. The tensile properties of the nanocomposites largely depend upon the amount and the nature of the filler present. In our case the presence of up to 3% Cloisite 93A clay in EVA had little influence on both the tensile strength and modulus of the samples. This is in line with earlier observations [15, 16], where up to 3% Cloisite 15A clay in the same EVA gave similar values for the tensile strength and modulus. Peroxide treatment also seemed to have little influence on these properties, although both the tensile strength and modulus are about 10–20% higher for the 1 and 2% clay containing samples prepared in the presence of DCP. These were also the only samples showing some degree of exfoliation.

4. Conclusions

The results discussed in this paper clearly show differences in the EVA-clay morphology of nanocomposites prepared in the absence of organic peroxides, and of those prepared in the presence of respectively DCP (which has a slow decomposition under the preparation conditions) and DBP (which should completely decompose under the preparation conditions). It seems as if DCP, under the

preparation conditions, much more improves the polymer-clay interaction than DBP. The presence of clay also seems to inhibit the initiation of crosslinking by the DBP free radicals, probably because these free radicals initiates hydroxylated edge-edge interaction between the clay layers, which gives rise to a flocculated morphology and reduced polymer-clay interaction. There is a good correlation between these morphologies and the thermal stabilities of the nanocomposites, as studied through TGA, the total crystallinity, as seen from the DSC melting and crystallization enthalpies. There is, however, little difference between the modulus and tensile strength values of the different samples.

Acknowledgements

The National Research Foundation (GUN 2070099) and the University of the Free State in South Africa are acknowledged for financial support. Dr Remy Bucher from iThemba LABS in Somerset West, South Africa did the XRD analyses.

References

- [1] Chaudhary D. S., Prasad R. Gupta R. K., Bhattacharya S. N.: Clay intercalation and influence on crystallinity of EVA-based clay nanocomposites. *Thermochimica Acta*, **433**, 187–195 (2005).
- [2] Ghosh A. K., Woo E. M.: Analyses of crystal forms in syndiotactic polystyrene intercalated with layered nano-clays. *Polymer*, **45**, 4749–4759 (2004).
- [3] Vaia R. A., Price G., Ruth P. N., Nguyen H. T., Lichtenhan J.: Polymer/layered silicate nanocomposites as high performance ablative materials. *Applied Clay Science*, **15**, 67–92 (1999).
- [4] Usuki A., Tugigase A., Kato M.: Preparation and properties of EPDM-clay hybrids. *Polymer*, **43**, 2185–2189 (2002).
- [5] Gilman J. W.: Flammability and thermal stability studies of polymer layered-silicate (clay) nanocomposites. *Applied Clay Science*, **15**, 31–49 (1999).
- [6] Zhang W., Chen D., Zhao Q., Fang Y.: Effects of different kinds of clay and different vinyl acetate content on the morphology and properties of EVA/clay nanocomposites. *Polymer*, **44**, 7953–7961 (2003).
- [7] Duquesne S., Jama C., Le Bras M. L., Delobel R., Recourt P., Gloaguen J. M.: Elaboration of EVA-nanoclay systems-characterization, thermal behaviour and fire performance. *Composites Science and Technology*, **63**, 1141–1148 (2003).
- [8] Zannetti M., Camino G., Thomann R., Mülhaupt R.: Synthesis and thermal behaviour of layered silicate-EVA nanocomposites. *Polymer*, **42**, 4501–4507 (2001).

- [9] Sinha Ray S., Okamoto M.: Polymer/layered silicate nanocomposites: A review from preparation to processing. *Progress in Polymer Science*, **28**, 1539–1641 (2003).
- [10] Riva A., Zanetti M., Braglia M., Camino G., Faliqi L.: Thermal degradation and rheological behaviour of EVA/montmorillonite nanocomposites. *Polymer Degradation and Stability*, **77**, 299–304 (2002).
- [11] Massa A., Scettri A., Contessa S., Bugatti V., Concilio S., Iannelli P.: New catalyst for the synthesis of poly(butylene terephthalate) with high thermo-oxidative stability. *Journal of Applied Polymer Science*, **104**, 3071–3076 (2007).
- [12] Zhang X., Guo F., Chen J., Wang G., Liu H.: Investigation of interfacial modification for flame retardant ethylene vinyl acetate copolymer/alumina trihydrate nanocomposites. *Polymer Degradation and Stability*, **87**, 411–418 (2005).
- [13] Százdí L., Ábrányi A., Pukánszky B. Jr., Vancso J. G., Pukánszky B.: Morphology characterization of PP/clay nanocomposites across the length scales of the structural architecture. *Macromolecular Materials and Engineering*, **291**, 858–868 (2006).
- [14] Galimberti M., Lostritto A., Spatola A., Guerra G.: Clay delamination in hydrocarbon rubbers. *Chemistry of Materials*, **19**, 2495–2499 (2007).
- [15] Guduri B. R., Luyt A. S.: Effect of ethylene glycidyl methacrylate compatibilizer on the structure and mechanical properties of clay nanocomposites modified with ethylene vinyl acetate copolymer. *Journal of Applied Polymer Science*, **103**, 4095–4101 (2007).
- [16] Guduri B. R., Luyt A. S.: Comparison of the influence of different compatibilizers on the structure and properties of ethylene vinyl acetate copolymer/modified clay nanocomposites. *Journal of Applied Polymer Science*, **105**, 3612–3617 (2007).

Synthesis and characterization of styrene-co-divinylbenzene-graft-linseed oil by free radical polymerization

V. Sharma^{1,2}, J. S. Banait², R. C. Larock³, P. P. Kundu^{1*}

¹Department of Chemical Technology, Sant Longowal Institute of Engineering & Technology, Sangrur, Punjab-148106, India

²Department of Chemistry, Punjabi University, Patiala, Punjab-147002, India

³Department of Chemistry, Iowa State University, Ames, Iowa 50011, USA

Received 1 January 2008; accepted in revised form 27 February 2008

Abstract. A variety of opaque white to light yellow polymeric material have been prepared by two methods, one copolymerization of styrene (ST), divinylbenzene (DVB), and grafting of linseed oil (LIN), and the second involves the copolymerization of the same comonomers with pre-reacted (with initiator) linseed oil. All of the reactant mixtures in different concentrations start to solidify at 100°C and give rise to a solid crosslinked polymer at 130°C. These polymeric materials contain approximately 30 to 74% of crosslinked materials. Their ¹H NMR spectra indicate that the polymeric samples contain both soft oily and hard aromatic segments. The insoluble material left after soxhlet extraction contains finely distributed micropores. The heat deflection temperatures (HDT) of the polymer samples range from 26 to 44°C. The glass transition temperature for different linseed oil polymer samples ranges from 66 to 147°C (from dynamic mechanical analysis) and 158 to 182°C (from differential scanning calorimetry). The crosslinking density of samples ranges from 35.0 to 6.01·10⁴ mol/m³. Irrespective of methods, the storage modulus decreases with increasing oil content in the copolymers. The polymers prepared by the first method show minimum swelling in saline water and maximum swelling in tetrahydrofuran. On the other hand, the polymers from the second method show maximum swelling in alkaline solution and a minimum in acidic solution.

Keywords: biopolymers, linseed oil, swelling ratio, copolymerization, transition temperature

1. Introduction

Linseed oil is a triglyceride oil consisting mainly of linolenic acid (53%), oleic acid (18%), linoleic acid (15%), palmitic acid (6%) and stearic acid (6%) [1]. Linseed oil is considered a good drying oil, used mainly for the preparation of paints and varnishes [2]. It is also used in enamels, linoleum, oilcloth, patent leather, printer's ink and as waterproofing for raincoats, slickers and tarpaulins [3].

Considerable research has been carried out on applications of linseed oil. In medicinal front, it is

claimed that linseed oil is useful in treating anxiety, prostate problems, vaginitis, weight loss and certain types of cancer [4], but appropriate research is lacking. To improve its film properties, different olefinic monomers, such as styrene, have been copolymerized with linseed oil [5–7]. Recently, it has been reported [8] that the reaction of styrene with drying oils depends on the number of conjugated double bonds present in the drying oil. Larock and coworkers have successfully prepared useful bioplastics from tung [9] and linseed oil [10]

*Corresponding author, e-mail: ppk923@yahoo.co.in
© BME-PT and GTE

by thermal copolymerization. Some bioplastics have also been prepared from soybean [11, 12], tung [13], and corn [14] oils by cationic copolymerization with varying amounts of styrene (ST) and divinylbenzene (DVB). Crosslinked bacterial polyesters have been obtained by the free radical polymerization of soybean oil acids [15]. Extensive research has been devoted to the development of polymers from triglyceride oils as a natural alternative to petroleum-based polymers [16–18]. In this work, common linseed oil is grafted free radically with ST and DVB to prepare a range of promising new polymers.

2. Materials and methods

2.1. Materials used

The linseed oil (LIN) used in this study was purchased from the local market. ST and DVB (stabilized with 4-*tert*-butylpyrocatechol) were purchased from Merck Chemical Co., Germany and used as received. Benzoyl peroxide (BPO) was purchased from CDH Ltd., New Delhi (India) and used as received. Tetrahydrofuran was purchased from Merck Chemical Co., Germany and used as a solvent for extraction.

2.2. Polymer preparation

The polymeric materials have been prepared by heating the desired concentration of linseed oil [LIN or Benzoyl peroxide initiated Linseed Oil (BLO)], ST and DVB in a glass vial. Two different methods for preparation of the polymeric materials have been adopted. In the first method, all of the materials were mixed in a vial in the desired amounts, stirred thoroughly and then the initiator BPO (1%) was added with stirring for proper dissolution. The material was heated sequentially to the desired temperatures for the appropriate amount of time, usually 85°C for 45 minutes, 100°C for 12 hours, 120°C for 24 hours and finally 130°C for 3 hours. When using the second method, the LIN was heated with 1% BPO at 120°C for five hours (henceforth known as BLO) and then ST and DVB were added to the oil and heated sequentially to the desired temperatures, usually 85°C for 45 minutes, 100°C for 12 hours, 120°C for 24 hours and finally 130°C for 3 hours. The nomenclature used in this work is based on the original composition of the

reactants. For example, LIN30-ST42-DVB28 represents a polymer prepared from 30 weight% of linseed oil (LIN), 42 weight% of ST and 28 weight% of DVB and BLO30-ST42-DVB28 represents a polymer prepared from 30 weight% of initiated linseed oil (BLO), 42 weight% of ST and 28 weight% of DVB.

3. Characterization

3.1. Soxhlet extraction

The polymeric materials reported in Table 1 were subjected to soxhlet extraction to determine their soluble and insoluble contents. About 2 gram sample of the bulk polymer was extracted for 24 hours with 150 ml of refluxing tetrahydrofuran using a soxhlet extractor. After extraction, the resulting solution was concentrated by rotary evaporation and subsequently dried under vacuum. The insoluble materials were dried under vacuum for several hours before weighing.

3.2. ¹H nuclear magnetic resonance spectroscopy (¹H NMR)

The soluble extract from the polymeric material, as well as LIN, ST and DVB were dissolved in CDCl₃. Tetramethylsilane (TMS) was used as a reference to compare the spectra obtained. The spectra were obtained using a multinuclear FT-NMR Spectrometer (Bruker AC-300 F) at 300 MHz. A total of 30 scans were averaged to obtain the final data.

3.3. Dynamic mechanical analysis (DMA)

The dynamic mechanical analysis of the properties of bulk polymers were conducted by using a Perkin-Elmer dynamic mechanical analyzer DMA Pyris-7e in a three-point bending mode with a 110 mN static force and a 110 mN dynamic force. A rectangular specimen was prepared by machining the cylindrical product (obtained from heating in a vial) to specimens of 1.2–2 mm thickness and 5 mm depth. Each specimen was first cooled under liquid nitrogen to ca. –60°C, and then heated at 3°C/min and at a frequency of 1 Hz under nitrogen. The viscoelastic properties, i.e. storage modulus E' , and mechanical loss factor (damping) $\tan\delta$ were recorded as a function of temperature. The glass transition temperature T_g of the polymer was

Table 1. Compositions of the crosslinked linseed oil-ST-DVB copolymers from soxhlet extraction and ¹H NMR spectroscopic studies

Sample	Polymer	Soluble extracts ^a		Soxhlet results	
		Weight% of oil	Weight% of ST and DVB	Soluble ^b [wt%]	Insoluble ^c [wt%]
C ₁	LIN30-ST42-DVB28	97.25	2.75	26.1(25.38 0.72)	73.9(4.62 69.28)
C ₂	LIN35-ST39-DVB26	98.48	1.52	33.6(33.09 0.51)	66.4(1.91 64.49)
C ₃	LIN40-ST36-DVB24	97.33	2.67	38.8(37.76 1.04)	61.2(2.24 58.96)
C ₄	LIN45-ST33-DVB22	98.27	1.73	45.1(44.22 0.89)	54.9(0.88 64.11)
C ₅	LIN50-ST30-DVB20	97.80	2.20	49.5(48.41 1.09)	51.5(1.59 48.91)
C ₆	LIN55-ST27-DVB18	97.68	2.32	54.1(52.84 1.26)	45.9(2.16 43.74)
C ₇	LIN60-ST24-DVB16	97.34	2.66	59.9(58.31 1.59)	40.1(1.69 38.41)
C ₈	LIN65-ST21-DVB14	98.93	1.07	63.4(62.72 0.68)	36.6(2.28 34.32)
B ₁	BLO30-ST42-DVB28	94.59	5.41	30.3(28.39 1.91)	69.7(1.61 68.09)
B ₂	BLO35-ST39-DVB26	91.24	8.76	38.7(34.47 4.23)	61.3(0.53 60.77)
B ₃	BLO40-ST36-DVB24	91.93	8.07	43.5(39.55 3.95)	56.5(0.45 56.05)
B ₄	BLO45-ST33-DVB22	90.62	9.38	48.5(43.95 4.55)	51.5(1.05 50.45)
B ₅	BLO50-ST30-DVB20	88.61	11.39	55.6(49.21 6.39)	44.4(0.79 43.61)
B ₆	BLO55-ST27-DVB18	92.05	7.95	59.5(54.77 4.73)	40.5(0.23 40.27)
B ₇	BLO60-ST24-DVB16	86.23	13.77	68.3(58.90 9.40)	31.7(1.10 30.60)
B ₈	BLO65-ST21-DVB14	91.86	8.14	70.2(64.49 5.71)	29.8(0.51 29.29)

^aMicrocomposition of the extracted soluble materials calculated from the ¹H NMR spectra of the glyceride peak at 4.1 ppm and the aryl CH peak at 7 ppm. ^bThe data in parentheses have been calculated directly from the wt% of oil and wt% of aromatics in the soluble extract. The first value in the parentheses represents the % oil content and the second value represents the % aromatic content. ^cThe data in the parentheses have been calculated indirectly from the wt% of the oil and aromatic content in the soluble extract, as the total mass of the soluble and insoluble portions are held constant. The first value in the parentheses represents the % oil content and the second value represents the % aromatic content.

obtained from the peak of the loss tangent plot. The crosslink densities, ν_e , were determined from the rubbery modulus plateau based on the theory of rubber elasticity (Equation (1)) [19, 20]:

$$E' = 3\nu_e RT \quad (1)$$

where E' is the storage modulus (Young's) of crosslinked polymer in the plateau region, R is the universal gas constant ($8.314 \text{ J}\cdot\text{mole}^{-1}\cdot\text{K}^{-1}$) and T is the absolute temperature [K].

Since the three point bending mode was used for all dynamic measurements, the storage modulus obtained is a flexural modulus, which is related to Young's modulus as Equation (2) [21, 22]:

$$E' = \frac{12D'(1-\nu^2)}{h^3} \quad (2)$$

where D' is the flexural storage modulus (flexural rigidity) per unit width; ν is Poisson's ratio and h is the thickness of the specimen. For simplicity and ease of comparison with the previously published results [11], Equation (1) has been used to calculate

the crosslink density, assuming that E' and D' are equal.

3.4. Differential scanning calorimetry (DSC)

Differential scanning calorimetric studies were carried out by using a differential scanning calorimeter (TA Instruments DSC Q10 V9.0 Build 275) in the temperature range of 35 to 250°C at a heating rate of 20°C/min. The sample weight used was approximately 4–5 mg. The peaks were used to determine the glass transition temperature T_g of the samples which is approximately 20 to 40°C higher than T_g shown by loss tangent plot. The area in J/gm was also reported by integrating the peak from DSC results and peak width was calculated from the difference between starting point and finishing point of the DSC peak for each sample.

3.5. Scanning electron microscopy (SEM)

The polymeric samples to be scanned were mounted onto the specimen stub. The samples were sputter coated with a thin layer (approximately 25 nm) of gold under a vacuum by using a JEOL Sputter

Coater (JFM 1100). The metal coating prevents the buildup of high voltage charges on the specimen. In addition, the metal coatings serve as an excellent source of secondary electrons, as well as helping to disperse potentially damaging heat. The coated samples were examined using a JOEL scanning electron microscope (JSM 6100) at a 20 kV accelerating voltage and the images were recorded on 120 B and W Roll Film (100 ASA).

3.6. Heat deflection temperature (HDT)

The heat deflection temperatures of the polymeric samples were measured according to ASTM D 648. The dimensions of the samples were 80×10×4 mm. They were tested in a flatwise position. For the HDT measurements, the samples were heated from room temperature to 170°C at a rate of 2°C per minute. A load of 450 kPa was applied to the sample at the center. Once the sample was deflected by 0.25 mm, the temperature was noted. This is the heat deflection temperature (HDT) of the sample.

3.7. Swelling analysis

The swelling analyses of the polymeric samples were carried out in different solvents *viz.*, saline (20% NaCl), alkaline (2% NaOH), acidic (2% H₂SO₄) and tetrahydrofuran. To study the swelling kinetics, the so-called pat-and-weight technique was used for liquid sorption [23]. The polymeric samples were allowed to remain in the solution for 72 hours at room temperature and then weighed as soon as they were removed from the solvent. The samples were weighed after 2, 4, 8, 12, 24, 48 and 72 hours. The swelling ratio, q_v , of the various polymers at equilibrium [24] was determined using the Equation (3):

$$q_v = \frac{\text{volume of swollen polymer}}{\text{volume of dry polymer}} \quad (3)$$

4. Results and discussion

4.1. Microstructure of the LIN-ST-DVB copolymers

Sixteen polymer samples, in total, were prepared by the free radically grafted copolymerization of varying amounts of LIN, ST and DVB as reported

in Table 1. The possible initiation reactions for this free radical process are shown in Figure 1. It is observed that the LIN employed in this study is oligomerized on heating and becomes viscous at 160°C or higher. No crosslinked polymers are evident at 160°C, but upon standing for several days at room temperature, this oil forms an upper solid surface. This indicates that the LIN polymerizes in the presence of oxygen. Thus, the formation of crosslinked homopolymers from LIN probably depends on the conditions employed, namely the thickness of the surface layer, the temperature and the time of reaction with surface oxygen, etc. It is also observed that when this heated oil is mixed with equal amounts of ST and left for some days at room temperature, it also forms a solid upper surface. Thus, in order to get a viable product of considerable strength within some stipulated time, it is important that one mixes the LIN with some more thermally active reactants, like ST and DVB.

The activation temperature for the free radical copolymerization of ST and DVB is much lower than that of LIN. Both ST and DVB undergo polymerization at 100°C, resulting in hard rigid solid material. Based on the above findings, the mixture of LIN, ST and DVB was successively heated at 85°C for 45 minutes, then 100°C for 12 hours, 120°C for 24 hours, and finally at 130°C for 3 hours. During the heating at 100°C, all of the reactant mixtures (C₁–C₈ and B₁–B₈ of Table 1) solidified within two hours of heating. Thus, a reasonable mechanism for initiation may involve formation of the radicals **2** and **3** from ST and DVB after decomposition of the initiator. These radicals are then capable of attacking the C=C bonds of the ST, DVB and LIN. After post curing at 130°C, almost all of the starting materials are converted into crosslinked polymers. It is expected that the radicals **2** and **3** generated as shown in Figure 1 will form relatively stable radicals by adding either to ST or DVB. During prolonged heating, the ST-DVB copolymer chains crosslink at the pendant vinylic double bonds and the rest of the pendant vinylic double bonds react with many unreacted of double bonds in the LIN, leading to a crosslinked polymer having two distinctly separated soft and hard phases. The radical **5** is more pronounced and may result in grafting (**6**) of LIN in the ST-DVB polymer chain. The soft phase is comprised mainly of the LIN copolymer, whereas the hard phase con-

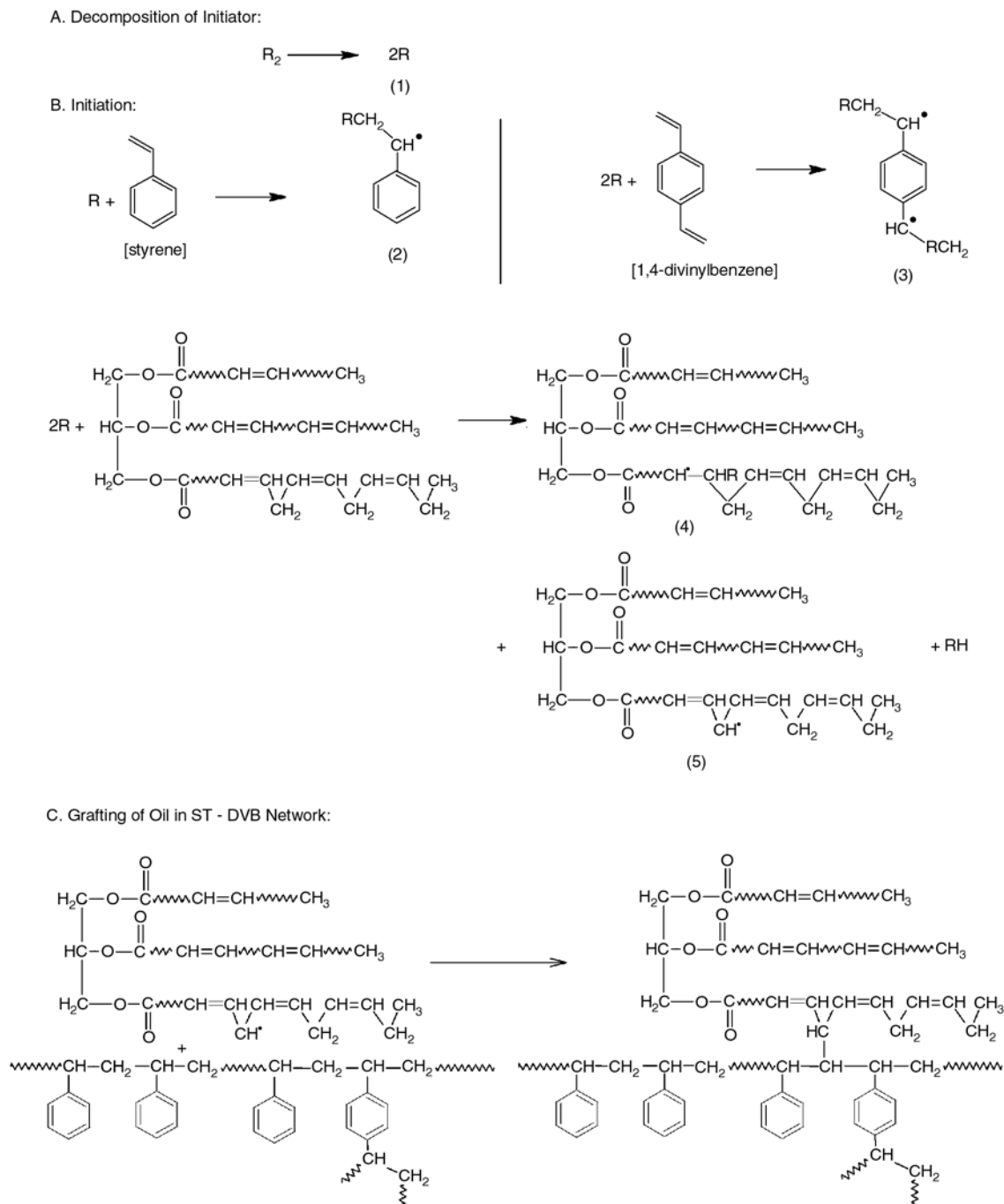


Figure 1. The possible initiation reactions for this free radical process

sists primarily of ST-DVB copolymer. There is a strong possibility of seeing phase separation (macroheterogeneity) between these two phases, leading to some fault or defect-like cracks in the bulk and surface when relatively few dangling vinylic double bonds from the ST-DVB copolymer are available for grafting with the double bonds of the fatty acid chains of the LIN. This condition prevails when a very low amount of DVB (<14%) is present in the mixture. Thus, the sample C₈, con-

taining the least DVB (14%) exhibits no visible phase separation.

Apparently, the aromatic comonomers (ST and DVB) upon crosslinking strengthen the copolymer chains and thus make the resulting fully cured polymers more viable as structural materials. As noted earlier, when the DVB concentration is not sufficiently high, there is a strong possibility of agglomerating soft and hard phases forming clusters among themselves, leading to macrophase separa-

tion. The macrophase separation induces cracks in the products, along with the separation of white crosslinked ST-DVB copolymer. With 20% DVB content (C_5 of Table 1), both soft and hard phases are still present in the product, but the formation of an oil-grafted ST-DVB copolymer prevents the formation of clusters. Thus, macroheterogeneity reduces to microheterogeneity, which is indicated by the opaque nature of the material.

Based upon the above results, different concentrations of LIN were added to a 3:2 mixture of ST and DVB. It is observed that for a LIN concentration of 30–65% (C_1 – C_8), the samples are free of cracks. An increase in the DVB content results in the formation of more highly crosslinked copolymers of LIN, further reducing the possibility of macrophase separation.

4.2. Soxhlet extraction

The polymer samples were extracted to determine their insoluble content and these results are shown in Table 1. With an increase in the LIN content in the polymeric samples from 30 to 65%, the insoluble content of the samples decreases from 74 to 30%, while the soluble portion increases from 26 to 70%. A plot of the percentage of the LIN vs. the soluble content of the sample is shown in Figure 2. These results indicate that with an increase in the LIN content, the crosslinking densities of the polymeric samples decrease. The polymer samples prepared by the first method have less soluble content as compared to the samples prepared by the second

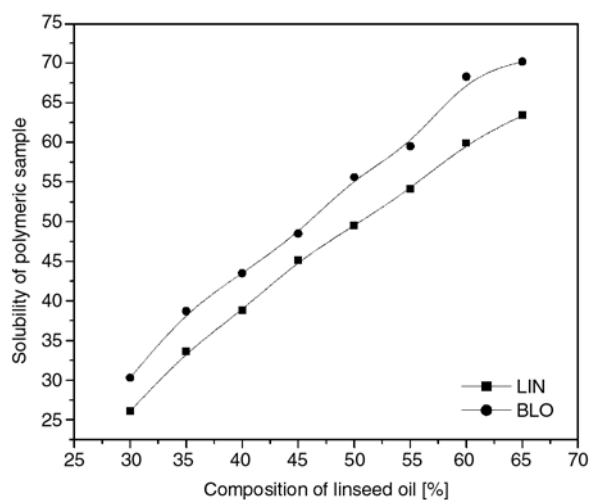


Figure 2. Variation in solubility of the LIN polymers with increasing LIN content

method, which indicates that the crosslinking densities of samples prepared by the second method are less than that prepared by the first method. In the second method, the initiator is first allowed to react with the LIN, may cause the formation of peroxy-linkages, which subsequently cause the degradation, as well as crosslinking. The presence of the higher soluble contents in the polymers from this second method may be due to this degradation process. It may be caused also because of partial blocking of double bonds with radicals produced by the initiator as well as radical recombination. In such case more active pre-initiated double bonds of the oil are falling out of the following copolymerization process.

4.3. ^1H NMR spectroscopic characterization

The ^1H NMR spectra of ST, DVB, LIN, solvent removed from extractable portion of the polymer (vacuum rota-evaporator) and the soluble extract from the polymeric samples C_5 (LIN50-ST30-DVB20) and B_5 (BLO50-ST30-DVB20) are shown in Figure 3. The extracts from C_5 and B_5 are representative of the soluble extracts obtained from all other samples (C_1 – C_4 and B_1 – B_4). The peaks at 2.8 ppm are due to the methylene (CH_2) protons present in between the two unsaturated $\text{C}=\text{C}$ double bonds of the fatty acid chain. The presence of a similar peak in the DVB is due to the presence of

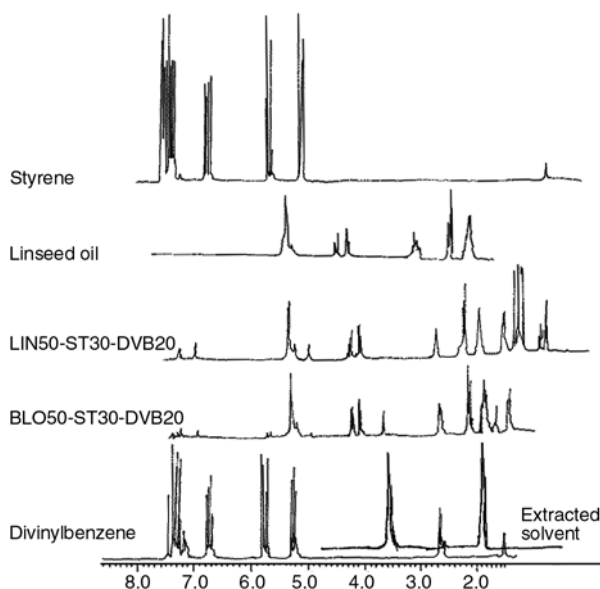


Figure 3. ^1H NMR spectra of DVB, extracts of the samples B_5 (BLO50-ST30-DVB20) and C_5 (LIN50-ST30-DVB20), LIN and ST

methylene protons in the ethylvinylbenzene, which is present to the extent of about 20% in the DVB. The peaks for the vinylic (C=C-H) protons of the linseed oil, ST and DVB are present at 5.1–5.8 ppm. The peaks at 4.1–4.5 ppm in the soluble extract (C₁–C₈ and B₁–B₈) (samples C₅ and B₅ are shown in Figure 3) and in LIN are due to the methylene protons (CH₂) of the glyceride unit. This is a particularly characteristic peak for the LIN oil. It is used in calculating the oil content in the soluble extract of the polymeric material. The aromatic protons of the ST, DVB and the oligomeric portion of these materials are observed between 7.1–7.9 ppm. These aromatic peaks are distinctive and are used to calculate the ST and DVB content in the soluble extracts. However, the peak due to the solvent CDCl₃ peak, which occurs in the same region at 7.26 ppm, has been excluded from all calculations. The solvent removed from the soluble portion by vacuum evaporation is free from any oligomers and the peak is shown in Figure 3. The peak is same as for pure solvent.

The weight percentages of the oil and aromatic components of the different samples are reported in Table 1. The weight percent of the LIN in the soluble extract varies from 86 to 99% and the weight percent of aromatic components varies from 1 to 14%. The values in parentheses in the Soxhlet results of Table 1 indicate the detailed microcomposition of the polymeric samples. The soluble portion present in the samples helps plasticize the crosslinked insoluble materials. Thus, the insoluble materials mainly determine the properties of the polymeric material. For the samples C₁–C₈ and B₁–B₈ in Table 1, the amount of oil decreases in the insoluble fraction, but the decrease is more significant in samples B₁–B₈. With the decrease in DVB content from 28 to 14%, the amount of oil in the insoluble portion shows a considerable decrease. This fact is consistent with our hypothesis that the

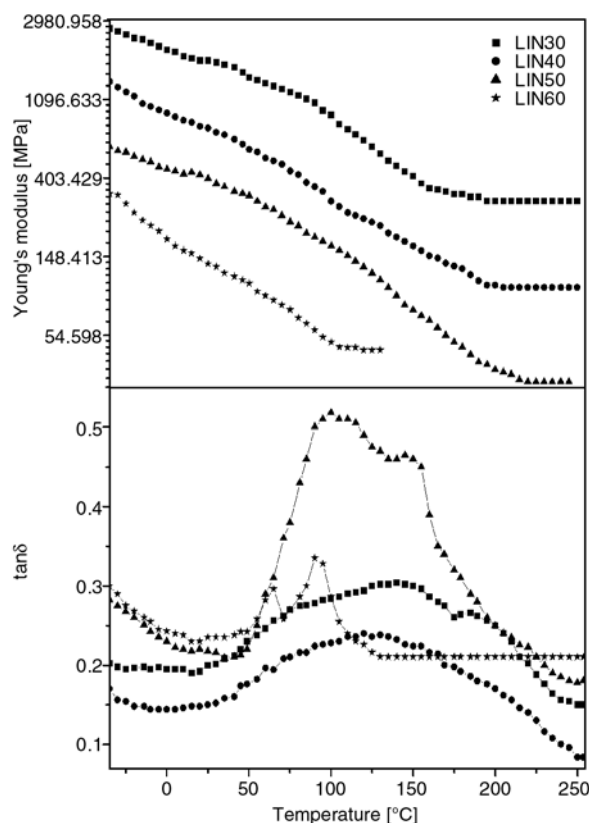


Figure 4. tanδ and storage modulus with temperature for LIN polymer samples (C₁, C₃, C₅, and C₇)

LIN is grafted into the polymer chain of the ST and DVB copolymer during prolonged heating.

4.4. Dynamic mechanical analysis

Figure 4 shows the variation of tanδ and storage modulus with temperature for different linseed oil polymer samples (C₁, C₃, C₅, and C₇). The glass transition temperatures were obtained from the tanδ peaks and the crosslink densities were calculated from the plateau storage moduli using Equation (1). These are listed in Table 2. From the tanδ plots of Figure 4, the presence of a hump or two peaks in all of the samples except C₁ and C₃ indicates that there

Table 2. Dynamic mechanical and thermal properties of crosslinked linseed oil-ST-DVB copolymers

Sample	Polymer composition	DMA results		DSC results			HDT results
		T _g [°C]	v _c [10 ⁴ mol/m ³]	T _g [°C]	Area [J/gm]	Peak width ^a	
C ₁	LIN30-ST42-DVB28	141–146	21.00	181.28	31.70	120.57	43.6
C ₃	LIN40-ST36-DVB24	121	8.28	180.73	46.19	104.17	35.9
C ₅	LIN50-ST30-DVB20	100 and 146.5	6.01	178.34	62.74	99.51	31.3
C ₇	LIN60-ST24-DVB16	66 and 91	8.60	158.86	96.03	86.10	26.9
B ₅	BLO50-ST30-DVB20	50.6 and 70.5	35.00	164.31	76.93	83.06	–

^aDifference between starting and finishing temperature of the peak

is clearly phase separation between the soft oily phase and the hard aromatic phase. The peaks for sample C₁ and C₃ get merged due to the broadening of the hump. It was reported that the glass transition temperature peaks for rubbery materials appears in negative region [10]. In present work, the glass transition peaks for all samples are appearing above the room temperature. The crosslink densities of these samples are quite high, which suggests that these polymers should be hard plastics. But from visual inspection, it appears that these samples are neither plastics nor elastic, but to some extent waxy in nature. These observations indicate that these samples are crosslinked as well as degraded (the presence of atmospheric oxygen causes degradation). That is why these samples show high glass transition temperature.

With increase of oil contents in these polymers, it is observed that the strength of these samples is very low, when compared with the polymeric samples from thermal polymerization of conjugated linseed oil reported by Kundu and Larock [10]. The possible explanation is the simultaneous crosslinking and degradation of polymer chains. This leads to the formation of highly crosslinked small polymeric chains giving rise to high T_g s and crosslink densities (v_e). The crosslink densities (v_e) of these samples (C₁, C₃, C₅, and C₇) are plotted in Figure 5. The crosslink density of C₁ is the highest and decreases with increasing oil contents upto sample C₅. From sample C₅ onwards v_e start decreasing again which suggest that as the linseed oil contents increased beyond 50%, the degradation of linseed

oil dominates. This results in highly crosslinked small polymer chains. The samples B₅ (not shown in Figure 5) shows highest v_e and is more waxy than C₇ (LIN 60%).

In considering the storage modulus plots of these polymers, it is observed that the storage modulus at high temperature (>50°C) is higher for samples containing less linseed oil and it decreases with increasing oil contents. In samples C₅ and B₅, sample B₅ show high modulus at low temperature (< -5°C) and sample C₅ shows high modulus at temperature higher than 20°C. This may be due to the reason that, in sample B₅, the initiator oligomerizes the oil first and a few peroxy radical left for polymerizing other comonomers. Also, the molecular size of linseed oil is larger than the one of BPO. Thus the BPO treated linseed oil molecules have less reactivity and less diffusability as compared to BPO. Due to this, the polymerization is lower in sample B₅ than C₅.

4.5. Differential scanning calorimetry

The plots of heat flow [W/g] versus temperature [°C] for different samples are shown in Figure 6. The differential scanning calorimetry results are shown in Table 2. It seems that the polymers show their transitions in a specific temperature range where some chemical reaction may also occur. Thus, the glass transition appears in the range of 164–181°C (higher by 40–90°C from the transition temperature shown by the samples by dynamic mechanical analysis). But these transitions are

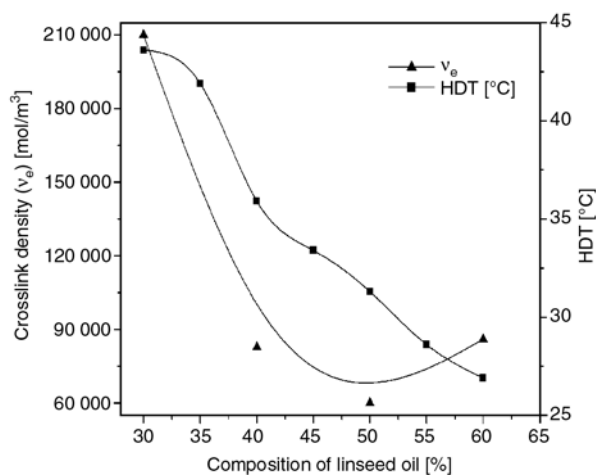


Figure 5. Heat deflection temperatures [°C] and crosslink density [v_e] with variation in the LIN content

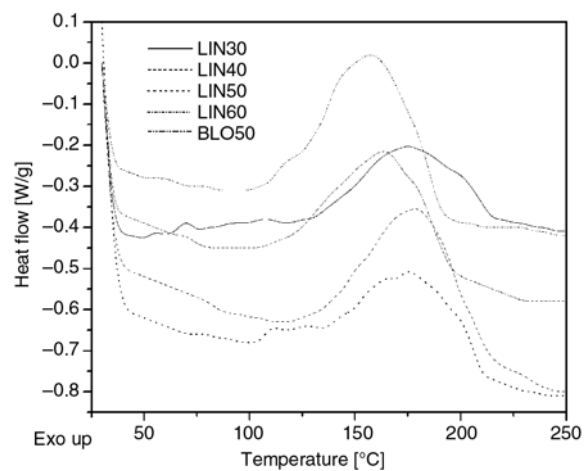


Figure 6. DSC plot using heat flow [W/g] versus temperature [°C] for LIN polymer samples (C₁, C₃, C₅, C₇, and B₅)

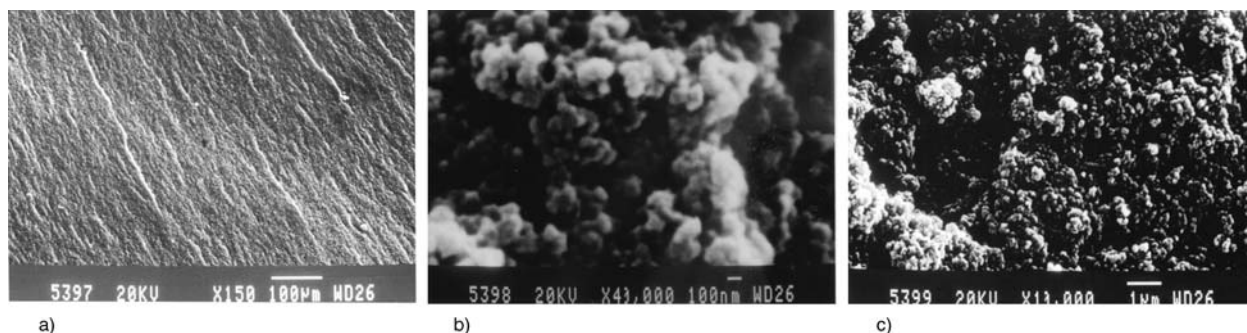


Figure 7. SEM micrographs of the insoluble materials from the sample C₅ (LIN50-ST30-DVB20) with different magnifications. (a) Magnification-150×, Scale-100 μm, (b) Magnification-40 000×, Scale-100 nm, (c) Magnification-10 000×, Scale-1 μm

shadowed by exothermic peaks in the range of 164–181°C, exhibited by the samples. The exothermic peaks are originated due to the possible crosslinking of the polymers initiated from the peroxy linkages formed during the free radical polymerization. In the free radical polymerization, some aerial oxidation occurs during polymerization, resulting in residual peroxy linkages [25].

The sample C₁ is hard in nature and it shows a broad peak. As the aromatic component (ST and DVB) decreased, the peak becomes sharper indicating the change in nature of the samples from plastic to waxy. The area of the peak increases with a decrease in peak width. With increase in the oil contents, the content of residual peroxy linkages increases [25]. The presence of more peroxy linkages needs higher energy for its breakage leading to crosslinking of polymers. Thus, the results from Table 2 justify the increase in the peak area. The increasing oil contents resulted in sharper peaks. The T_g of sample C₅ is higher than that for sample B₅, but the peak is observed to be less sharp for sample C₅ than sample B₅. This indicates that the sample B₅ is waxier.

4.6. Scanning electron microscopy (SEM) of the insoluble extracts

The insoluble portion of the samples after extraction with tetrahydrofuran has been used to study the morphological behavior by scanning electron microscopy. The SEM micrographs of all of the samples are very similar and indicate that the material is porous in nature and the pores are evenly distributed throughout the whole matrix. The micrographs of sample C₅ are shown as representative of all other samples. Three micrographs of the sample

C₅ with different magnification (contains 50% LIN) are shown in Figure 7. Figure 7a confirms the presence of cracks on the surface of the sample after Soxhlet extraction. Under higher magnifications (Figures 7b and 7c), the pores are clearly visible, which indicates that the material is porous in nature and, as the ST and DVB content decreases, the material becomes more porous.

4.7. Heat deflection temperature

The heat deflection temperatures (HDT) for various samples (C₁–C₇) are reported in Table 2. In Figure 5, the HDT of the polymeric sample is plotted against the percent of oil. The HDT of sample C₁ is the highest (43.6°C) and that for sample C₇ is the lowest (26.9°C). The higher value of HDT is mainly due to the higher aromatic content present in the polymeric samples. With a decrease in the aromatic content, the HDT of the samples decreases. The HDT for the sample with 65% oil is not tabulated, since the sample broke during testing due to its softness.

4.8. Swelling of samples

The polymeric samples have been tested for swelling in different media. The swelling ratios (q_v) have been determined from the swelling of samples by Equation (3). The swelling ratios of the samples prepared by the first method have been plotted against the percent of oil present in the sample. The graphs for the polymeric materials prepared by both methods are shown in Figure 8. The polymers prepared by the first method (C₁–C₈) show minimum swelling for saline water and a maximum for tetrahydrofuran. This is due to the fact that tetrahydrofuran is an organic solvent, which can readily

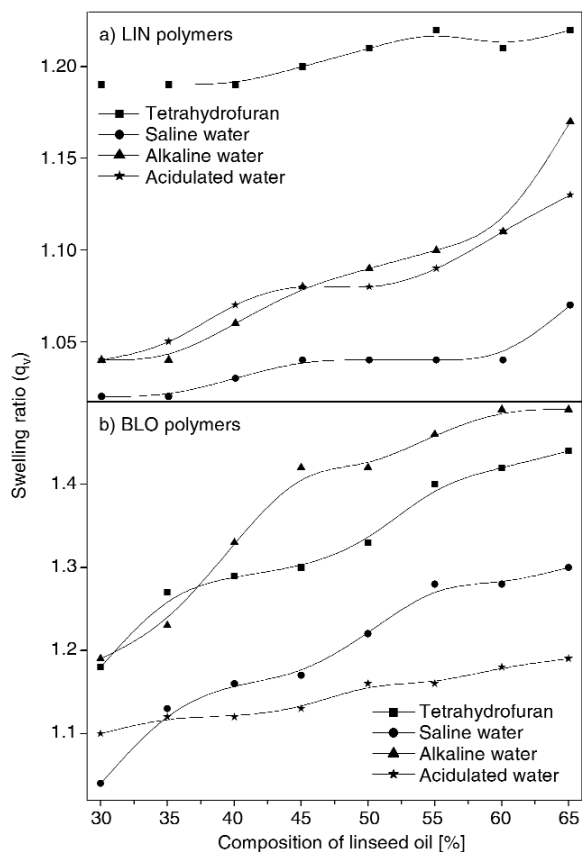


Figure 8. Swelling ratios in various media with variation in (a) the LIN content and (b) the BLO content

diffuse into the polymer network, whereas the other three solutions are aqueous and quite polar in nature and have less penetration into the relatively non-polar polymer and hence show less swelling. For the polymers prepared by the second method (B₁–B₈), the swelling is maximum for the alkaline solution and minimum for the acidic solution. Once again, tetrahydrofuran exhibits significant swelling, but even greater swelling is observed in the alkaline solution. This is perhaps due to the fact that initial treatment of the oil by air has resulted in partial oxidation of the oil, which in turn results in alkaline hydrolysis of the resulting polymeric materials, although we have no actual proof of this hypothesis. Due to the presence of oxidized fragments, presumably in the form of carboxylic acids, in the polymeric samples, minimum swelling is observed in acidic solution. When both methods for preparation of the polymers are compared, it is observed that the degree of swelling is greater for the material prepared by the second method. This can be explained by the fact that during polymerization at the higher temperatures, some degradation of the

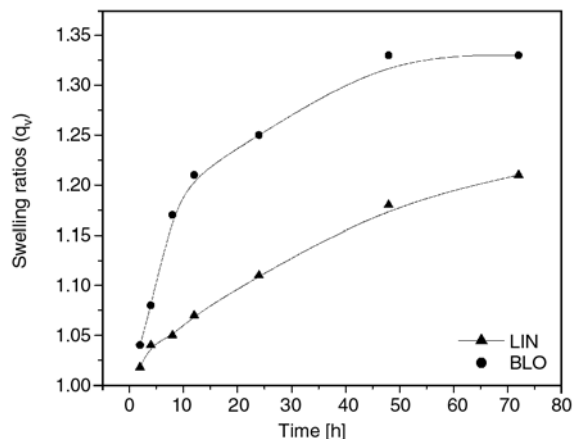


Figure 9. Change in the swelling ratios of 50% LIN (C₅) and BLO (B₅) samples with time

sample apparently occurs. The polymers prepared by the first method (C₁–C₈) are quite resistant towards saline water and those prepared by the second method (B₁–B₈) are resistant towards aqueous acid.

The swelling ratios at different time intervals for tetrahydrofuran for the samples C₅ and B₅ are shown in Figure 9. Figure 9 represents the time dependence of the swelling ratios. The swelling increases progressively with time. A sharp rise in q_v values is observed at the early stages of swelling. After 24 hours, the q_v values show little change. This may be explained in terms of the catastrophic rupture of the polymer network due to the internal stress caused by diffusion of the liquid into the polymer network. Sample B₅ shows more swelling than sample C₅.

5. Conclusions

A variety of novel polymers have been synthesized by the free radical graft copolymerization of linseed oil (LIN), ST and DVB in the presence of benzoyl peroxide as an initiator. The copolymerization is performed in a temperature range of 85–130°C. Various compositions of LIN, ST and DVB start to solidify at 100°C and the reaction is completed at 130°C. The resulting crosslinked polymers have been extracted by tetrahydrofuran in a Soxhlet extractor and are found to contain approximately 30 to 74% of highly crosslinked materials. ¹H NMR spectroscopic analysis indicates that the crosslinked materials are composed of soft oily, as well as hard aromatic domains. The insoluble cross-

linked materials have been examined under a scanning electron microscope (SEM). The SEM studies reveal the presence of fine pores in the material after extraction and indicate an even distribution of the soluble materials throughout the matrix. The heat deflection temperatures (HDT) of the polymer samples range from 26 to 44°C. With an increase in the oil content, the softness of the sample increases, leading to higher heat deflection at a lower temperature. The loss tangent and storage modulus have been used to calculate T_g and crosslink density of different samples. The T_g obtained from DMA for different linseed oil polymer samples ranges from 147 to 66°C. The crosslink density of samples ranges from 35.0 to 6.01·10⁴ mol/m³. The T_g from DSC results ranges from 182 to 158°C. These results show that the polymer samples prepared from linseed oil are hard and waxy in nature. The samples have been tested for swelling in alkaline, acidic, and brine solutions, as well as in tetrahydrofuran. The polymeric samples C₁–C₈ show minimum swelling in saline water and maximum swelling in tetrahydrofuran, while the polymeric samples B₁–B₈ show maximum swelling in alkaline solution and a minimum in acidic solution. The polymers prepared show high crosslink density and high transition temperature as show by hard plastics. The visual inspection showed that these samples are not hard plastics and have very little strength. The highly crosslinked materials with lower strength is resulted from the simultaneous oxidative degradation and crosslinking of polymer chains. These observations suggest that these polymers if prepared in anaerobic conditions may results in products with high molecular weight chains.

References

- [1] Conte L. S., Lercker G., Capella P., Catena M.: Linseed oil composition (in Italian). *Rivista Italiana delle Sostanze Grasse*, **56**, 339–342 (1979).
- [2] Berglund D. R.: Flax: New uses and demands in. in 'Trends in new crops and new uses.' (eds.: Janick J., Whipkey A.) ASHS Press, Alexandria, 358–360 (2002).
- [3] Knörr W., Daute P., Grützmacher R., Höfer R.: Development of new fields of application for linseed oil. *Fat Science Technology*, **97**, 165–169 (1995).
- [4] Budwig J.: Flax oil as a true aid against arthritis, heart infarction, cancer and other diseases. Apple Publication, Vancouver (1996).
- [5] Motawie A. M., Hassan F. A., Manieh A. A., Aboul-Fetouh M. E., El-Din A. F. J.: Some epoxidized polyurethane and polyester resins based on linseed oil. *Journal of Applied Polymer Science*, **55**, 1725–1732 (1995).
- [6] Thames S. F., Hariharan R., Wang Z., Brister E. H., King C. L., Panjanani K. G.: Internally plasticized and low VOC latex compositions and applications thereof. US Patent 6624223, USA (2003).
- [7] Tortorello A. J., Montgomery E., Chawla C. P.: Radiation-curable compositions comprising oligomers having an alkyd backbone. US Patent 6638616, USA (2003).
- [8] Gultekin M., Beker U., Güner F. S., Erciyas A. T., Yagci Y.: Styrenation of castor oil and linseed oil by macromer method. *Macromolecular Materials and Engineering*, **283**, 15–20 (2000).
- [9] Li F., Larock R. C.: Synthesis, structure and properties of new tung oil-styrene-divinylbenzene copolymers prepared by thermal polymerization. *Biomacromolecules*, **4**, 1018–1025 (2003).
- [10] Kundu P. P., Larock R. C.: Novel conjugated linseed oil-styrene-divinylbenzene copolymers prepared by thermal polymerization. 1. Effect of monomer concentration on the structure and properties. *Biomacromolecules*, **6**, 797–806 (2005).
- [11] Li F., Hanson M. V., Larock R. C.: Soybean oil-divinylbenzene thermosetting polymers: Synthesis, structure, properties and their relationships. *Polymer*, **42**, 1567–1579 (2001).
- [12] Li F., Larock R. C.: New soybean oil-styrene-divinylbenzene thermosetting copolymers. I. Synthesis and characterization. *Journal of Applied Polymer Science*, **80**, 658–670 (2001).
- [13] Li F., Larock R. C.: Thermosetting polymers from cationic copolymerization of tung oil: Synthesis and characterization. *Journal of Applied Polymer Science*, **78**, 1044–1056 (2000).
- [14] Li F., Haşjim J., Larock R. C.: Synthesis, structure and thermophysical and mechanical properties of new polymers prepared by the cationic copolymerization of corn, styrene and divinylbenzene. *Journal of Applied Polymer Science*, **90**, 1830–1838 (2003).
- [15] Hazer B., Demirel S. I., Borcakli M., Eroglu M. S., Cakmak M., Erman B.: Free radical crosslinking of unsaturated bacterial polyesters obtained from soybean oily acids. *Polymer Bulletin*, **46**, 389–394 (2001).
- [16] Wool R. P., Küseföglu S. H., Palmese G. R., Khot S. N., Zhao R.: High modulus polymers and composites from plant oils. US Patent 6121398, USA (2000).
- [17] Khot S. N., Lascala J. J., Can E., Morye S. S., Williams G. I., Palmese G. R., Küseföglu S. H., Wool R. P.: Development and application of triglyceride-based polymers and composites. *Journal of Applied Polymer Science*, **82**, 703–723 (2001).

- [18] Can E., Küseföglü S., Wool R. P.: Rigid thermosetting liquid molding resins from renewable resources. I. Copolymers of soyoil monoglycerides with maleic anhydride. *Journal of Applied Polymer Science*, **81**, 69–77 (2001).
- [19] Flory P. J.: Principles of polymer chemistry. Cornell University Press, Ithaca (1953).
- [20] Nielsen L. E., Landel R. F.: Mechanical properties of polymers and composites. Marcel Dekker, New York (1994).
- [21] Kumar R., Shakher C.: Application of digital speckle pattern interferometry and wavelet transform in measurement of transverse vibrations in square plate. *Optics and Lasers in Engineering*, **42**, 585–602 (2004).
- [22] Srinivasan P.: Mechanical vibration analysis. Tata McGraw Hill, New Delhi (1990).
- [23] Fieldson G. T., Barbari T. A.: The use of F.T.I.R.-A.T.R. spectroscopy to characterize penetrant diffusion in polymers. *Polymer*, **34**, 1146–1153 (1993).
- [24] Hamurcu E., Baysal B. M.: Interpenetrating polymer networks of poly (dimethylsiloxane). 1. Preparation and characterization. *Polymer*, **34**, 5163–5167 (1993).
- [25] Sharma V., Kundu P. P.: Addition polymers from natural oils: A review. *Progress in Polymer Science*, **31**, 983–1008 (2006).

Novel azo-peresters radical initiators used for the synthesis of acrylic pressure-sensitive adhesives

Z. Czech¹, A. Butwin¹, E. Herko¹, B. Hefczyc^{2,*}, J. Zawadiak²

¹Department of Chemical Organic Technology, Szczecin University of Technology, Pulaskiego 10, 70-322 Szczecin, Poland

²Department of Organic Chemical Technology and Petrochemistry, Silesian University of Technology, Krzywoustego 4, 44-100 Gliwice, Poland

Received 28 January 2008; accepted in revised form 29 February 2008

Abstract. Acrylic pressure-sensitive adhesives (PSA) based on two monomers: 2-ethylhexyl acrylate and acrylic acid were synthesized in organic solvent ethyl acetate using AIBN (2, 2'-azo-diisobutyronitrile) and new synthesized azo-peresters as radical initiators. After polymerization the viscosity, molecular weight and polydispersity of synthesized acrylic PSA were evaluated. The novel synthesized radical azo-perester initiators were synthesized, isolated and compared with industrial predominant usable azo-initiator AIBN.

Keywords: polymer synthesis, radical azo-perester initiators, viscosity, molecular weight, polydispersity

1. Introduction

The difference between pressure-sensitive adhesives and other adhesives, such as contact adhesives, is in the permanent surface stickiness of the pressure-sensitive adhesives before, or after, the application. In the giant field of adhesives the pressure-sensitive adhesives make up but a low percentage and the solvent-borne pressure-sensitive acrylic adhesives with their 20 000...30 000 tons per annum in Europe are almost a quantity negligible within this group. Pressure-sensitive adhesive acrylics can be applied in forms as a solvent-borne, as a water-borne (dispersions) and as a solvent-free system.

Solvent-based acrylic pressure-sensitive adhesives represent more than 45% of the total PSA produced. Pressure-sensitive adhesive acrylic solutions are nowadays predominantly manufactured by polymerization from a wide selection of monomers containing acrylic groups, often with low lev-

els of monomers having pendant functional groups in a refluxing organic solvent in the present of a radical initiator, such as organic peroxides or azo compounds. The acrylic monomers are commonly polymerized utilizing free radical polymerization processes involving the unsaturation contained in the acrylic monomer [1].

Azo groups containing initiators such as azo-peroxy compounds can be divided into: azo-dialkyl peroxides, azo-diacyl peroxides, azo-peresters and azo-hydroperoxides. First three groups of azo-peroxy compounds can play a role of bifunctional initiators in generation of block copolymers. They can also play a role of traditional initiator in radical polymerization of just one type of monomers.

Azo-diacyl peroxides and azo-peresters were tested as initiators in styrene [2–3] and acrylamide [4] polymerization processes and in preparation of block copolymers from vinyl [5–7] and acrylic [8] monomers.

*Corresponding author, e-mail: Barbara.Kordyaczny@polsl.pl
© BME-PT and GTE

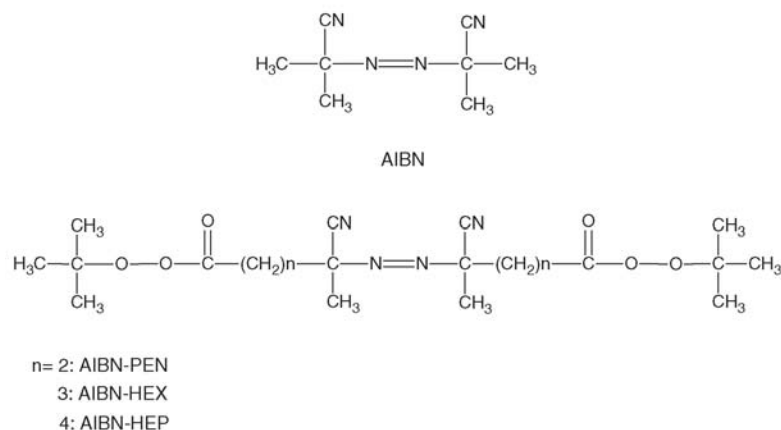


Figure 1. Chemical formula of AIBN and of azo-peresters

In 80's one of azo-peroxy compounds [6] was produced by Ludicol Division of Pennwalt Corporation. This compound was made from commercially available 4,4'-azobis-(4-cyanopentanoic) acid and *tert*-butyl hydroperoxide. Actually they are not commercially available. Due to the similarity of azo and peroxy groups decomposition temperatures those compounds were not suitable to obtain well-defined block copolymers when both stages of polymerization were initiated thermally. Azo-peroxy compounds in comparison to traditional free radical initiators have some other advantages, such as higher initiation rate [9].

Compounds described in this article belong to azo-peresters group. Those compounds have three labile groups: azo and two peroxy separated with carbon chain with different number of methylene groups (Figure 1). Figure 1 shows commercial radical initiator AIBN too.

2. Experimental

2.1. Synthesis of azo-peresters radical initiators

The simpler method to obtain azo-peresters is a method described in this article consisting of a single step reaction of carboxylic acid with azo function with *tert*-butyl hydroperoxide in presence of 1,1'-carbonylimidazole (Figure 2).

2.2. Preparation of azo-peroxyesters (general procedure)

To the 3-RB flask equipment with mechanic stirrer, nitrogen supply and dropping funnel, was intro-

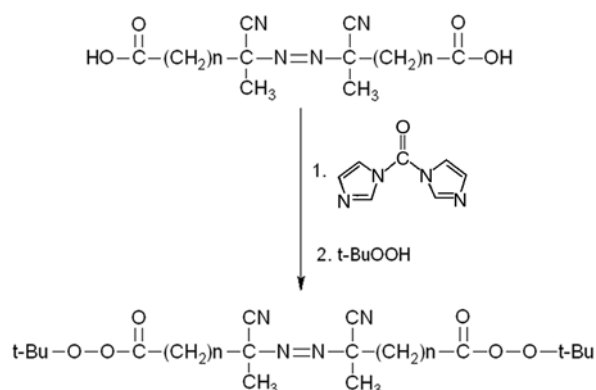


Figure 2. Synthesis of azo-peresters radical initiators

duced a solution of carboxylic acid with azo function (10 mmol) in dry THF. To this mixture was slowly added solution of 1,1'-carbonyldiimidazole (21 mmol) in dry THF. A suspension was extensively stirred for about 30 minutes. After this time the mixture was cooled down to less than 5°C, and 80% *tert*-butyl hydroperoxide (35 mmol) was added. The progress of the reaction was studied by means of TLC (thin layer chromatography) method (mobile phase CH₂Cl₂:CH₃COCH₃ 9:1, a solution of sodium iodide in acetic acid was used for visualization of the separated substances). The reaction was continued for 5 h. After this time to reaction mixture was added Et₂O, and stirring was continued for 45 minutes. The mixture was then washed twice: with 5% NaOH and water. The organic layer was dried with MgSO₄, and then the solvent was evaporated on vacuum rotary of ambient temperature. All azo-peresters were crystallized from CH₂Cl₂.

2.3. Materials for synthesis of azo-peroxyesters

Tert-butyl hydroperoxide (Merck) was extracted with hexane. THF was distilled over metallic Na and used immediately. 4,4'-azobis-(4-cyanopentanoic) acid (Fluka), 1,1'-carbonyldiimidazole (Alfa Aestar), 5,5'-azobis-(5-cyanoheptanoic) acid and 6,6'-azobis-(6-cyanoheptanoic) acid were synthesized as described by Silesian University of Technology.

2.4. Analysis of synthesis of azo-peroxyesters

¹H NMR spectra were recorded in CDCl₃ on a Varian Unity Inova-300 spectrometer using TMS as an internal standard and compared, with the reference standard. IR spectra were recorded on a Zeiss Specord M 80 spectrometer.

2.5. Synthesis of acrylic PSA using synthesized azo-peresters

The following experiments were conducted to study the influence of kind and concentration of novel azo-peroxyesters as radical initiators on the main properties of synthesized solvent-borne acrylic pressure-sensitive adhesives (PSA) as viscosity, molecular weight and polydispersity [10].

2.5.1. Materials

The acrylate monomers, i.e. 2-ethylhexyl acrylate, acrylic acid and solvent ethyl acetate were avail-

able from BASF (Germany). AIBN was supplied by Evonik Degussa (Germany) and other investigated radical azo-perester initiators (Figure 3) were synthesized at the Silesian University of Technology.

2.5.2. Polymerization process

All starting materials such as acrylate monomers, solvent and AIBN were obtained technical grade and were used without further purification unless otherwise noted. The investigated synthesized azo-peroxyesters were likewise technical commercial grade.

The basic solvent-borne pressure-sensitive adhesive was synthesized from between 90 and 99 wt% of 2-ethylhexyl acrylate and between 1 and 10 wt% of acrylic acid in ethyl acetate at the boiling point temperature about 77°C. AIBN and other azo-peroxyesters mentioned in Figure 3 were used as thermal initiators to start radical polymerization in the amount of 0.1 wt% according to monomers amount. The polymerization process was carried out for 8 h to reach 50 wt% of acrylic polymer content [11].

2.6. Method of testing

The viscosity of the evaluated solvent-borne acrylic pressure-sensitive adhesives containing the novel azo-peroxyesters initiators was determined with a Rheomat RM 189 from Rheometric Scientific, with spindle No 3 at 23°C.

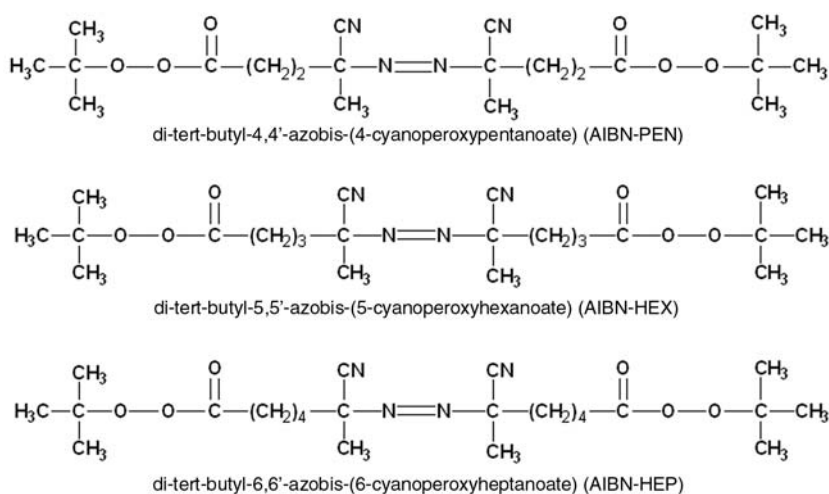


Figure 3. Investigated novel azo-peroxyesters

The molecular weight studies were performed in tetrahydrofuran with a liquid chromatograph LaChrom system: RI Detector L-7490 and LaChrom UV Detector L-7400 from Merck-Hitachi, equipped with a PLgel 10⁶ Å column from Hewlett-Packard.

3. Results and discussion

3.1. Synthesized azo-peroxyesters

Azo-peresters were obtained in single step reaction of carboxylic acid possessing azo function with *tert*-butyl hydroperoxide in presence of 1,1'-carbonyldiimidazole. Described method of synthesis is simpler than the double step method, due to the lack of individual preparation and separation of acylating agent (acid chloride). This method was used earlier in synthesis of esters and peresters [12]. Higher yields of desired compounds were achieved by using higher excess of hydroperoxide, than described in the literature [12].

In this method acylating agent is generated in situ by reaction of 1,1'-carbonyldiimidazole with carboxylic acid with azo function. This acylating agent is coupling immediately with hydroperoxide. Yields of obtained azo-perester are higher than obtained in the double step reaction, and purities are comparable (Table 1). All compounds were characterized by comparing their spectra with reference standards.

However one big disadvantage of described method is the sensitivity of 1,1'-carbonyldiimidazole and of the generated acylating agent to traces of water. Presence of water causes the decomposition of those compounds. Azo acid chlorides used in the two step method are also sensitive to water, but hydrolysis of this compound proceeds much slower. Azo acid chlorides are less sensitive to the presence of water than 1,1'-carbonyldiimidazole and acylating agent.

Table 1. Yield of the obtained compounds

Compound	Yield* [%]
di- <i>tert</i> -butyl-4,4'-azobis-(4-cyanoperoxy-pentanoate)	83
di- <i>tert</i> -butyl-5,5'-azobis-(5-cyanoperoxyhexanoate)	78
di- <i>tert</i> -butyl-6,6'-azobis-(6-cyanoperoxyheptanoate)	75

*the yield was calculated for pure compounds, determined according to the gravimetric method

3.2. Influence of the kind and concentration of the novel azo-peroxyesters and acrylic acid content on viscosity, molecular weight and polydispersity of synthesized acrylic PSA

The effect of acrylic acid concentration (from 1.0 to 10 wt%) on viscosity, molecular weight and polydispersity of synthesized solvent-borne acrylic pressure-sensitive adhesives is listed in Table 2 and presented in Figures 4–7.

Good examples of the correlations between viscosity, molecular weight and polydispersity of synthesized acrylic PSAs are shown in Table 2. The use of AIBN-HEP with the longest structure of organic radical gives excellent high viscosity and high molecular weight at lowest polydispersity. High viscosity and high molecular weight of acrylic PSAs mean the high content of the long acrylic polymer chains and a relatively small amount of short acrylic chains. This observed effect means the reduction of polydispersity, characterized by low polydispersity values. Acrylic PSAs with low polydispersity are characterized by high \overline{M}_w and \overline{M}_n values.

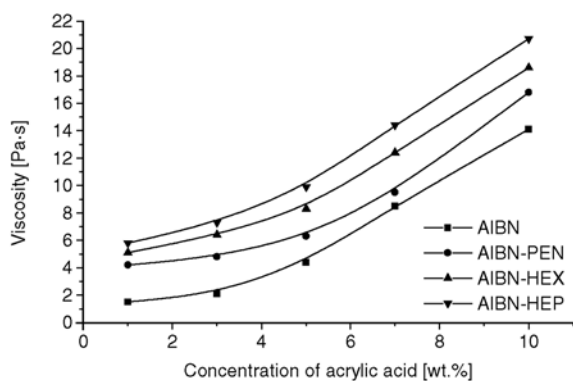
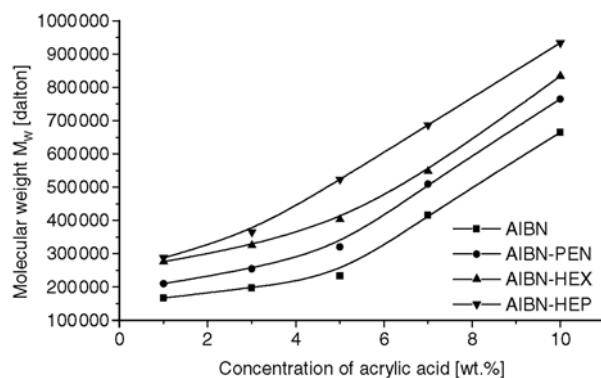
The viscosity of synthesised acrylic pressure-sensitive adhesives is very sensitive to the variations of the azo-peroxyester radical initiator kind and concentration of acrylic acid. In general, the viscosity of the acrylic PSA increases clearly with increasing the acrylic acid concentration. The highest viscosity of synthesized acrylic PSA was observed for azo-peroxyester AIBN-HEP with the longest structure of organic radical. The increasing of radical sluggishness influences positively the high molecular weight of synthesized acrylic PSA.

Figure 5 shows the influence of the acrylic acid concentration and kind of azo-peroxyesters and AIBN on weight average molecular weight M_w of the synthesized solvent-borne acrylic pressure-sensitive adhesives. As expected after evaluation of viscosity, the increase of acrylic acid concentration corresponds to the molecular weight M_w increase of synthesized acrylic PSA. By using of di-*tert*-butyl-6,6'-azobis-(6-cyanoperoxyheptanoate) (AIBN-HEP) the highest molecular weight M_w performance were observed.

The influence of the acrylic acid concentration and type of the investigated azo-peroxyesters used for polymerization on the number average molecular

Table 2. Viscosity, molecular weight and polydispersity of synthesized acrylic PSAs produced with AIBN and tested azo-peroxyester initiators

Concentration of acrylic acid [wt %]	Viscosity[Pa·s]	\bar{M}_w [dalton]	\bar{M}_n [dalton]	$P_d = \frac{\bar{M}_w}{\bar{M}_n}$
0.1 wt% of 2,2'-azo-bis-diisobutyronitrile (AIBN)				
1.0	1.5	167 000	41 300	4.04
3.0	2.1	198 000	49 700	3.98
5.0	4.4	234 000	64 100	3.65
7.0	8.5	416 000	125 000	3.33
10.0	14.1	665 000	213 000	3.12
0.1 wt% of di- <i>tert</i> -butyl-4,4'-azobis-(4-cyanoperoxy-pentanoate) (AIBN-PEN)				
1.0	4.2	210 000	57 500	3.65
3.0	4.8	255 000	73 500	3.47
5.0	6.3	321 000	98 800	3.25
7.0	9.5	509 000	163 000	3.12
10.0	16.8	765 000	254 000	3.01
0.1 wt% of di- <i>tert</i> -butyl-5,5'-azobis-(5-cyanoperoxyhexanoate) (AIBN-HEX)				
1.0	5.1	276 000	77 700	3.55
3.0	6.4	325 000	95 600	3.40
5.0	8.3	403 000	127 000	3.17
7.0	12.4	548 000	181 000	3.03
10.0	18.6	834 000	290 000	2.88
0.1 wt% of di- <i>tert</i> -butyl-6,6'-azobis-(6-cyanoperoxyheptanoate) (AIBN-HEP)				
1.0	5.8	288 000	86 000	3.35
3.0	7.3	365 000	113 000	3.23
5.0	9.9	523 000	170 000	3.08
7.0	14.4	687 000	239 000	2.87
10.0	20.7	934 000	347 000	2.69

**Figure 4.** Effect of acrylic acid concentration on viscosity of acrylic PSA synthesized by using of evaluated azo initiators**Figure 5.** Effect of acrylic acid concentration on molecular weight M_w of acrylic PSA synthesized by using of evaluated azo initiators

weight M_n of the synthesized solvent-borne acrylic pressure-sensitive adhesives is described in Figure 6. As can be seen from the M_n results recorded in Figure 6, the efficiency of the evaluated radical azo-peroxyester initiators of acrylic PSA molecular weight clearly corresponds to their chemical architecture, expressed as length of azo-peroxyester molecule. The longer the azo-peroxyester molecule, the greater the acrylic PSA molecular weight (AIBN-HEP). With the increase of acrylic acid

amount the molecular weight M_n of synthesized acrylic PSA also rises.

Higher molecular weight adhesives allow the manufacture of cohesive layers and lower molecular weight adhesives the manufacturing of adhesive and tacky layers. Acrylic PSA polydispersity as molecular weight distribution includes information about acrylic soft and hard performance.

Figure 7 shows polydispersity of the synthesized acrylic PSA as a function of different concentration

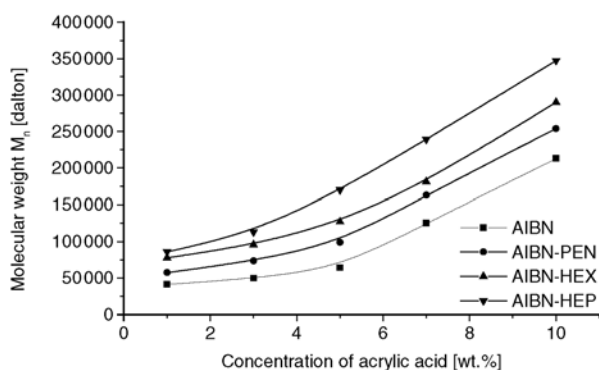


Figure 6. Effect of acrylic acid concentration on molecular weight M_n of acrylic PSA synthesized by using of evaluated azo initiators

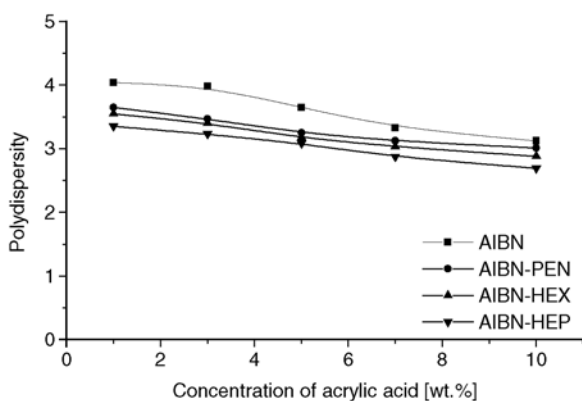


Figure 7. Effect of acrylic acid concentration on the polydispersity of acrylic PSA synthesized by using of evaluated azo initiators

of acrylic acid and kind of novel azo-peroxyesters initiators and AIBN. The following polydispersity ranking for various concentrations of acrylic acid and type of investigated azo initiators was obtained: 2,2'-azo-bis-diisobutyronitrile (AIBN), di-*tert*-butyl-4,4'-azobis-(4-cyanoperoxy-pentanoate) (AIBN-PEN), di-*tert*-butyl-5,5'-azobis-(5-cyanoperoxyhexanoate) (AIBN-HEX) and di-*tert*-butyl-6,6'-azobis-(6-cyanoperoxy-heptanoate) (AIBN-HEP). For all synthesized acrylic PSA containing different contents of acrylic acid the using of AIBN allows synthesis of solvent-borne acrylic PSA with high tack and adhesion properties and the using of novel azo-peroxyesters initiators allows manufacturing of acrylic PSA characterized by high cohesion level.

4. Conclusions

The evaluation of novel synthesized azo-peroxyesters initiators has recently attracted considerable

attention, due to their practical and potential application in various industrial branches to comprehensive permanent self-adhesive technical and medical articles with the wide range of very interesting original performance. Solvent-borne acrylic pressure-sensitive adhesives with high performance can be formed by the radical polymerization of typical acrylate monomers such as 2-ethylhexyl acrylate and acrylic acid using instead of AIBN the novel azo-peroxyester initiators. Especially the di-*tert*-butyl-6,6'-azobis-(6-cyanoperoxy-heptanoate) (AIBN-HEP) guarantees satisfactorily performance with respect to the important properties of solvent-borne acrylic PSA containing various amounts of acrylic acid between 3 and 7 wt%.

References

- [1] Czech Z.: Stable vinyl-oxy-carbonyl-oxy and -amino compounds with chromophore group. German patent, DE19501025, Germany (1996).
- [2] Simionescu C., Sik K. G., Comanița E., Dumitriu S.: Bifunctional initiators, VI. Polymerization of styrene with 4,4'-azo-bis-(4-cyanovaleryl)-bis-(*m*-chlorobenzoyl)-diperoxide as initiator. *Die Angewandte Makromolekulare Chemie*, **126**, 73–80 (1984).
- [3] Simionescu C. I., Popa A. A., Comanița E., Comanița B.: Polymerization of styrene initiated with cumyl 4-*t*-butylazo-4-cyanoperoxy-pentanoate. *Polymer-Plastics Technology and Engineering*, **31**, 451–461 (1992).
- [4] Sik K.G., Dumitriu S., Comanița E., Simionescu C.: Bifunctional initiators: 7. Acrylamide polymerization with 4,4'-azo-bis-(4-Cyanovaleryl)-bis-(*m*-Chlorobenzoyl) diperoxide as initiator. *Polymer Bulletin*, **12**, 419–425 (1984).
- [5] Vogla C., Hazer B., Torul O.: Kinetic study of vinyl polymerization with a new oligo azo peroxidic initiator. *European Polymer Journal*, **33**, 907–912 (1997).
- [6] Piirma I., Chou L-P.: Block copolymers obtained by free-radical mechanism, I. Methyl methacrylate and styrene. *Journal of Applied Polymer Science*, **24**, 2051–2070 (1979).
- [7] Hazer B., Ayas A., Besirli N., Saltek N., Baysal B. M.: Preparation of ABCBA-type block copolymers by use of macro-initiators containing peroxy and azo groups. *Die Makromolekulare Chemie*, **190**, 1987–1996 (1989).
- [8] Gunesin B. Z., Piirma I.: Block copolymers obtained by free radical mechanism, II. Butyl acrylate and methyl methacrylate. *Journal of Applied Polymer Science*, **26**, 3103–3115 (1981).
- [9] Simionescu Cr., Comanița E., Păstrăvanu M., Dumitriu S.: Progress in the field of bi- and poly-functional free-radical polymerization initiators. *Progress in Polymer Science*, **12**, 1–109 (1986).

- [10] Czech Z.: Synthesis and cross-linking of acrylic PSA systems. *Journal of Adhesion Science and Technology*, **7**, 625–635 (2007).
- [11] Czech Z., Wesolowska M.: Development of solvent-free acrylic pressure-sensitive adhesives. *European Polymer Journal*, **43**, 3604–3612 (2007).
- [12] Staab H.A., Rohr W., Graf F.: Darstellung von Diacylperoxyden und Persäureestern nach der Imidazolidmethode. *Chemische Berichte*, **98**, 1122–1127 (1965).

Modification of PTFE nanopowder by controlled electron beam irradiation: A useful approach for the development of PTFE coupled EPDM compounds

M. S. Khan*, D. Lehmann, G. Heinrich

Leibniz Institute of Polymer Research Dresden, Hohe Str. 6, D-01069 Dresden, Germany

Received 30 January 2008; accepted in revised form 9 March 2008

Abstract. Low-temperature reactive mixing of controlled electron beam modified Polytetrafluoroethylene (PTFE) nanopowder with Ethylene-Propylene-Diene-Monomer (EPDM) rubber produced PTFE coupled EPDM rubber compounds with desired physical properties. The radiation-induced chemical alterations in PTFE nanopowder, determined by electron spin resonance (ESR) and Fourier transform infrared (FTIR) spectroscopy, showed increasing concentration of radicals and carboxylic groups (–COOH) with increasing irradiation dose. The morphological variations of the PTFE nanopowder including its decreasing mean agglomerate size with the absorbed dose was investigated by particle size and scanning electron microscopy (SEM) analysis. With increasing absorbed dose the wettability of the modified PTFE nanopowder determined by contact angle method increased in accordance with the (–COOH) concentration. Transmission electron microscopy (TEM) showed that modified PTFE nanopowder is obviously enwrapped by EPDM. This leads to a characteristic compatible interphase around the modified PTFE. Crystallization studies by differential scanning calorimetry (DSC) also revealed the existence of a compatible interphase in the modified PTFE coupled EPDM.

Keywords: *mechanical properties, PTFE nanopowder, EPDM, electron beam irradiation, compatibility*

1. Introduction

Polytetrafluoroethylene (PTFE) finds an exceptional position in plastic industry due to its outstanding chemical and heat resistance, electrical insulation and its significantly low friction coefficient. These properties recommend PTFE for numerous and diverse applications [1]. Both elastomeric and thermoplastic fluoropolymers find a wide use especially in automotive applications such as seals, O-rings and gasket etc. [2]. It is also blended with other polymers or reinforced as a composite material for special purpose applications [3–5]. However, its inherently low adhesion and inert behaviour limit its dispersion and compatibility with other materials. Therefore, surface modification of PTFE to enhance its wettability and

compatibility is a prerequisite for its effective utilization in other compounds. New approaches were considered to surface modification of PTFE via different procedures [6–10]. Significant developments were also made both in the synthesis and manufacturing of new commercial fluoropolymers with improved mechanical properties [11–12]. However, electron beam modification provides a simple and effective method for modification of PTFE powder [13–20]. Recently, newly developed chemically coupled PTFE-PA compounds have opened a new way in producing high performance wear-resistant materials [21–23]. A new class of potential wear-resistant materials based on modified PTFE powder filled SBS, NBR and EPDM compounds were also produced [24]. Modified PTFE

*Corresponding author, e-mail: khan@ipfdd.de
© BME-PT and GTE

powder was specially utilized in NBR to expand its utility as wear-resistant material for sealing applications [25]. PTFE micropowders produced by emulsion polymerization are low-molecular weight fine coagulated powder commonly used as an additive in variety of applications [26–27]. In the previous study, PTFE coupled EPDM compounds were produced by reactive mixing of pre-modified PTFE nanopowder with EPDM [28]. In the present work the influence of dose-controlled agglomerate size, structural morphology and interfacial compatibility of PTFE nanopowder on the physical properties of the resulting modified PTFE-EPDM blends are presented. These investigations are of extreme importance especially in the development of new rubber compounds which require optimization of both the physical and tribological properties [29–30]. It has been shown that the desired physical properties can be achieved simply by controlled modification of PTFE nanopowder.

2. Materials and experimental

2.1. Materials

Both EPDM (Buna EP G 6850) with ethylidene norbornene (ENB) content 7.7 wt%; ethylene content 51 wt%; Mooney viscosity, ML (1+4) at 125°C, 60; ash content 0.2 wt%; specific gravity, 0.86; and peroxide (Perkadox 14-40 MB GR) were supplied from Lanxess Deutschland GmbH, Germany while coagent (R-20S/Saret 634C) was used from Sartomer, USA. Algoflon L100X an emulsion grade received from Solvay Solexis S.p.A, Italy is an agglomerated white PTFE nanopowder with the bulk density and surface area of 0.25–0.44 g·cm⁻³ and 26 g·m⁻², respectively.

2.2. Modification of PTFE nanopowder

PTFE nanopowder was modified with absorbed doses of 20, 100, 200, 300, 400 and 500 kGy with the help of ELV-2 electron beam accelerator from Budker Institute of Nuclear Physics, Novosibirsk, Russia, installed at the Leibniz Institute of Polymer Research Dresden. The electron beam treatment was carried out in air and at room temperature with an absorbed dose of 2.5 kGy per pass and at an average dose rate of about 10 kGy/h. These treatment parameters were considered in order to avoid excess temperature rise which might favour deactivation of

the radical formation as well as to control agglomerate size and chemical structure via absorbed dose. Further information about the electron accelerator (ELV-2) facility can be found in [18].

2.3. PTFE nanopowder characterization

The number of free radicals was determined with the help of MiniScope MS200 electron spin resonance (ESR) instrument from Magnettech Limited, Germany. Spin numbers for each absorbed dose were calculated after four hours of electron treatment. Fourier Transform Infrared Spectrometer (FTIR) spectra were recorded on Vertex 80v (Bruker) FTIR spectrometer (4000–400 cm⁻¹, resolution = 2 cm⁻¹, 32 scans per measurement) in transmission mode on 10 μm thin PTFE foils to observe the chemical changes induced in PTFE nanopowder having exposed to different absorbed doses. The contact angle measurements were performed on (1 mm thin, diameter 20 mm) PTFE discs with the help of OCA 40 Micro contact angle meter from DataPhysics Instrument GmbH, Germany. The rounded discs were prepared by compressing PTFE nanopowder at room temperature under a pressure of 1 MPa. Sessile drop method was performed to determine the wettability of PTFE discs modified similarly as discussed in section 2.2. The discs were used to obtain smooth and comparable surfaces for contact angle measurement.

The particles size and their distribution were determined with the help of the particle size analyzer, Sympatec HELOS HO367 from Sympatec GmbH Germany, having a measuring range of 0.5/0.9–175 μm. The primary and mean agglomerate size of PTFE nanopowder was 70–80 nm and 17.7 μm, respectively, as received from the supplier. Post and pre-irradiation structure morphology of the PTFE nanopowder modified to different absorbed doses were determined with the help of LEO 435 scanning electron microscope (SEM – acceleration voltage 20 kV) from LEO Electron Microscopy Ltd, England. SEM examination was also performed on the cryogenic surface fractured samples for the dispersion analysis of PTFE nanopowder in EPDM.

2.4. Specimen preparation

EPDM and 30 phr (parts per hundred of rubber) PTFE nanopowder were first pre-mixed in a Poly-

Lab Haake Rheomix internal mixer from Thermo Electron Corp, Germany for 5 minutes at 100°C and at a rotor speed of 50 rpm. Curatives including 7.5 phr coagent and 5 phr peroxide were added to the material on a two roll laboratory mill (Polymix 110L, Servitic, Germany) at room temperature. A constant friction ratio of 1.2 was maintained between the milling rolls. Approximately 2 mm thick sheets were drawn out from the mill and cured in a hot press (Fontune, Holland) under a pressure of 5 MPa at a temperature of 170°C up to their corresponding optimum cure time.

2.5. PTFE-EPDM blend characterization

Mechanical properties including tensile strength at break, percentage elongation at break and modulus at 300% elongation were carried out according to ISO 527 at a cross-head speed of 200 mm/min using tensile testing machine (Zwick, Germany). Hardness values were measured according to DIN 53505, using a Shore A Durometer. Indentations were made at several points for each specimen for the determination of the average hardness value. Differential scanning calorimetry (DSC) studies of the PTFE-EPDM composites were carried out using NETSCH DSC 204 from NETZSCH-Gerätebau GmbH, Germany to analyze the influence of absorbed dose on the compatibility and dispersion in EPDM from their crystallization studies. All experiments were performed under atmospheric conditions and at a heating rate of 10 K·min⁻¹ above the melting temperature of PTFE up to 330°C. The results obtained were expressed as input energy versus temperature. Transmission electron microscopy (TEM) micrographs of the modified and non-modified PTFE filled EPDM were recorded on transmission microscope model EM910 from Carl Zeiss, Germany.

3. Results and discussion

3.1. Effect of modification on the molecular structure of PTFE

Figure 1 shows the ESR spectra of the modified and non-modified PTFE nanopowder. The ESR spectra show a systematic increase in the signal with increasing absorbed irradiation dose. Non-modified PTFE nanopowder produced no signal due to the absence of reactive free radicals. The

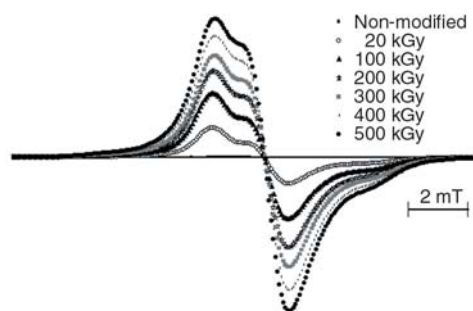


Figure 1. Electron spin resonance (ESR) spectra of PTFE nanopowder modified with different absorbed doses

increase in signal indicates that the radical concentration is increased with increasing absorbed dose or modification. 500 kGy irradiated PTFE nanopowder having the highest spin numbers shows the highest number of radical concentration. Electron beam treatment generates persistent reactive free radicals and functional groups on the surface due to degradation of PTFE nanopowder by chain scission. Figure 2 visualizes the radiation induced degradation of PTFE in the presence of air. It has been reported that PTFE undergoes C–F and C–C scission during energy rich electron modification process [31–32]. C–F scission results in secondary radicals while C–C scissions produce primary free radicals. These free radicals react with atmospheric oxygen to yield stable perfluoroalkylperoxy radicals. Besides these peroxy radicals, carbonyl fluoride groups are also formed which hydrolyse in the presence of atmospheric moisture to form carboxylic acid groups (–COOH). The complete reaction mechanism can be found in [33]. Chemical changes introduced in PTFE after exposure to electron treatment were monitored by FTIR spectroscopy. Figure 3 shows several new bands in the infrared spectrum of modified PTFE. The peak at 1884 cm⁻¹ was identified with carbonyl fluoride groups (–COF) while 1810 cm⁻¹ are free and 1777 cm⁻¹ associated carboxylic acid groups (–COOH).

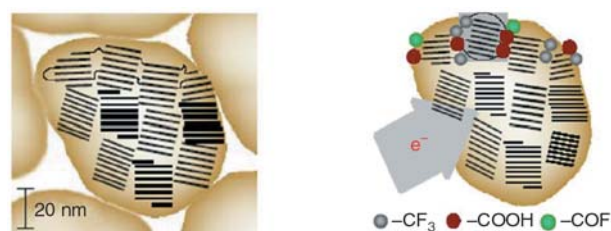


Figure 2. Radiation induced degradation of high molecular weight PTFE nanopowder

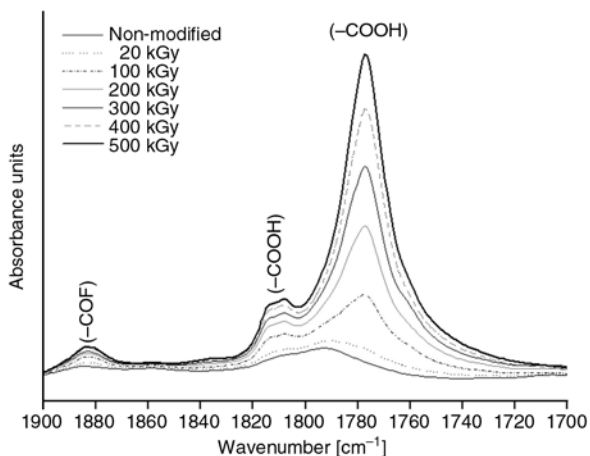


Figure 3. Infrared spectra (1900–1700 cm^{-1}) of L100X (nanopowder) after modification by different absorbed doses in comparison to non-modified PTFE

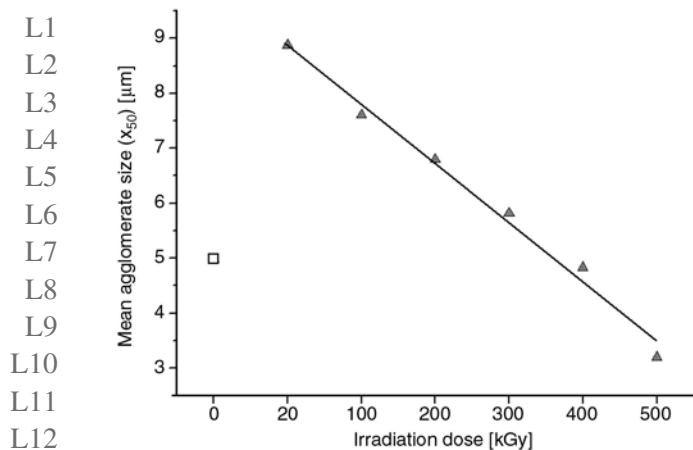


Figure 4. Mean agglomerate size of PTFE nanopowder as a function of absorbed dose (Empty box indicates non-irradiated while filled triangles indicates irradiated PTFE nanopowders)

Figure 4 shows the influence of absorbed dose on the mean agglomerate size of PTFE nanopowder. It can be seen that mean agglomerate size of PTFE nanopowder decreased systematically with absorbed irradiation dose. It suggests that mean agglomerate size of PTFE nanopowder can be controlled via absorbed dose. The decrease in agglomerate size is due to chain scission of PTFE nanopowder. High molecular weight PTFE is reduced to low molecular weight PTFE. The highest absorbed dose of 500 kGy shows the smallest mean agglomerate size. The mean agglomerate size delivered by the supplier of virgin non-modified PTFE nanopowder was 17.7 μm compared to our determined agglomerate size of 5.0 μm . This might be due to the ability of PTFE nanopowder to re-agglomerate as can

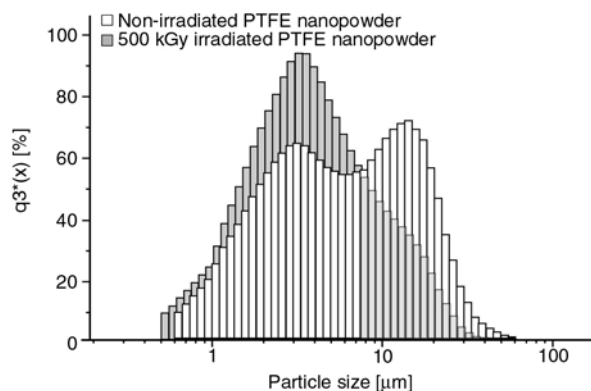


Figure 5. Particle size distribution of non-irradiated and 500 kGy irradiated PTFE nanopowder

be seen in the particle size distribution in Figure 5. The particle size distribution suggests that non-irradiated L100X PTFE nanopowder has a broad particle size distribution compared to 500 kGy irradiated PTFE nanopowder. The non-irradiated PTFE nanopowder shows a characteristic bimodal distribution compared to unimodal distribution of 500 kGy irradiated PTFE nanopowder. This specific bimodal distribution clearly signifies that non-irradiated L100X PTFE nanopowder is mainly composed of bigger agglomerates which tend to re-agglomerate. On the contrary, 500 kGy irradiated PTFE nanopowder indicates finely dispersed smaller agglomerate particles. This can also be seen in the SEM micrographs of 500 kGy irradiated PTFE nanopowder. Effect of absorbed dose on the agglomerate morphology of (a) non-irradiated L100X and (b) 500 kGy irradiated PTFE nanopowder is shown in Figure 6. It is evident that the agglomerate size and morphology of these nanopowders are apparently distinguishable from each other. Non-irradiated PTFE nanopowder are huge solid-structured agglomerates formed by the random re-agglomeration of PTFE agglomerates. In comparison, 500 kGy irradiated PTFE nanopowder shows fine homogeneous coarse particles dispersed individually over the area without the formation of huge agglomerates.

Figure 7 shows result of the contact angle measurements on PTFE nanopowders having different absorbed doses in comparison to 0 kGy (non-modified) L100X PTFE nanopowder. The horizontal line indicates contact angle value of a typical commercial PTFE. It is observed that the water contact angles of modified PTFE discs are lower than non-modified PTFE disc and is systematically decreas-

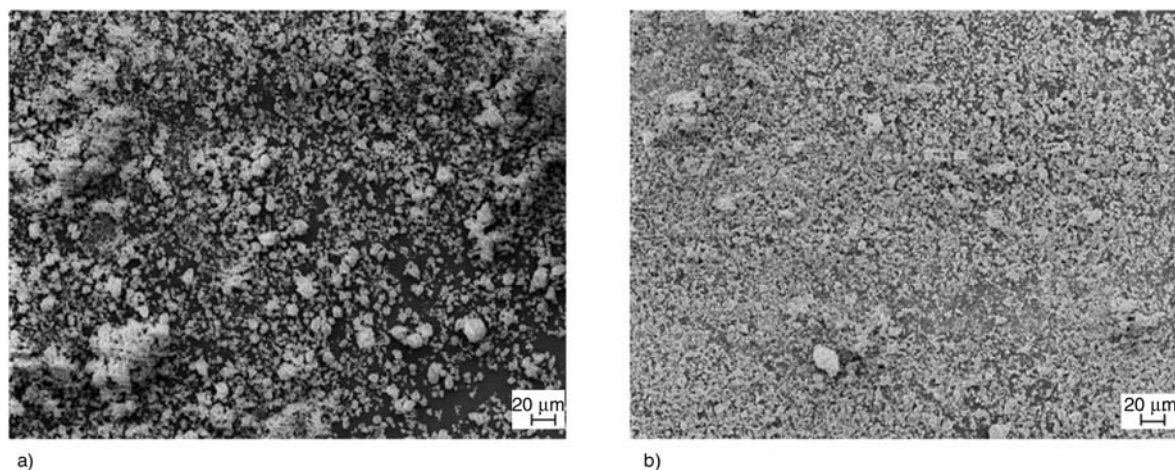


Figure 6. Scanning electron micrographs of (a) non-irradiated and (b) 500 kGy irradiated PTFE nanopowder

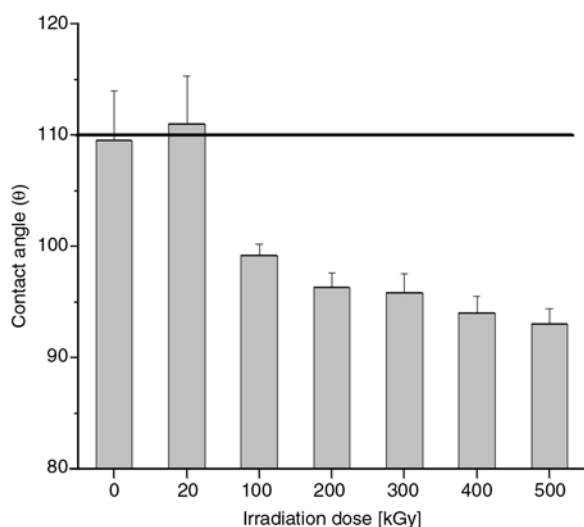


Figure 7. Effect of the absorbed dose on the contact angle of modified PTFE discs in comparison to non-modified PTFE. The horizontal line indicates contact angle value of a commercial PTFE

ing with increasing absorbed dose. The water contact angle of 111° of non-modified L100X PTFE nanopowder indicates its inherently hydrophobic behavior. Post-modification to different absorbed doses result in the decrease in contact angle from 114.8 to 92° for 500 kGy PTFE nanopowder. That is, compared with non-modified PTFE, the wettability of 500 kGy is significantly increased. The increase in wettability is due to the strong interaction between water and the hydrophilic groups (COF/COOH) generated on the surface of PTFE nanopowder after electron treatment in the presence of air. As can be seen, increasing absorbed dose results in lower contact angles due to the generation of oxygen containing groups on the PTFE surface. Lower contact angles correspond to higher

surface energy and thus higher adhesion and higher interfacial compatibility. As shown in Figure 3 an increasing absorbed dose results in higher concentration of C=O groups (1777 cm^{-1}). This shows that the chemical structure of PTFE nanopowder was changed due to electron treatment.

3.2. Effect of structural changes on the compatibility with EPDM

Figure 8a–8c show TEM micrographs of PTFE⁰ kGy-EPDM, PTFE³⁰⁰ kGy-EPDM and PTFE⁵⁰⁰ kGy-EPDM blends. The enhanced interfacial compatibility in case of PTFE³⁰⁰ kGy-EPDM and PTFE⁵⁰⁰ kGy-EPDM can be seen in Figures 8b and 8c. The modified agglomerate particles are embedded and wrapped by EPDM. No clear and visible interphase can be seen between the two incompatible polymers. Slightly light and dark regions around modified PTFE powder are an indication of a reinforced compatible interphase due to radical coupling with EPDM. It is also observed that modified PTFE agglomerate acts as a PTFE core surrounded by EPDM shell. On the other hand, PTFE⁰ kGy-EPDM shows non-modified PTFE nanopowder as solid embedded bodies lacking interfacial compatibility with EPDM. The interface is distinctively separated from each other. No mutual compatible interphase exists as observed in both PTFE³⁰⁰ kGy-EPDM and PTFE⁵⁰⁰ kGy-EPDM blends. Modified agglomerates in case of PTFE⁵⁰⁰ kGy-EPDM are elongated and outstretched in a specific direction. The modified PTFE particles due to enhanced compatibility and dispersion are oriented under high-shearing during reactive blending. However, non-modified PTFE

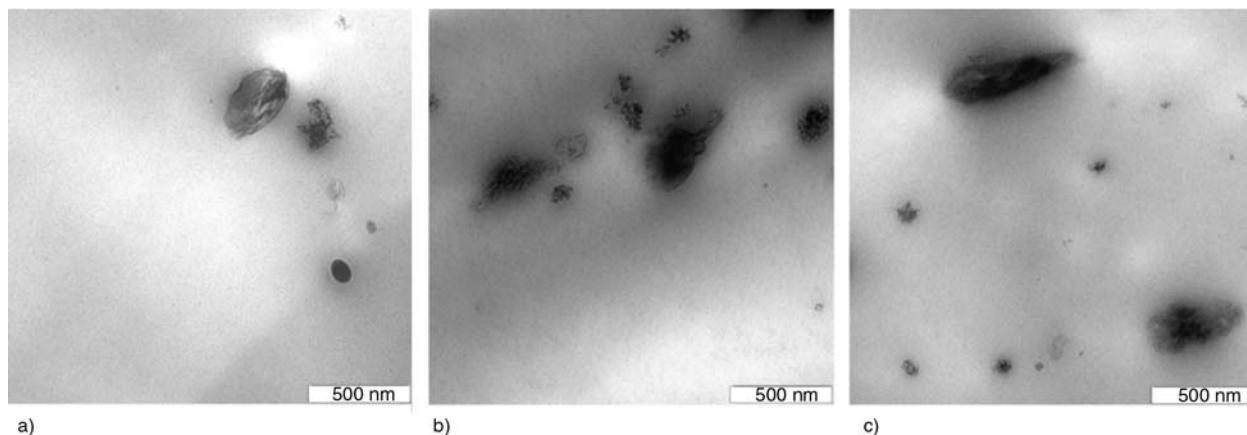


Figure 8. TEM morphologies of a) PTFE^{0 kGy}-EPDM; b) PTFE^{300 kGy}-EPDM and c) PTFE^{500 kGy}-EPDM blends

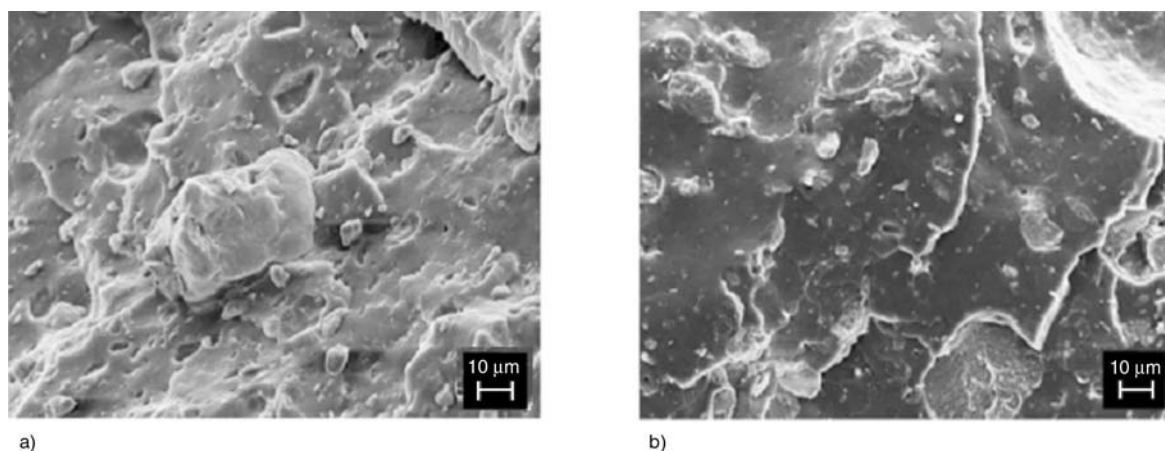


Figure 9. SEM micrographs of the tensile fractured surfaces of a) PTFE^{0 kGy}-EPDM and b) PTFE^{500 kGy}-EPDM blends

nanopowder being inert remained as huge rounded agglomerates even under high shearing. This behavior can also be seen in microdispersion in EPDM matrix. Figures 9a and 9b shows SEM micrographs of the tensile fractured surfaces of PTFE^{0 kGy}-EPDM and PTFE^{500 kGy}-EPDM. It is evident that the surface features are apparently distinguishable from each other. The PTFE^{500 kGy}-EPDM vulcanizate surface is smooth, with agglomerates embedded and homogeneously dispersed in the EPDM matrix while PTFE^{0 kGy}-EPDM shows an uneven, inhomogeneous surface with large vacuoles on the fractured surface. This indicates that the PTFE particles are being pulled out of the matrix on application of stress due to the absence of interfacial interaction or coupling with the matrix. It can be observed that the non-modified PTFE particles are bigger in size and tend to form huge irregular agglomerates in the EPDM matrix even under high shearing during blending operation. Non-modified L100X PTFE particles lack both the compatibility and the dispersion efficiency. Figure 10 shows the

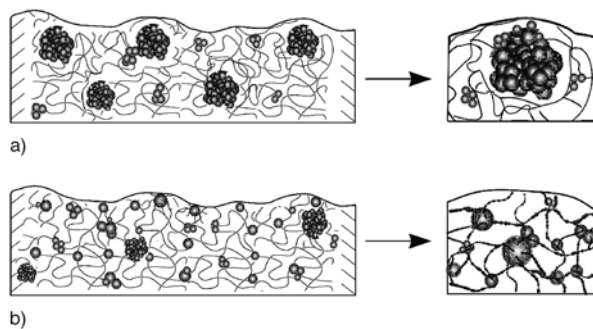


Figure 10. Schematics of the (a) non-modified and (b) modified PTFE nanopowder in EPDM

schematics of the (a) non-modified and (b) modified PTFE nanopowder in EPDM.

3.3. DSC investigations

Figure 11 shows the thermal traces of (a) non-modified and 500 kGy irradiated PTFE nanopowder and (b) corresponding blends PTFE^{0 kGy}-EPDM and PTFE^{500 kGy}-EPDM. The crystallization peak of 500 kGy irradiated PTFE nanopowder shifts to a lower temperature of about 303.5°C. Also, the crys-

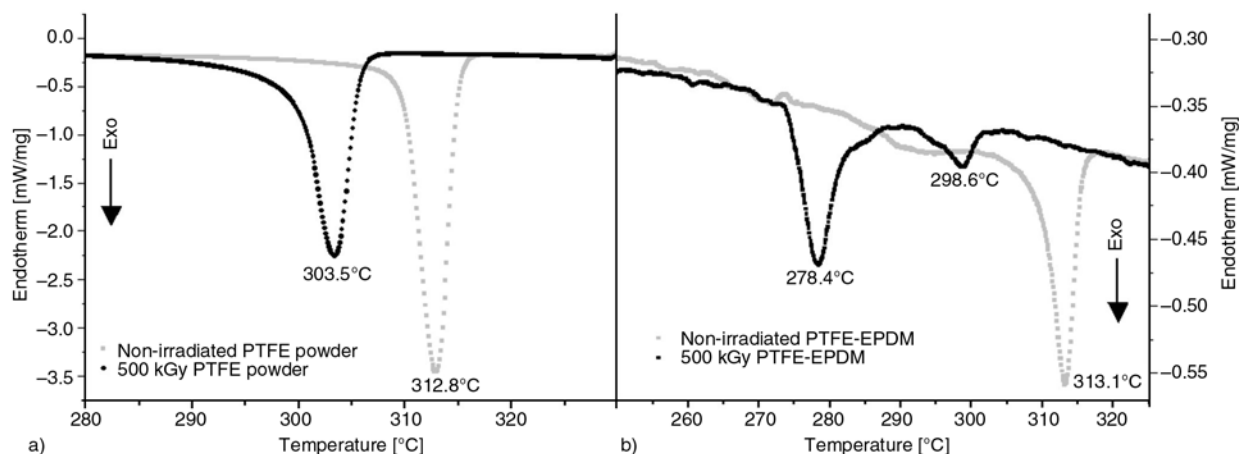


Figure 11. DSC cooling scans of the non-irradiated and 500 kGy irradiated PTFE nanopowder (a), and their corresponding EPDM blends (b)

tallization onset occurred at lower temperature and continued down to approx. 290°C. These distinct variations in 500 kGy compared to non-modified PTFE nanopowder is due to the electron beam treatment process which caused degradation of 500 kGy PTFE nanopowder. The molecular weight decreases due to chain scission and leads to PTFE macromolecules of different chain lengths. As a result, the crystallization peak occurs at lower temperatures and the crystallization process continues till much lower temperatures in comparison to the non-modified PTFE nanopowder.

In case of blends, PTFE^{500 kGy}-EPDM shows two crystallization peaks located at distinct temperatures. The second crystallization step at lower temperature also called fractionated crystallization occurred at 278°C along with the bulk crystallization peak at 298°C [34–35]. The area of the first bulk crystallization peak is smaller as compared to the area of the second peak. However, the crystallization temperature (298.6°C) of the first peak is close to 500 kGy irradiated PTFE nanopowder (303.5°C). The first crystallization peak is attributed to the content of PTFE nanopowder in EPDM having comparatively bigger and incompatible agglomerates. The PTFE agglomerates could be compatibilized only on the surface and the core consists of pure agglomerated PTFE nanopowder. These agglomerates show crystallization temperatures similar to pure PTFE bulk crystallization. However, for PTFE^{0 kGy}-EPDM, no fractionated crystallization except bulk crystallization similar to non-irradiated PTFE powder is observed at 313°C. This stems from the fact that non-irradiated PTFE

nanopowder is difficult to de-agglomerate and disperse homogeneously. The variations in the position of the transition-melting peaks observed in PTFE^{500 kGy}-EPDM is due to the specific chemical compatibility of the electron beam modified PTFE with EPDM. This unique fractionated crystallization behaviour is mainly due to the fine dispersion of 500 kGy irradiated PTFE nanopowder in EPDM. The outstanding dispersion of 500 kGy irradiated PTFE nanopowder is also attributed to its smaller particle size and enhanced compatibility as is evident in Figure 8. PTFE^{0 kGy}-EPDM on the other hand has significantly poor dispersion and compatibility with EPDM.

3.4. Physical properties

Figures 12a and 12b show tensile strength and elongation at break of PTFE-EPDM blends as a function of absorbed irradiation dose. The horizontal line represents EPDM gum. In case of PTFE^{0 kGy}-EPDM, tensile strength and elongation at break are lower than modified PTFE filled EPDM. With increasing absorbed dose, tensile strength and elongation at break of modified PTFE coupled EPDM compounds increase systematically. Tensile strength and elongation at break of EPDM gum and PTFE^{0 kGy}-EPDM are almost the same because of poor compatibility and dispersion. On the other hand, PTFE^{500 kGy}-EPDM shows the highest tensile strength and elongation at break. Modified PTFE particles having smaller agglomerate sizes and compatible surfaces enhance its degree of dispersion and compatibility. The improvement of physi-

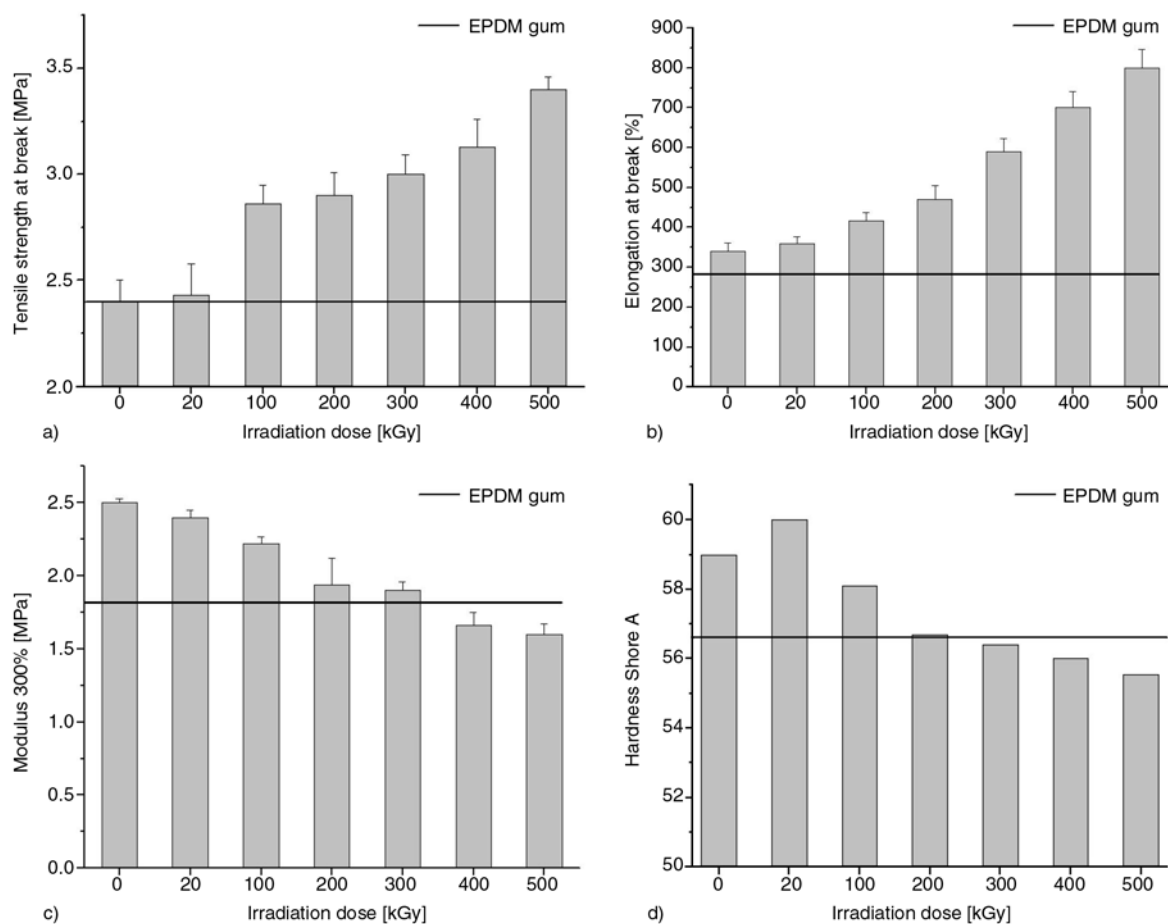


Figure 12. Tensile strength at break (a), elongation at break (b), modulus 300% (c) and hardness (d) as a function of absorbed dose of PTFE nanopowder in EPDM

cal properties of EPDM filled with electron treated PTFE is essentially due to the synergistic effect of their homogeneous dispersion and desirable compatibility. Figure 12c displays the stress at 300% elongation (so-called modulus 300%, M300) as a function of absorbed dose. The M300 decreases for modified PTFE filled EPDM with increasing irradiation dose. PTFE^{0 kGy}-EPDM shows the highest M300. However, the corresponding values of PTFE^{400 kGy}-EPDM and PTFE^{500 kGy}-EPDM are lower even than EPDM gum. Figure 12d shows the corresponding Shore A hardness values of PTFE-EPDM blends. The effect of absorbed dose of PTFE nanopowder on vulcanizate hardness can be seen in their decreasing values of hardness. EPDM filled with PTFE having absorbed irradiation doses higher than 20 kGy results in decreasing hardness values of PTFE-EPDM blends. PTFE^{20 kGy}-EPDM has the highest hardness while PTFE^{500 kGy}-EPDM showed the lowest. It is interesting to note that hardness of the blends above PTFE^{200 kGy}-EPDM is

even lower than that of EPDM gum. Non-modified PTFE nanopowder as shown in Figure 8 and 9 are huge uncovered agglomerates dispersed as solid rigid bodies in a matrix. Being incompatible they are not covered by EPDM molecules and hence tend to segregate in EPDM matrix. The presence of these huge inert bodies provides strength and hardness to the host matrix.

3.5. Reaction mechanism

The lack of reinforcement or compatibility of PTFE with other polymers is due to its inherent inert molecular structure. However, surface modification by high-energy electrons provides compatibility between PTFE and an unsaturated rubber matrix by a radical coupling reaction. The radicals of the irradiated PTFE react with olefinic unsaturated groups of EPDM as shown in Figure 13. Since several EPDM molecules are coupled to the surface of PTFE particles, these inter-chain bonds between

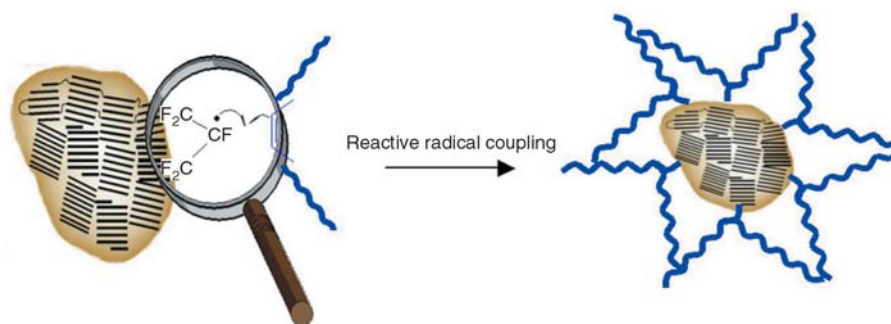


Figure 13. Radical coupling mechanism of modified PTFE radicals and the unsaturated diene EPDM

PTFE and EPDM provide compatibility by strong intermolecular network formation, the result of which is obvious in the improved physical properties of modified PTFE-EPDM blends.

4. Conclusions

We have described a method to develop PTFE coupled EPDM compounds with desired physical properties by simple, easy and effective controlled-modification of PTFE nanopowder. The existence of compatibility between modified PTFE nanopowder and EPDM was revealed by TEM, DSC and SEM. The resultant modified PTFE-EPDM blends demonstrate exceptionally enhanced physical properties by enwrapping of modified PTFE nanopowder by EPDM. Water contact angles indicate that the wettability of the modified PTFE nanopowder was increased by functional groups compared with non-modified PTFE nanopowder. The synergistic effect of enhanced compatibility by chemical coupling and micro-dispersion of PTFE agglomerates results in a significant improvement of physical properties of PTFE coupled EPDM compounds. In conclusion, PTFE coupled EPDM compounds prepared by the described approach offer the potential use of PTFE nanopowder in wide range of polymers for special purpose applications. Accordingly, they are promising in various fields.

Acknowledgements

We thank Solvay Solexis S.p.A. (Italy) for the free of charge supply of the special L100X PTFE nanopowder grade and U. Gohs for assisting in carrying out electron beam irradiation of PTFE nanopowder.

References

- [1] Gangal S. V.: Tetrafluoroethylene polymers. in 'Encyclopedia of polymer science and engineering' (eds.: Mark. H. F., Bikales N. M., Overberger C. G., Menges G.) Wiley, New York, Vol. **16**, 577–600 (1989).
- [2] Drobny J. G.: Fluoropolymers in automotive applications. *Polymers for Advanced Technologies*, **18**, 117–121 (2007).
- [3] Morgan R. A., Stewart C. W., Thomas E. W., Stahl W. M.: Reinforcement with fluoroplastic additives. *Rubber World*, **204**, 25–28 (1991).
- [4] Crandell W. H.: Evaluation of silicon rubber modified with teflon. *Rubber World*, 236–240 (1955).
- [5] Kaufman M. H., Gonzales J.: Reinforcement of fluoroelastomers with halopolymers. *Rubber Chemistry and Technology*, **41**, 527–532 (1968).
- [6] Akinay E., Tinçer T.: Radiation grafting of vinyl monomers onto poly(tetrafluoroethylene) powder produced by γ irradiation and properties of grafted poly(tetrafluoroethylene) filled low density polyethylene. *Journal of Applied Polymer Science*, **79**, 816–826 (2001).
- [7] Ji L. Y., Kang E. T., Neoh K. G., Tan K. L.: Oxidative graft polymerization of aniline on PTFE films modified by surface hydroxylation and silanization. *Langmuir*, **18**, 9035–9040 (2002).
- [8] Yu W. H., Kang E. T., Neoh K. G.: Controlled grafting of comb copolymer brushes on poly(tetrafluoroethylene) films by surface-initiated living radical polymerizations. *Langmuir*, **21**, 450–456 (2005).
- [9] Zhang M. C., Kang E. T., Neoh K. G., Tan K. L.: Consecutive graft copolymerization of glycidyl methacrylate and aniline on poly(tetrafluoroethylene) films. *Langmuir*, **16**, 9666–9672 (2000).
- [10] Kouichi K., Sato H., Katsuyama H.: Thiopyrylium compounds and photoconductive compositions containing said compounds. US patent 4469864, USA (1984).
- [11] Feiring A. E., Imbalzano J. F., Kerbow D. L.: Developments in commercial fluoroplastics. *Trends in Polymer Science*, **2**, 26–31 (1994).

- [12] Hillmyer M. A., Lodge T. P.: Synthesis and self assembly of fluorinated block-copolymers. *Journal of Polymer Science, Part A: Polymer Chemistry*, **40**, 1–8 (2002).
- [13] Lunkwitz K., Lappan U., Lehmann D.: Modification of fluoropolymers by means of electron beam irradiation. *Radiation Physics and Chemistry*, **57**, 373–376 (2000).
- [14] Lappan U., Lunkwitz K.: Radiation induced functionalization of fluoropolymers. *Zeitschrift für Physikalisch Chemie*, **191**, 209–218 (1995).
- [15] Lappan U., Geißler U., Lunkwitz K.: Electron beam irradiation of polytetrafluoroethylene in vacuum at elevated temperature: An infrared spectroscopy study. *Journal of Applied Polymer Science*, **74**, 1571–1576 (1999).
- [16] Lunkwitz K., Brink H-J., Handte D., Ferse A.: The radiation degradation of polytetrafluoroethylene resulting in low-molecular and functionalized perfluorinated compounds. *Radiation Physics and Chemistry*, **33**, 523–532 (1988).
- [17] Jun T., Quinji X.: Surface modification of PTFE by ^{60}Co γ -ray irradiation. *Journal of Applied Polymer Science*, **69**, 435–441 (1998).
- [18] Dorschner H., Lappan U., Lunkwitz K.: Electron beam facility in polymer research: radiation induced functionalization of polytetrafluoroethylene. *Nuclear Instruments and Methods In Physics Research, Section B*, **139**, 495–501 (1998).
- [19] Cheng S., Kerluke D. R.: Radiation processing for modification of polymers. in 'Annual Technical Conference of the Society of Plastic Engineering (ANTEC) IBA, Advanced Materials Division, 7695 Formula Place. San Diego, USA' (2003).
- [20] Jun T., Qunji X.: Surface modification of PTFE by ^{60}Co γ -ray irradiation. *Journal of Applied Polymer Science*, **69**, 435–441 (1998).
- [21] Lehmann D., Hupfer B., Lappan U., Pompe G., Häußler L., Jehnichen D., Janke A., Geißler U., Reinhardt R., Lunkwitz K., Franke R., Kunze K.: New PTFE-polyamide compounds. *Designed Monomers and Polymers*, **5**, 317–324 (2002).
- [22] Lehmann D., Hupfer B., Lappan U., Geißler U., Reinhardt R., Lunkwitz K.: Neue Polytetrafluoroethylen-Polyamid Compounds. *Materialwissenschaft und Werkstofftechnik*, **31**, 666–668 (2000).
- [23] Franke R., Lehmann D., Kunze K.: Tribological behaviour of new chemically bonded PTFE polyamide compounds. *Wear*, **262**, 242–252 (2007).
- [24] Klüpfel B., Lehmann D., Heinrich G., Linhart C., Haberstroh E., Kunze K., Hufenbach W., Dallner C., Künkel R., Ehrenstein G. W.: Kopplung von PTFE und Kautschuk- Eine neue elastomere Werkstoffklasse. *Kautschuk Gummi Kunststoffe*, **58**, 226–229 (2005).
- [25] Haberstroh E., Linhart C., Epping K., Schmitz T.: Verbesserte tribologische Eigenschaften von Elastomeren durch PTFE Pulver. *Kautschuk Gummi Kunststoffe*, **59**, 447–453 (2006).
- [26] Lee B-L., Patel R., Cox M., Andries J. C.: Polyvinyl chloride or polyolefin melt processable compositions containing polytetrafluoroethylene micropowder. US patent 6977280, USA (2005).
- [27] Lahijani J.: Melt-fabricable polytetrafluoroethylene. US patent 6265492, USA (2003).
- [28] Khan M. S., Lehmann D., Heinrich G.: Properties of the EPDM with modified PTFE nanopowder. *Kautschuk Gummi Kunststoffe*, **60**, 226–234 (2007).
- [29] Khan M. S., Lehmann D., Heinrich G., Franke R.: Physical and tribological properties of the modified PTFE nanopowder filled EPDM. *Wear*, in press (2008).
- [30] Khan M. S., Franke R., Lehmann D., Heinrich G.: Friction and wear behaviour of PTFE nanopowder-EPDM compounds. *Wear*, in press (2008).
- [31] Golden J. H.: The degradation of polytetrafluoroethylene by ionizing radiation. *Journal of Polymer Science*, **45**, 534–536 (1960).
- [32] Hagiwara M., Tagawa T., Amemiya H., Araki K., Shinohara J., Kagiya T.: Mechanism of thermal decomposition of peroxide radicals formed in polytetrafluoroethylene by γ -ray irradiation. *Journal of Polymer Science, Polymer Chemistry*, **14**, 2167–2172 (1976).
- [33] Fisher W. K., Corelli J. C.: Effect of ionizing radiation on the chemical composition, crystalline content and structure, and flow properties of polytetrafluoroethylene. *Journal of Polymer Science, Polymer Chemistry*, **19**, 2465–2493 (1981).
- [34] Häussler L., Pompe G., Lehmann D., Lappan U.: Fractionated crystallization in blends of functionalized poly(tetrafluoroethylene) and polyamide. in 'International Symposium on Reactive Polymers in Inhomogeneous Systems, in Melts and at Interfaces, Dresden, Germany' vol **164**, 411–419 (2001).
- [35] Pompe G., Häussler L., Pötschke P., Voigt D., Janke A., Geißler U., Hupfer B., Reinhardt G., Lehmann D.: Reactive polytetrafluoroethylene/polyamide compounds. I. Characterization of the compound morphology with respect to the functionality of the polytetrafluoroethylene component by microscopic and differential scanning calorimetry studies. *Journal of Applied Polymer Science*, **98**, 1308–1316 (2005).

Dielectric relaxations in PVDF/BaTiO₃ nanocomposites

C. V. Chanmal, J. P. Jog*

Polymer Science and Engineering Division, National Chemical Laboratory, Dr. Homi Bhabha Road, Pashan, Pune-411008, India

Received 28 January 2008; accepted in revised form 11 March 2008

Abstract. The present work aims at the study of molecular relaxations in PVDF/BaTiO₃ nanocomposites using broadband dielectric spectroscopy. The nanocomposites of PVDF with BaTiO₃ (10–30% by wt%) are prepared using simple melt mixing method. In dielectric permittivity study, two relaxation processes are identified corresponding to the crystalline, glass transition in the PVDF/BaTiO₃ nanocomposites. The peaks shift to higher frequencies as the temperature is increased. Electric modulus formalism is used to analyze the dielectric relaxations to overcome the conductivity effects at low frequencies. In M'' spectra two peaks are observed only at high temperature and low frequency whereas a single relaxation peak appears at low temperatures. The single relaxation peak appearing at low temperatures is the α_c relaxation attributed to crystalline chain relaxation in PVDF and the second relaxation peak which appears only at high temperatures and at a frequency lower than α_c relaxation is identified as MWS relaxation. The temperature dependence of α_c relaxation and MWS relaxation follows Arrhenius type behavior.

Keywords: nanocomposites, dielectric spectroscopy, MWS relaxation, interfacial polarization

1. Introduction

Nanocomposites of electroactive ceramics and a ferroelectric polymer are very attractive for many applications as their properties can be easily tailored to suit particular performance requirements [1]. In these nanocomposites, the final properties depend essentially on parameters such as grain size of ceramic, method of preparation of composites and on the dispersion of the ceramic particles into the polymer matrix [2–5]. PVDF is semicrystalline polymer with pyro and piezoelectric properties. Its high permittivity and relatively low dissipation factor made it a potential candidate to useful in many applications [6, 7]. The piezoelectric and pyroelectric properties of PVDF have led for intensive technological applications. Piezoelectric polymers have advantage over piezoelectric ceramics for certain applications wherein acoustic impedance similar to that of water or living tissue is required [8]. Due to

this reason PVDF is increasingly used for medical and industrial applications.

Although, there are several techniques to understand dynamics in polymer nanocomposites, dielectric spectroscopy is a well established tool for materials characterization [9, 10]. The magnitude and frequency location of the energy absorption associated with various processes depends critically on physical and chemical nature of the material [11].

In this article, we present the results of relaxations in PVDF/BaTiO₃ nanocomposites prepared by melt compounding technique. Although there have been few reports on PVDF/BaTiO₃ composites with high loading of BaTiO₃ (upto 50% by volume) the relaxations in this nanocomposites were not studied [12, 13]. In the present work, relaxations in PVDF/BaTiO₃ at low BaTiO₃ content i.e. upto 11.5% by volume are investigated using dielectric spec-

*Corresponding author, e-mail: jp.jog@ncl.res.in
© BME-PT and GTE

trospectroscopy over a temperature range from 30 to 150°C.

2. Experimental

2.1. Materials

PVDF grade, Solef 1008 (with weight-average molecular weight of $100 \cdot 10^3$ g/mol) procured by Solvay Belgium is used for this study. BaTiO₃ nanoparticles (formula weight = 233.24) of more than 99% purity are procured from Aldrich chemicals. The average diameter of the particle is around 30–50 nm.

2.2. Melt processing of PVDF/BaTiO₃ nanocomposites

The nanocomposites of PVDF with various weight percent of BaTiO₃ (10, 20 & 30% wt/wt) are processed via melt mixing in Thermo Haake Poly-lab batch mixer at 200°C, with 60 rpm for 5 minutes. The films of uniform thickness are compression molded at 200°C under 5-ton pressure using Carver Press (Germany). The thickness of the films is about 0.4 to 0.5 mm.

2.3. Characterization techniques

2.3.1. Scanning electron microscopy (SEM)

The dispersion of BaTiO₃ nanoparticles in the polymer matrix is determined from the morphology of fractured surfaces of PVDF/BaTiO₃ nanocomposites using Leica-440 scanning electron microscope. Cryo-fractured films are used for this purpose and fractured surfaces are sputtered by gold to avoid overcharging.

2.3.2. Dielectric relaxation spectroscopy (DRS)

Complex dielectric permittivity measurement of PVDF and PVDF/BaTiO₃ nanocomposites is done using Novocontrol broadband dielectric spectrometer with the ZGS active sample cell equipped with temperature controller and WinFit software for data analysis. The dielectric response of material in the frequency ranging from 10 MHz to 0.01 Hz over the temperature range of 30 to 150°C is measured by placing sample between two 20 mm gold plated electrodes. Quick drying silver paste is used to ensure good electrical contact.

3. Results and discussion

3.1. Morphology study

Figure 1a shows the transmission electron microscopy (TEM) micrograph of BaTiO₃ clusters. The average initial size of BaTiO₃ nanoparticles is around 50 nm as evidenced by TEM micrograph. The cryofractured surface morphology of PVDF/BaTiO₃ nanocomposites with scanning electron microscopy (SEM) is shown in Figure 1b. SEM micrograph reveals slight agglomeration of BaTiO₃ nanoparticles in the nanocomposites. The average aggregate size of filler in nanocomposites is around 100 nm. The microscopic observation validates the nano-dispersion of filler in the polymer matrix.

3.2. Dielectric relaxation spectroscopy (DRS) study

Dielectric spectroscopy has been widely used in polymer relaxation analysis and has the advantage over dynamic mechanical methods in that it covers much wider frequency ranges [14–17]. The study

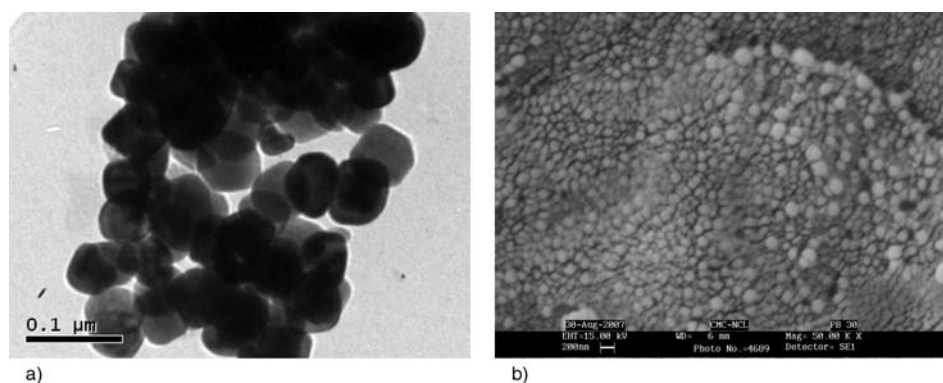


Figure 1. TEM micrograph of BaTiO₃ nanoparticles (a) and SEM micrographs of PVDF/BaTiO₃ nanocomposites with 30 wt% of BaTiO₃ nanoparticles (b)

of polymers as a function of frequency and temperature can be used to elucidate the effects due to intermolecular co-operative motions and hindered dielectric rotations.

3.2.1. Frequency dependence of dielectric constant at 30°C

Figure 2 shows the typical dielectric permittivity (ϵ') and dielectric loss (ϵ'') of PVDF/BaTiO₃ nanocomposites as a function of frequency at 30°C. As expected, the dielectric constant of PVDF/BaTiO₃ nanocomposites increases with the increase in BaTiO₃ content. It can be found that dielectric permittivity measured at lower frequency is always greater than higher frequency. With the increasing frequency, dielectric constant decreases very fast upto 10⁺⁰² Hz and in frequency range from 10⁺⁰² to 10⁺⁰⁶ Hz it is almost constant. In the studied frequency range 10⁻⁰² to 10⁺⁰⁷ Hz, the decrease in dielectric constant of PVDF/BaTiO₃ nanocomposites with increase in frequency is similar to that of PVDF. The frequency dependence of dielectric study indicates that introduction of BaTiO₃

increases the dielectric constant of the PVDF from about 11 to 25 at 30 wt% of BaTiO₃ content.

The permittivity loss curve at 30°C shows two relaxations. The peak at 10⁺⁰⁷ Hz is related to the glass transition relaxation of PVDF and is denoted as α_a relaxation [6, 8, 17, 18]. The frequency and temperature limit of instrument constraints the full view of α_a relaxation. Earlier literature work confirms peak at 10⁺⁰⁷ Hz to be related to the micro-Brownian cooperative motions of the main chain backbone and is dielectric manifestation of the glass transition temperature of PVDF [19]. The relaxation peak at about 10⁺⁰⁰ Hz is attributed to α_a relaxation and is associated with the molecular motions in crystalline region of PVDF. The presence of α_a relaxation peak in PVDF/BaTiO₃ nanocomposites explains the non-polar i.e. α phase of PVDF in nanocomposites [20]. Several interpretations of these transitions are reported [21–23]. Takahashi and Miyaji have attributed this relaxation to the reversible conformation rearrangement in the crystals while Nagakawa and Ishida have attributed this relaxation to the molecular motions in chain folds of crystalline lamellae and in the interior of crystals. Miyamoto *et al.* have ascribed this transition to the change in conformation with internal rotation that occur in crystalline phase and have reported that the defects in the crystalline phase play a major role.

3.2.2. Temperature dependence of dielectric constant

The temperature dependence of dielectric permittivity for PVDF is shown in Figure 3. As can be seen, the dielectric permittivity increases with increasing temperature. The room temperature value of permittivity at frequency 10⁻⁰² Hz is about 15, which increase to about 42 at 90°C. In case of permittivity loss curves, the α_a relaxation corresponding to the glass transition temperature shifts to higher frequency with increasing temperature and thus can not be detected in this experimental window, while the crystalline relaxation is clearly visible. The frequency dependence of dielectric loss can be described by Havriliak–Negami (HN) function.

Havriliak–Negami (HN) functional formalism [19] that can be phenomenologically described as a

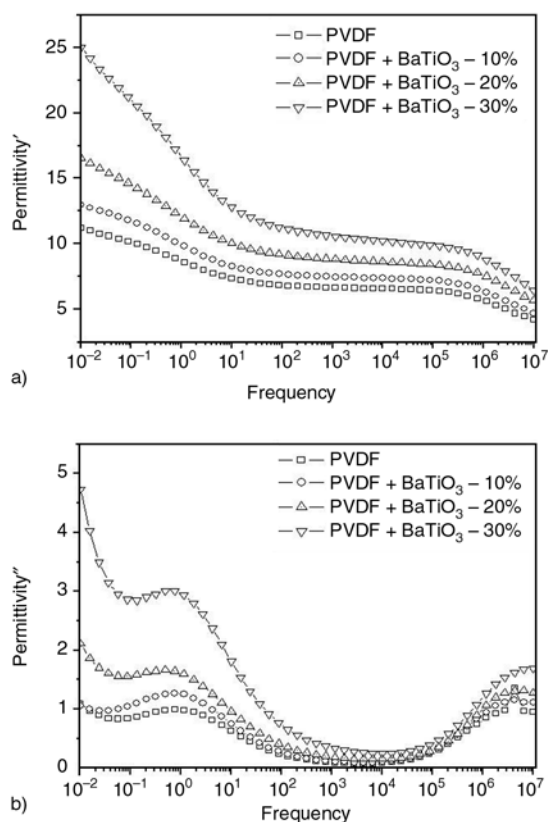


Figure 2. Dielectric permittivity (ϵ') (a) and loss (ϵ'') (b) of PVDF and PVDF/BaTiO₃ nanocomposites as a function of frequency at 30°C

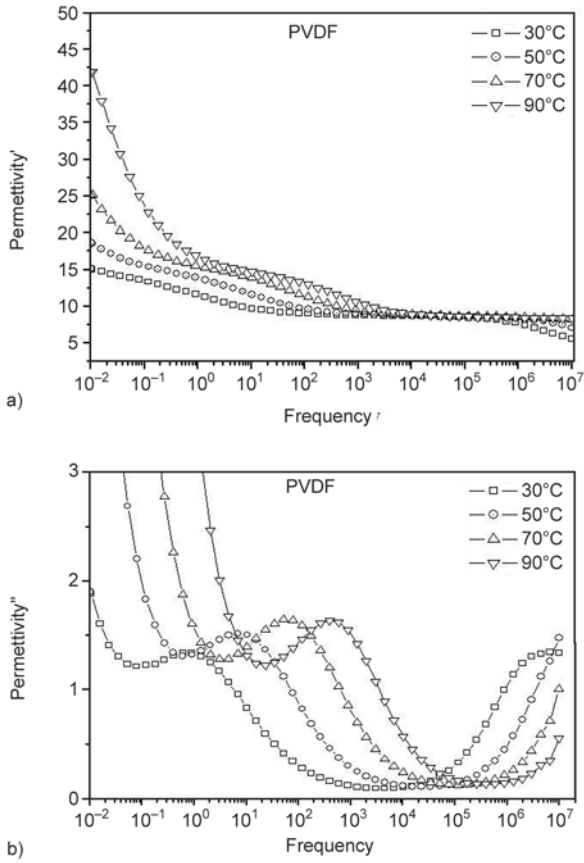


Figure 3. Dielectric permittivity (ϵ') (a) and loss (ϵ'') (b) at various temperatures for PVDF

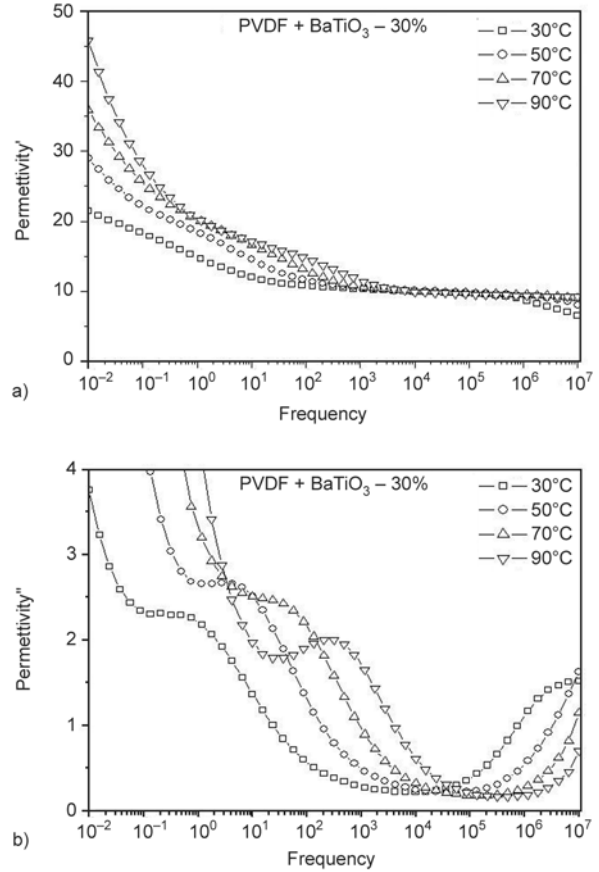


Figure 4. Dielectric permittivity (ϵ') (a) and loss (ϵ'') (b) at various temperatures for PVDF/BaTiO₃ - 30%

combination of the conductivity term with the HN functional form as Equation (1):

$$\epsilon(\omega) = \epsilon' - i\epsilon'' = -i \left(\frac{\sigma_{dc}}{\epsilon_0 \omega} \right)^N + \sum_{k=\beta, \alpha} \left[\frac{\Delta\epsilon_k}{(1 + (i\omega\tau_{HNk})^{a_k})^{b_k}} \right] \quad (1)$$

where σ_{dc} is the direct current electrical conductivity, $\omega = 2\pi f$ is the angular frequency, ϵ_0 denotes the vacuum permittivity, N is an exponent ($0 < N < 1$), $\Delta\epsilon_k$ is the dielectric of the k^{th} process, τ_{HNk} is the most probable value of the central relaxation time distribution function, and a_k and b_k are shape parameters related to symmetric and asymmetric broadening of the relaxation peak, respectively. All HN fits reported here were performed using WinFit software program provided with the Novocontrol dielectric analyzer. The values of the HN parameters a and b for the nanocomposites were found to be similar to those of pure PVDF. This suggests that the intermolecular and intramolecular interac-

tions that arise in the polymer and the nanocomposites are almost identical.

PVDF/BaTiO₃ composites exhibit the similar dielectric behavior to that of PVDF as shown in Figure 4. However, the most apparent difference between PVDF and PVDF/BaTiO₃ nanocomposites can be seen at low frequency region. The conductivity effect in the low frequency is more pronounced in PVDF/BaTiO₃ nanocomposites as compared to that of PVDF. This behavior is similar to that observed in polyisoprene and organically modified Cloisite 25A nanocomposites [24]. The increase in the values of the permittivity and the displacement of the peak maximum of permittivity with the temperature are characteristic behavior of dielectric dispersion. Most generally, in the system with low conductivity the rapid increase of the permittivity at very low frequency is due to the electrode polarization and the effect of electrode polarization can completely masks the low frequency relaxation.

To overcome the electrode polarization effect and to resolve low frequency relaxation, ‘electric mod-

ulus' formalism is used for the study of dielectric relaxations. The electric modulus formalism is introduced by McCrum *et al.* [11] and it is used to study electrical relaxation phenomena in many polymers [25–27].

The electric modulus is defined by the Equation (2):

$$M^* = \frac{1}{\epsilon^*}, \quad M' = \frac{\epsilon'}{\epsilon'^2 + \epsilon''^2}, \quad M'' = \frac{\epsilon''}{\epsilon'^2 + \epsilon''^2} \quad (2)$$

where M' and M'' are the real and the imaginary part of electric modulus respectively, and ϵ' and ϵ'' are the real and the imaginary part of dielectric permittivity.

Figure 5a shows typical 3D plots of dielectric modulus spectra for pure PVDF at various temperatures as a function of frequency. Two relaxation processes can be clearly observed in the M'' curves. The

relaxation peak at high frequency side is identified as fast symmetric crystalline relaxation and it shifts to higher frequency with the increasing temperature.

At high temperature, another peak appears in modulus spectra. This is attributed to Maxwell–Wagner–Sillars (MWS) polarization which can be seen in the heterogeneous materials and is also known as interfacial polarization. At temperature about 70°C the MWS relaxation peak starts appearing in PVDF whereas in PVDF/BaTiO₃ nanocomposites the MWS peak is seen at higher temperature about 90°C. In semicrystalline polymers, the crystalline regions are dispersed in amorphous matrix and MWS relaxation is observed in these materials due to the differences in the conductivity and permittivity values of the crystalline and amorphous phases [28, 24]. For heterogeneous composite, an interfacial polarization is almost always present because of filler additives or even impurities that migrate

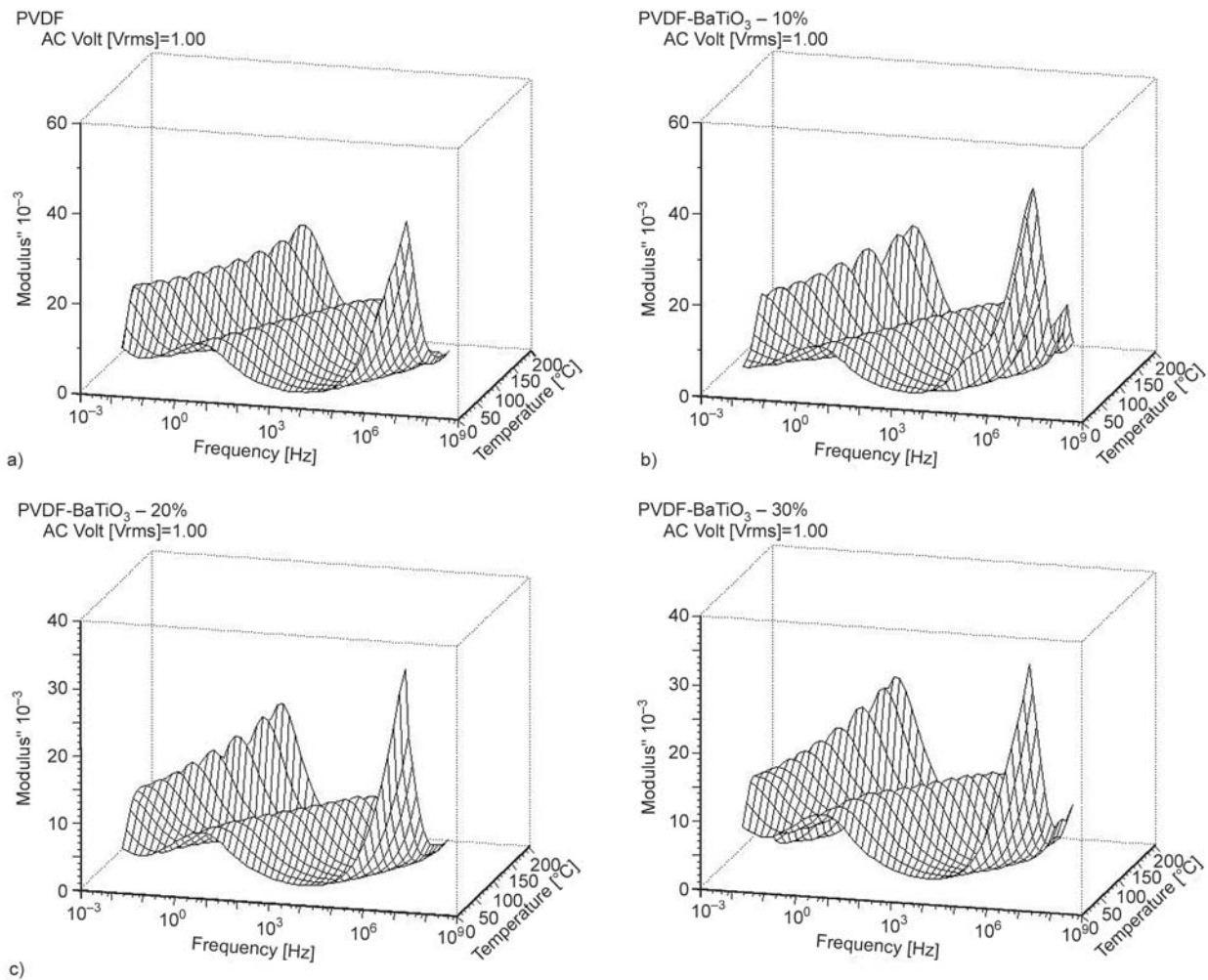


Figure 5. 3D plot of isothermal curves for PVDF (a), 3D plot of isothermal curves for PVDF/BaTiO₃ – 10% (b), 3D plot of isothermal curves for PVDF/BaTiO₃ – 20% (c), 3D plot of isothermal curves for PVDF/BaTiO₃ – 30% (d)

towards the interface [29]. The M'' peaks for both relaxation processes shift to a higher frequency with increasing temperature. In addition, there is no significant change in the dielectric relaxation peak height for crystalline relaxation process, however, the intensity of dielectric relaxation peak at low frequency side increases with temperature and peak broadening decreases signifying asymmetric nature of MWS relaxation. Similar dielectric relaxation in the low frequency region below that of crystalline relaxation (α_c) is noted in earlier work on PVDF and this relaxation is ascribed to be interfacial or MWS polarization [30].

The relaxation peaks of PVDF and PVDF/BaTiO₃ nanocomposites as a function of frequencies at 120°C are shown in Figure 6. In case of α_c relaxation, peak appears at same frequency for polymer and nanocomposites, whereas MWS peak for PVDF/BaTiO₃ nanocomposites shifts to lower frequency as compared to PVDF. It can also be seen that the intensity of MWS relaxation decreases with increasing content of BaTiO₃ which is characteristic of MWS relaxation [31, 32]. Similar behavior is observed for PVDF/BaTiO₃ nanocomposites at all measured temperatures.

The temperature dependence of a relaxation process is further analyzed by plotting the frequency maximum versus reciprocal of temperature. Figure 7 shows the activation energy plots of PVDF for two relaxation processes observed. The relaxation time decreases with increasing temperature due to enhancement of mobility of charge carriers at high temperature. The temperature dependence of dielectric relaxation can be well described by the Arrhenius type behavior.

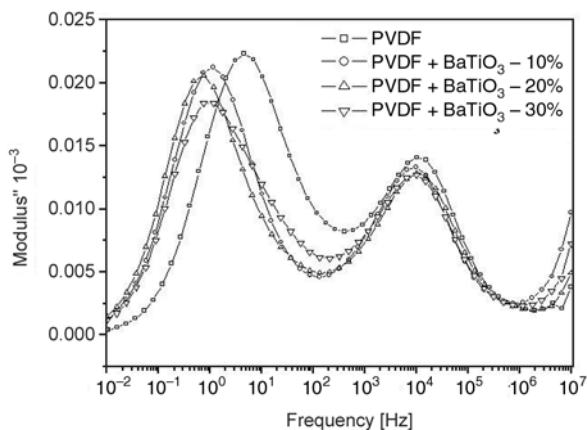


Figure 6. Comparison of dielectric modulus spectra of PVDF and PVDF/BaTiO₃ nanocomposite at 120°C as a function of frequency

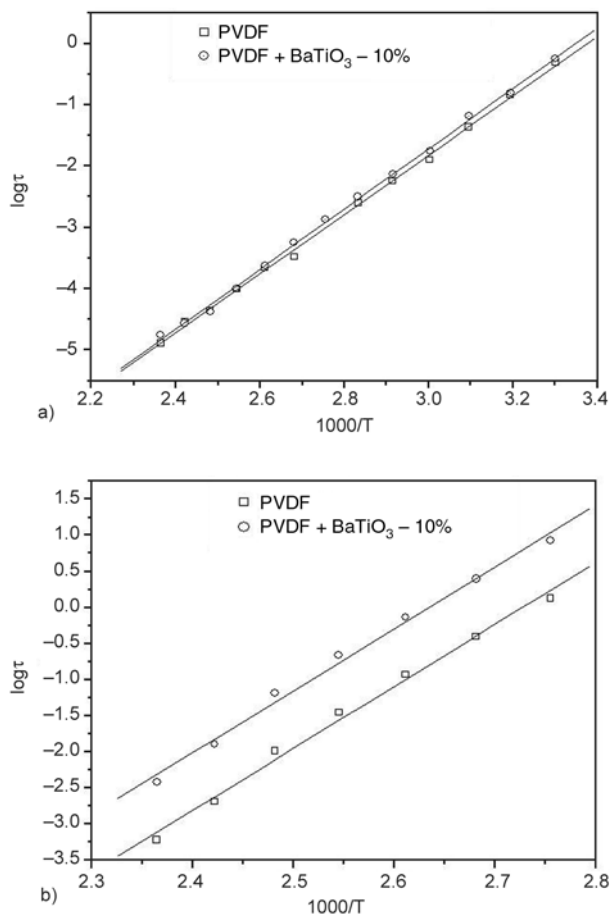


Figure 7. Activation energy plot for crystalline relaxation (a) and MWS relaxation (b) showing Arrhenius type behavior

The plot for crystalline relaxation process yields straight line and from the slope of the line activation energy can be calculated using Arrhenius equation (3):

$$f = f_0 \exp\left(-\frac{E_a}{kT}\right) \tag{3}$$

where f – frequency maximum in permittivity loss spectra, E_a – activation energy, k – Boltzmann’s constant.

The activation energy was calculated for the crystalline relaxation, α_c , for PVDF and PVDF/BaTiO₃ nanocomposites. The activation energy was found to be about 0.41 eV for PVDF as well as PVDF/BaTiO₃ nanocomposites. This value is in good agreement with the reported value of activation energy for crystalline relaxation (α_c) in PVDF [33]. The MWS relaxation shows Arrhenius type behavior indicating relaxation is thermally activated process. Table 1 summarizes the obtained results

Table 1. Fitting parameters for α_c relaxation and MWS relaxation

	α_c relaxation		MWS relaxation	
	log τ [sec]	W [eV]	log τ [sec]	W [eV]
PVDF	-16.41	0.42	-23.47	1.80
PVDF+BaTiO ₃ -10%	-16.32	0.41	-22.59	1.70
PVDF+BaTiO ₃ -20%	-16.22	0.41	-21.14	1.64
PVDF+BaTiO ₃ -30%	-15.93	0.40	-20.65	1.60

for the activation energies of α_c relaxation and MWS polarization.

4. Conclusions

PVDF/BaTiO₃ nanocomposites are prepared using simple melt mixing technique. The BaTiO₃ nanoparticles are well dispersed in the PVDF matrix as evidenced by the scanning electron micrographs. The dielectric permittivity increases with increasing BaTiO₃ content. The room temperature dielectric spectra show two relaxations processes corresponding to the T_g and α_c relaxation while at high temperature another low frequency relaxation is observed which is attributed to the MWS relaxation. The temperature dependence of α_c relaxation and MWS relaxation follows Arrhenius type behavior. The activation energies of crystalline relaxation of MWS relaxation are not changed in nanocomposites.

Acknowledgements

Authors would like to thank Mr.A.B.Gaikwad for his help in the SEM study.

References

- [1] Hilczer B., Kulek J., Markiewicz E., Kosec M., Malic B.: Dielectric relaxation in ferroelectric PZT-PVDF nanocomposites. *Journal of Non-Crystalline Solids*, **5**, 167–173 (2002).
- [2] Chiang C. K., Popielarz R.: Polymer composites with high dielectric constant. *Ferroelectrics*, **275**, 1–9 (2002).
- [3] Kontos G. A., Soulintzis A. L., Karahaliou P. K., Psarras G. C., Georga S. N., Krontiras C. A., Pisanias M. N.: Electrical relaxation dynamics in TiO₂-polymer matrix composites. *Express Polymer Letters*, **1**, 781–789 (2007).
- [4] Psarras G. C., Gatos K. G., Karahaliou P. K., Georga S. N., Krontiras C. A., Karger-Kocsis J.: Relaxation phenomena in rubber/layered silicate nanocomposites. *Express Polymer Letters*, **1**, 837–845 (2007).
- [5] Ishida H., Campbell S., Blackwell J.: General approach to polymer nanocomposite preparation. *Chemistry of Materials*, **12**, 1260–1267 (2000).
- [6] Gregorio R. Jr., Cestari M.: Effect of crystallization temperature on the crystalline phase content and morphology of poly (vinylidene fluoride). *Journal of Polymer Science, Part B: Polymer Physics*, **32**, 859–870 (1994).
- [7] Pramoda K. P., Mohamed A., Phang I. Y., Liu T.: Crystal transformation and thermomechanical properties of poly (vinylidene fluoride)/clay nanocomposites. *Polymer International*, **54**, 226–232 (2005).
- [8] Gregorio R. Jr., Ueno E. M.: Effect of crystalline phase, orientation and temperature on the dielectric properties of poly (vinylidene fluoride) (PVDF). *Journal of Material Science*, **34**, 4489–4500 (1999).
- [9] Kremer F.: Dielectric spectroscopy: Yesterday, today and tomorrow. *Journal of Non-Crystalline Solids*, **305**, 1–9 (2000).
- [10] Djidjelli H., Benachour D., Boukerrou A., Zefouni O., Martinez-Véga J., Farenc J., Kaci M.: Thermal, dielectric and mechanical study of poly (vinyl chloride)/olive pomace composites. *Express Polymer Letters*, **1**, 846–852 (2007).
- [11] McCrum N. G., Read B. E., Williams G.: Anelastic and dielectric effects in polymeric solids. Wiley, London (1967).
- [12] Dang Z-M., Wang H-Y., Zhang Y-H., Qi J-Q.: Morphology and dielectric property of homogenous BaTiO₃/PVDF nanocomposites prepared via the natural adsorption action of nanosized BaTiO₃. *Molecular Rapid Communications*, **26**, 1185–1189 (2005).
- [13] Sekar R., Tripathi A. K., Pillai P. K. C.: X-ray diffraction and dielectric studies of a BaTiO₃: PVDF composite. *Materials Science and Engineering: B*, **5**, 33–36 (1989).
- [14] Madbouly S. A., Otaigbe J. U.: Broadband dielectric spectroscopy of nanostructured maleated polypropylene/polycarbonate blends prepared by in situ polymerization and compatibilization. *Polymer*, **48**, 4097–4107 (2007).
- [15] Mijovic J., Sy J. W., Kwei T. K.: Reorientational dynamics of dipoles in poly (vinylidene fluoride)/poly (methyl methacrylate) (PVDF/PMMA) blends by dielectric spectroscopy. *Macromolecules*, **30**, 3042–3050 (1997).
- [16] Lu H., Zhang X.: Investigation of MWS relaxation in Nylon 1010 using dielectric relaxation spectroscopy. *Journal of Macromolecular Science, Part B: Physics*, **45**, 933–944 (2006).
- [17] Linares A., Nogales A., Rueda D. R., Ezquerro T. A.: Molecular dynamics in PVDF/PVA blends as revealed by dielectric loss spectroscopy. *Journal of Polymer Science, Part B: Polymer Physics*, **45**, 1653–1661 (2007).

- [18] Sy J. W., Mijovic J.: Reorientational dynamics of poly(vinylidene fluoride)/poly(methyl methacrylate) blends by broad-band dielectric relaxation spectroscopy. *Macromolecules*, **33**, 933–946 (2000).
- [19] Bello A., Laredo E., Grimau M.: Distribution of relaxation times from dielectric spectroscopy using Monte Carlo simulated annealing: Application to α -PVDF. *Physical Review: B*, **60**, 12764–12774 (1999).
- [20] Kochervinskii V. V., Malyshkina I. A., Markin G. V., Gavrilova N. D., Bessonova N. P.: Dielectric relaxation in vinylidene fluoride-hexafluoropropylene copolymers. *Journal of Applied Polymer Science*, **105**, 1107–1117 (2007).
- [21] Takahashi Y., Miyaji K.: Long-range order parameters of form II of poly (vinylidene fluoride) and molecular motion in the α_c relaxation. *Macromolecules*, **16**, 1789–1792(1983).
- [22] Nakagawa K., Ishida Y.: Dielectric relaxations and molecular relaxation in poly (vinylidene fluoride) with crystal form II. *Journal of Polymer Science*, **11**, 1503–1533 (1973).
- [23] Miyamoto Y., Miyaji H., Asai K.: Anisotropy of dielectric relaxation in crystal form II of poly (vinylidene fluoride). *Journal of Polymer Science, Part B: Polymer Physics*, **18**, 597–606 (1980).
- [24] Mijović J., Lee H., Kenny J., Mays J.: Dynamics in polymer-silicate nanocomposites as studied by dielectric relaxation spectroscopy and dynamic mechanical spectroscopy. *Macromolecules*, **39**, 2172–2182 (2006).
- [25] Tsangaris G. M., Psarras G. C., Kouloumbi N.: Electric modulus and interfacial polarization in composite polymeric systems. *Journal of Materials Science*, **33**, 2027–2037 (1998).
- [26] Starkweather H. W., Avikian P.: Conductivity and the electric modulus in polymers. *Journal of Polymer Science, Part B: Polymer Physics*, **30**, 637–641(1992).
- [27] Hodge I. M., Eisenberg A.: Conductivity relaxation in an amorphous iron containing organic polymer. *Journal of Non-Crystalline Solids*, **27**, 441–443 (1978).
- [28] Arous M., Ben Amor I., Kallel A., Fakhfakh Z., Perrier G.: Crystallinity and dielectric relaxations in semicrystalline poly(ether ether ketone). *Journal of Physics and Chemistry of Solids*, **68**, 1405–1414 (2007).
- [29] Psarras G. C., Manolakaki E., Tsangaris G. M.: Dielectric dispersion and ac conductivity in – iron particles loaded – polymer composites. *Composites, Part A: Applied Science and Manufacturing*, **34**, 1187–1198 (2003).
- [30] Sasabe H., Saito S. A., Asahina M., Kakutani H.: Dielectric relaxation in poly (vinylidene fluoride). *Journal of Polymer Science, Part A-2*, **7**, 1405–1414 (1969).
- [31] Suzhu Y., Hing P., Xiao H.: Dielectric properties of polystyrene-aluminum-nitride composites. *Journal of Applied Physics*, **88**, 398–405 (2000).
- [32] Daly J. H., Guest M. J., Hayward D., Pethrick R. A.: The dielectric properties of polycarbonate/styrene-acrylonitrile copolymer multiplayer composites part II The Maxwell-Wagner-Sillars process. *Journal of Materials Science Letters*, **11**, 1271–1273 (1992).
- [33] Tuncer E., Wagener M., Gerhard-Mülhaupt R.: Distribution of relaxation times in α -phase Polyvinylidene fluoride. *Journal of Non-Crystalline Solids*, **351**, 2917–2921 (2005).

Modification of (DGEBA) epoxy resin with maleated depolymerised natural rubber

K. Dinesh Kumar^{1,2}, B. Kothandaraman^{1*}

¹Department of Rubber and Plastics Technology, MIT campus, Anna University, Chennai-6000 44, India

²Current address: Rubber Technology Centre, Indian Institute of Technology, Kharagpur-721302, India

Received 30 December 2007; accepted in revised form 13 March 2008

Abstract. In this work, diglycidyl ether of bisphenol A (DEGBA) type epoxy resin has been modified with maleated depolymerised natural rubber (MDPR). MDPR was prepared by grafting maleic anhydride onto depolymerised natural rubber. MDPR has been characterized by Fourier transform infrared (FT-IR) spectroscopy and nuclear magnetic resonance spectroscopy. MDPR was blended with epoxy resin at three different ratios (97/3, 98/2 and 99/1), by keeping the epoxy resin component as the major phase and maleated depolymerised natural rubber component as the minor phase. The reaction between the two blend components took place between the acid/anhydride group in the MDPR and the epoxide group of the epoxy resin. The proposed reaction schemes were supported by the FT-IR spectrum of the uncured Epoxy/MDPR blends. The neat epoxy resin and Epoxy/MDPR blends were cured by methylene dianiline (DDM) at 100°C for three hours. Thermal, morphological and mechanical properties of the neat epoxy and the blends were investigated. Free volume studies of the cured, neat epoxy and Epoxy/MDPR blends were correlated with the morphological and mechanical properties of the same systems using Positron Annihilation Lifetime Studies.

Keywords: *thermosetting resins, epoxy resin, maleated depolymerised natural rubber, blending, positron annihilation lifetime studies*

1. Introduction

Epoxy resins are very important class of thermosetting polymers that often exhibit high tensile strength and modulus, excellent chemical and corrosion resistance and good dimensional stability. Hence they are widely used in structural adhesives, surface coatings, engineering composites, electrical laminates etc. [1]. The major drawback of epoxy resins in the cured state is that they are extremely brittle materials having fracture energies two orders of magnitude lower than engineering thermoplastics and three orders lower than metal [1–3]. As the result they have limited utility in applications requiring high impact and fracture strengths. This inherent brittleness causes poor peeling and shear strength of epoxy based adhesives [3]. Hence

toughening of epoxy resin has been the subject of intense investigation throughout the world. Epoxy resins are most successfully toughened by dispersing rubber particles as a distinct phase of microscopic particles in the epoxy matrix [4].

This can be achieved by two ways: 1) by blending with low molecular weight functionalized liquid rubbers, having restricted solubility and limited compatibility with epoxy hardener mixture and undergo phase separation at a certain stage of curing reaction leading to a two phase microstructure, 2) by directly dispersing preformed rubbery particles in the epoxy matrix. Rubber toughened epoxies was first reported by McGarry and Willner in 1968, using low molecular weight carboxyl terminated copolymer of butadiene and acrylonitrile (CTBN,

*Corresponding author, e-mail: bkraman_mitindia@yahoo.co.in
© BME-PT and GTE

Goodrich) [5]. They modified different grades of diglycidyl ether of bisphenol A (DGEBA) epoxies with CTBN and cured with piperidine to get a network having two-phase microstructure and reported a ten-fold increase in fracture toughness. Approximately 5–20% of low molecular weight reactive liquid rubbers like CTBN dispersed in the hot epoxy resin can lead to a multiphase toughened epoxy system on curing [5, 6]. To optimize toughening, parameters such as modifier structure, molecular weight, solubility and rubber concentration must be clearly defined. These parameters are responsible for the dynamics of multiphase morphology [5, 6]. Following this pivotal work extensive research has been done for the past two and a half decades to understand the principle of morphology development, morphology and fracture property relationship and the mechanism of toughening [7–10]. Nowadays various functionalized synthetic liquid rubbers have been synthesized and investigated as a replacement of CTBN rubber [10–14].

However, till today, a liquid modifier for epoxy resin which is easily available and easy to modify has not been explored. Therefore, in this work, epoxy resin has been modified with depolymerised natural rubber (DPR), a rubber which is very easily available. Depolymerised natural rubber (DPR) has been functionalized by grafting maleic anhydride on it by a simple thermal reaction between the depolymerised natural rubber (DPR) and maleic anhydride. In this paper the role of maleated depolymerised natural rubber (MDPR) as a modifier for the liquid epoxy resin has been studied with reference to the mechanical, thermal, and morphological properties of the cured neat epoxy and Epoxy/MDPR blends. Furthermore, the effect of modifier on the mechanical and morphological properties and their correlation with the free volume data have been analyzed using positron annihilation lifetime spectroscopy (PALS).

Positron annihilation lifetime spectroscopy (PALS) is a sophisticated tool used for determining the nanometer sized free volume holes and their relative number densities (i.e. concentration) in polymers [15, 16]. Till today, only few reports are available regarding the free volume studies of the rubber modified epoxies through PALS technique [17–18]. Especially PALS studies of epoxy-depolymerised natural blends are not available. Therefore, in this paper, PALS has been used as a complemen-

tary tool to understand the relationship between the free volume and the mechanical properties of the cured neat epoxy and Epoxy/MDPR blend.

2. Materials and methods

2.1. Materials

Depolymerised natural rubber (DPR) with number average molecular weight (M_n) around 36 000 g/mol was obtained from Carborundum universal India private limited, Chennai, India. (DGEBA) liquid epoxy resin with the epoxy equivalent of 170 g was used as received from Ciba-Geigy India private limited, Mumbai, India. Methylene dianiline (DDM) (HT 972) curing agent was used as received from Ciba-Geigy India private limited, Mumbai, India. Maleic anhydride (Laboratory Reagent) and Triphenylphosphine (Laboratory Reagent) were used as received from Hipure chemicals India private limited, Chennai, India.

2.2. Synthesis of maleated depolymerised natural rubber (MDPR)

20 g of depolymerised natural rubber (DPR) was placed in a 100 ml two necked glass beaker fitted with a stirrer, thermometer and a gas inlet. After the system was well purged with an inert gas the temperature was brought to be in the range of 200–230°C. The system was allowed to remain in the same temperature for 10 minutes. Then 2 phr (parts per hundred on depolymerised natural rubber) of maleic anhydride was added to the system and nitrogen was bubbled slowly to remove dissolved oxygen. The mixture was heated and stirred at the temperature between 200–230°C for 20 minutes. Then the mixture is allowed to cool to room temperature. Then maleated depolymerised natural rubber (MDPR) was removed from the beaker.

2.3. Percentage grafting of maleic anhydride

The maleic anhydride grafted sample was taken in a filter paper and placed in the Soxhlet apparatus for extraction. Each extraction was carried out for 24 h, using acetone as the extracting medium for complete removal of unreacted maleic anhydride. The grafted polymer (MDPR) is fully insoluble in acetone. After the extraction, the samples within filter paper were dried under vacuum for 72 h at 70°C till

they showed no weight variation (W_g). The extent of grafting was calculated from the weight gain by the samples using the Equation (1):

$$[\%] \text{ Grafting} = \frac{W_g - W_0}{W_0} \cdot 100 \quad (1)$$

where, W_g – weight of grafted DPR and W_0 – weight of DPR before grafting.

2.4. Epoxy-MDPR network formation

The epoxy resin and maleated depolymerised natural rubber (MDPR) mixtures were blended with each other in the ratio 97/3, 98/2, 99/1, by keeping the epoxy resin component as the major phase and maleated depolymerised natural rubber component as the minor phase. The epoxy resin and maleated depolymerised natural rubber mixtures were heated in a beaker at 120°C (with 1% triphenylphosphine catalyst) for 1 hour. The Epoxy/MDPR mixtures were allowed to reach room temperature. 27 phr of methylene dianiline (curing agent) was slowly dissolved in neat epoxy and in each 99/1, 98/2, 97/3 (Epoxy/MDPR) mixtures at 80°C, under vacuum to remove entrapped air bubbles. Then they were mixed and poured in aluminum molds, and allowed to cure at 100°C for 3 hours. The samples neat epoxy, 99/1, 98/2, 97/3 (Epoxy/MDPR) blends were designated as E0, E1, E2 and E3 respectively.

2.5. Fourier transform infrared spectroscopy (FT-IR)

The infrared spectroscopy of the maleated depolymerised natural rubber and Epoxy/MDPR (uncured state) blends were recorded in with a Perkin-Elmer FT-IR spectrophotometer. The FT-IR spectra of the samples (liquid state) were taken at room temperature (25°C) using an optical cell. The samples were scanned from 4000 to 400 cm^{-1} with a resolution of 4 cm^{-1} . All spectra were reported after an average of 32 scans.

2.6. Nuclear magnetic resonance spectroscopy (NMR)

The $^1\text{H-NMR}$ spectroscopy of the maleated depolymerised natural rubber was recorded with Bruker AC-200 spectrometer (Switzerland) at 200 MHz with CDCl_3 as solvent.

2.7. Measurement of glass transition temperature (T_g) by differential scanning calorimetry (DSC)

The T_g of the cured neat epoxy and Epoxy/MDPR blends was measured by differential scanning calorimetry (DSC), NETZSCH DSC 204 in the temperature range of 30 to 200°C at a heating rate of 10°C per minute. The samples of 5–10 mg were encapsulated in standard aluminum pans.

2.8. Mechanical properties

2.8.1. Tensile stress-strain properties of neat epoxy and Epoxy/MDPR blends

The tensile tests were carried according to ASTM D 638. The tensile specimens with dimension of 60 mm×10 mm with thickness of 2 mm were prepared by casting. The tensile strength, tensile modulus and elongation at break values of the neat epoxy and Epoxy/MDPR blends were identified. The tensile tests were carried at a cross head speed of 1 mm/min. Five test samples from each formulation were tested and the average values were reported.

2.8.2. Flexural stress-strain properties of neat epoxy and Epoxy/MDPR blends

The flexural tests were carried according to ASTM D 790. The flexural specimens with dimension of 80 mm×25 mm with thickness of 2 mm were prepared by casting. The flexural strength, flexural modulus and flexural strain to failure values of the neat epoxy and Epoxy/MDPR blends were identified. The flexural tests were carried at a cross head speed of 3 mm/min. Five test samples from each formulation were tested and the average values were reported.

2.8.3. Izod unnotched impact test of neat epoxy and Epoxy/MDPR blends

The Izod unnotched impact test was carried out according to ASTM D 4812-93 specifications using an impact tester with a striking velocity of 3.35 $\text{m}\cdot\text{s}^{-1}$. Impact test specimens in all the cases were prepared by casting in to rectangular shaped cavities (125×10×10 mm^3). Tests are run on a TMT N 431 impact tester type machine equipped

with a hammer. Five test samples from each formulation were broken. Average impact strength (IS) values were reported. The impact test was carried out at 25°C and the impact energy was reported in J·m⁻². The Izod IS is calculated by Equation (2):

$$IS = \frac{U_1 - U_2}{w \cdot t} \quad [\text{J/m}^2] \quad (2)$$

where U_1 is the impact energy [J], U_2 the residual energy [J], w , the specimen width [m], and t , the specimen thickness [m].

2.9. Morphological study

Scanning electron microscopy (SEM) studies

Morphological analysis of the tensile fractured neat epoxy and Epoxy/MDPR blends were studied using JEOL (JSM-5800) Scanning electron microscopy after sputter coating the fractured sample surface with gold.

2.10. Positron annihilation lifetime measurements

Positron annihilation lifetime spectra were recorded for the cured neat epoxy and Epoxy/MDPR blends using positron lifetime spectrometer. The spectrometer consists of a fast-fast coincidence system with BaF₂ scintillators coupled to photomultiplier tubes type XP2020/Q with quartz window as detectors. The BaF₂ scintillators were conical shaped to achieve better time resolution. The two identical pieces of the sample were placed on either side of a 17 μCi ²²Na (a 17 micro Curie Na-22) positron source, deposited on a pure Kapton foil of 0.0127 mm thickness. This sample-source sandwich was placed between the two detectors of the spectrometer to acquire lifetime spectrum. The ⁶⁰Co source was used to acquire the prompt time spectrum, which gave 180 ps as the resolution of the spectrometer. However, to reduce the acquisition time and increase the count rate, the spectrometer was operated at 220 ps. All lifetime measurements were performed at room temperature with more than a million counts under each spectrum recorded in a time of 1 to 2 h. Source correction term and resolution functions were estimated from the lifetime of well-annealed aluminum using the program RESOLUTION [17]. Since single Gaussian resolution function did not yield convergence,

the resolution function was resolved further into three Gaussian components, which produced quick and good convergence. The net resolution function, however, for this remained at 220 ps. The compliancy of the resolution function was tested with well characterized polymer samples like PC and PTFE and the results obtained agreed very well with literature reported values. Therefore, three Gaussian resolution functions were used in the present analysis of positron lifetime spectra in all the blends and pure polymer samples. All spectra were analyzed into three lifetime components with the help of the computer program PATFIT-88 [17] with proper source and background corrections. The values of the free volume hole size, V_f in nm³; the number density of the free volume holes I_3 , in percentage and the fractional free volume F_v ; the product of V_f and I_3 was determined from the PALS measurements.

3. Results and discussion

3.1. Characterization of maleated depolymerised natural rubber (MDPR)

3.1.1. Structural characterization of MDPR by FT-IR spectroscopy

The FT-IR spectra of depolymerised natural rubber (DPR) and maleated depolymerised natural rubber

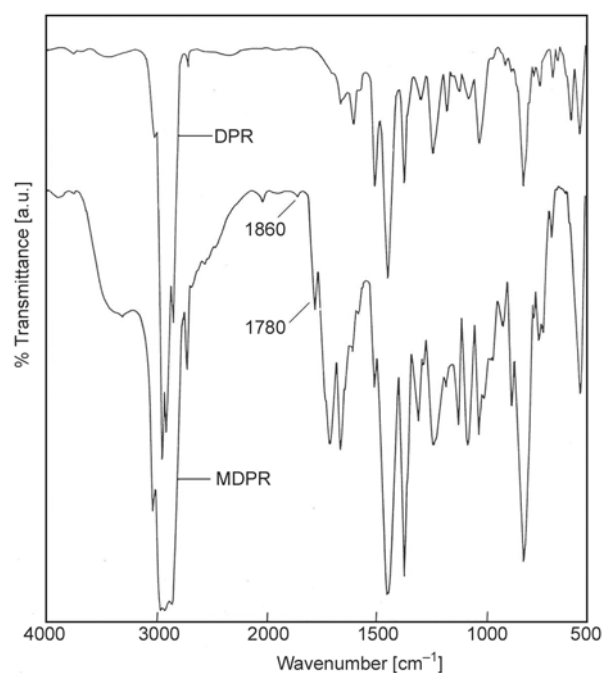


Figure 1. FT-IR Spectra of depolymerised natural rubber (DPR) and maleated depolymerised natural rubber (MDPR)

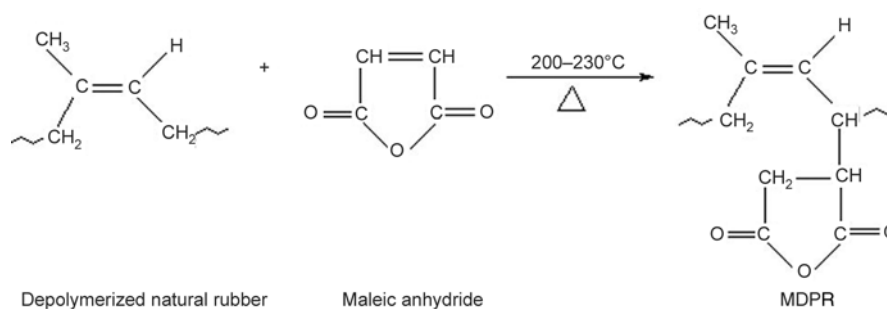


Figure 2. Grafting of maleic anhydride on depolymerised natural rubber (DPR) through Diels-Alder reaction mechanism

(MDPR) are shown in Figure 1. DPR shows the following characteristic peaks at 1640, 885, and 1370 cm^{-1} , for $-\text{C}=\text{C}-$ stretching, $=\text{C}=\text{CH}_2$ (Vinylidene) stretching, and $-\text{CH}_2$ stretching. In the FT-IR spectra of MDPR, the succinic anhydride function has been readily identified by the two absorption bands at 1780 and 1860 cm^{-1} , which suggests the grafting of maleic anhydride on DPR through Diels-Alder mechanism [19]. Derouet *et al.*, modified liquid natural rubber by maleic anhydride through similar type of reaction mechanism [19]. Additionally, another band was identified in the region around 1700 cm^{-1} which characterizes the succinic anhydride ring opening with the formation of carboxylic acid function due the presence of non rubber constituents in the DPR [19]. These characteristic peaks of succinic anhydride and carboxylic acid functions of MDPR were found along with the other characteristic peaks of depolymerised natural rubber. This shows that on reaction of depolymerised natural and maleic anhydride there is no loss in unsaturation or change in the *cis-trans*-ratio of depolymerised natural rubber. This finding is in line with the results reported by Nauton [20]. From Equation (1), the percentage grafting of maleic anhydride has been calculated to be around 1.8%. The plausible reaction between depolymerised natural rubber and maleic anhydride through Diels-Alder mechanism is given in Figure 2.

3.1.2. Structural characterization of MDPR by $^1\text{H-NMR}$ spectroscopy

In the $^1\text{H-NMR}$ spectra of MDPR, fixation of maleic anhydride on DPR was characterized by a chemical shift at $\delta H = 2.3\text{--}2.8$ ppm, which characterizes the protons on the succinic ring and confirms the grafting of maleic anhydride on DPR, through Diels-Alder mechanism [19]. The $^1\text{H-NMR}$

spectrum of MDPR was compared with the $^1\text{H-NMR}$ spectrum of depolymerised natural rubber available in literature [21]. The assignment of various $^1\text{H-NMR}$ peaks of depolymerised natural rubber are, 8.0 τ -which characterizes the methylene protons [$-\text{CH}_2-\text{C}(\text{CH}_3)=\text{CH}-\text{CH}_2-$] on NR and 8.33 τ -which characterizes the *cis* double bond methyl protons [$-\text{C}(\text{CH}_3)=\text{CH}-$] on NR [22].

3.2. Characterization of reactions between epoxy resin and MDPR

3.2.1. FT-IR spectrum of uncured Epoxy/MDPR blends

The FT-IR spectra of the neat epoxy (E0) and Epoxy/MDPR blend (E3) are shown in Figure 3. While blending MDPR with liquid epoxy resin, the secondary alcohol groups present in the epoxy resin (1297 cm^{-1}) can open the anhydride ring of MDPR leading to the formation of ester and carboxyl groups. This reaction is supported by the occurrence of a characteristic peak of saturated ester ($\text{C}=\text{O}$) at 1735 cm^{-1} . The plausible reaction between

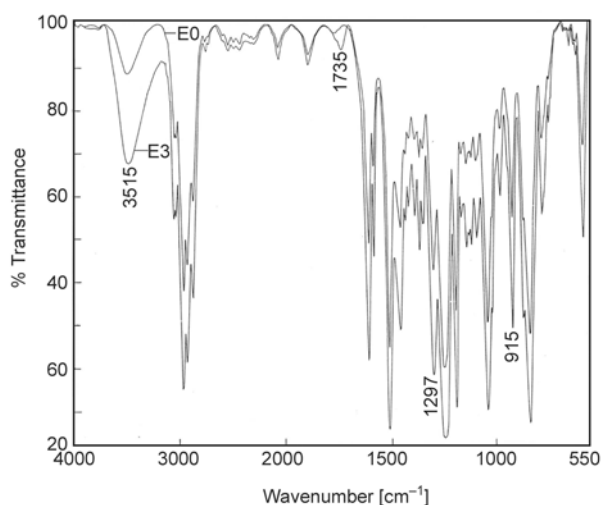


Figure 3. FT-IR Spectra of the uncured samples E0 and E3

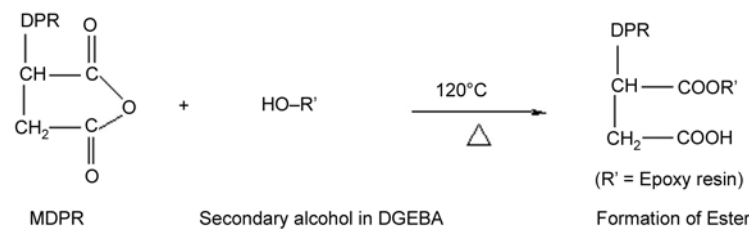


Figure 4. Reaction between maleated depolymerised natural rubber (MDPR) and secondary alcohol group of epoxy resin

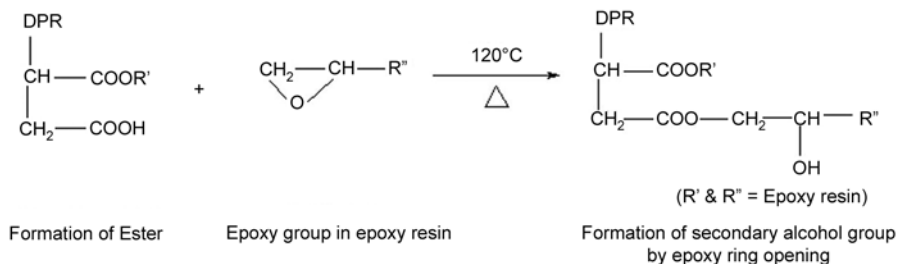


Figure 5. Reaction between the carboxyl group of maleated depolymerised natural rubber (MDPR) and the epoxy group of epoxy resin

MDPR and epoxy resin is shown in Figure 4. The carboxyl group formed will further react with the epoxide group of the epoxy resin leading to the formation of new secondary alcohol groups. This reaction is shown in Figure 5.

Another possible reaction is, some of the anhydride ring in the MDPR must have been opened and converted in to carboxyl groups by the impurities like non rubber constituents. Generally, in maleic anhydride grafted natural rubber, some of the anhydride rings has a tendency to break and get converted in to carboxyl groups. This type of reaction is believed to happen due to the impurities like non rubber constituents in the DPR [19]. While blending Epoxy/MDPR the carboxyl groups in the MDPR can react with the epoxide group of the epoxy resin, leading to the formation of new secondary alcohol groups. This reaction is shown in Figure 6.

By the above two possible mechanisms, maleated depolymerised natural rubber (MDPR) can be

attached to the epoxy backbone to some extent. The FT-IR spectra of the Epoxy/MDPR blend (E3) (Figure 3) elucidate the reaction between the MDPR and the epoxy resin. In the FT-IR spectra of the uncured Epoxy/MDPR blends, after the reaction of MDPR with epoxy resin, there is a decrease in the epoxide band intensity at 915 cm^{-1} with the concomitant increase in secondary alcohol band intensity and free alcohol band intensity at 1297 and 3500 cm^{-1} respectively when compared to the FT-IR spectra of the uncured neat epoxy resin. This confirms the reaction between the acid/anhydride groups of MDPR and the epoxide group of the epoxy resin which results in the formation of secondary alcohol groups. The reaction schemes between MDPR and epoxide group of epoxy resin has been established by calculating the areas of epoxide peak at 915 cm^{-1} , secondary alcohol peak at 1297 cm^{-1} and aromatic group peak at 1500 cm^{-1} in the respective FT-IR spectra of the uncured neat epoxy (E0) and Epoxy/MDPR blend (E3). The

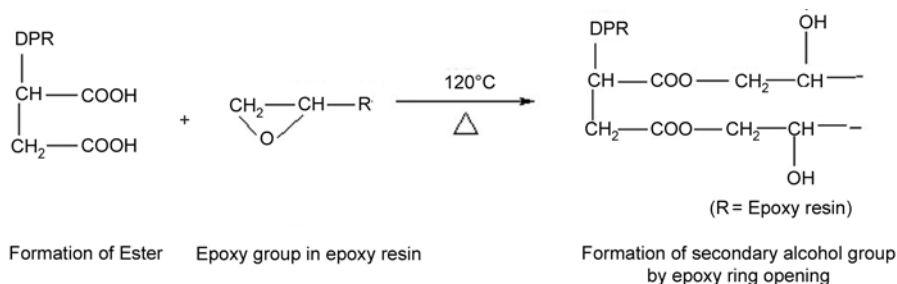


Figure 6. Reaction between the carboxyl groups of maleated depolymerised natural rubber (MDPR) and the epoxy group of epoxy resin

ratios of epoxide peak area to aromatic peak area, secondary alcohol peak area to aromatic peak area were calculated from the respective FT-IR spectrums. From these ratio values the reaction schemes between MDPR and Epoxy resin has been predicted.

3.3. Thermal analysis

Figure 7 shows the DSC traces of neat epoxy resin and Epoxy/MDPR blends. The glass transition temperature (T_g) values of cured neat epoxy and Epoxy/MDPR blends are included in Table 1. Addition of MDPR to epoxy resin does not produce

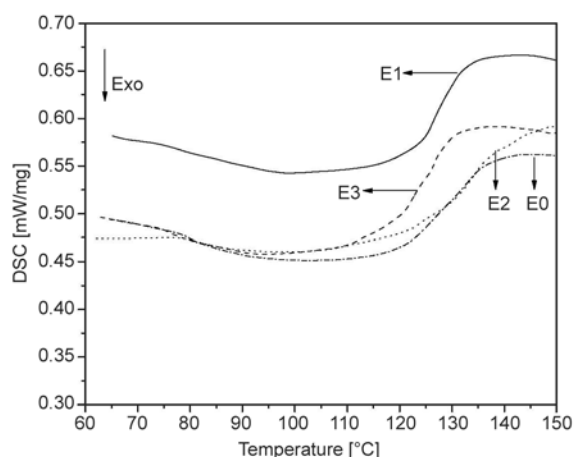


Figure 7. DSC traces of cured samples E0, E1, E2 and E3

Table 1. Glass transition temperature (T_g) and free volume parameters for the neat and the modified epoxies

Modifier (PHR)	Free volume hole size V_f [nm ³]	o-Ps intensity I_3 [%]	$F_{VR}(\%) = V_f \cdot I_3$	T_g [°C]
Nil (E0)	5.92	24.1	1.427	125
MDPR(1) (E1)	6.01	24.0	1.442	122
MDPR(2) (E2)	6.22	23.8	1.480	128
MDPR(3) (E3)	5.92	24.8	1.468	120

Table 2. Tensile, flexural and impact properties of the samples E0, E1, E2 and E3

Tensile properties	Sample designation	Tensile strength [MPa]	Tensile modulus [GPa]	Elongation @ break [%]
	E0	65	1.20	4.8
	E1	63	0.99	5.4
	E2	62	0.91	5.7
	E3	61	0.90	5.6
Flexural properties	Sample designation	Flexural strength [MPa]	Flexural modulus [GPa]	Flexural strain to failure [%]
	E0	126	6.0	2.2
	E1	124	5.9	2.8
	E2	121	5.4	2.6
	E3	120	5.0	2.6
Impact properties	Sample designation	Impact strength [J/m ²]		
	E0	70		
	E1	110		
	E2	130		
	E3	90		

and significant change in the T_g value of the neat epoxy resin. This can be attributed to the limited compatibility between the blend components. Generally, in the case of more miscible epoxy-liquid rubber systems, the glass transition region will be broader [4, 23]. Here, the glass transition region is very narrow indicating a very limited compatibility between the blend components and also clearly suggest a possibility of distinct phase separation. In this case, the hardener was mixed with liquid epoxy resin at 80°C and the mould was kept in the oven at 100°C. This would have given more time for gelation. However, at a higher temperature the viscosity will be much less and the reaction between epoxy and the hardener would be faster, and phase separations of the smaller particles will be more efficient. It must be remembered that as the epoxy starts curing, the rubber will precipitate faster thus, more efficient phase separation but with smaller precipitated rubber particles can be obtained. This prediction is confirmed and explained in detail in the later section on the morphological studies of the Epoxy/MDPR blends.

3.4. Mechanical properties

The tensile strength, tensile modulus, elongation at break [%]; flexural strength, flexural modulus and

flexural strain to failure [%] values of the cured neat epoxy and Epoxy/MDPR blends are reported in Table 2. As expected, the addition of MDPR results in the reduction of the tensile strength, tensile modulus, flexural strength and flexural modulus. This is perhaps due to the dissolution of the epoxy resin matrix by the addition of the any liquid rubber [24, 25]. However, elongation at break and flexural strain to failure percentage values of the Epoxy/MDPR blends are higher than those of the neat epoxy resin. This shows that the rubber modified epoxy has undergone higher percentage of strain (ductile deformation) before failure, which will significantly contribute in enhancing the toughness property of the epoxy resin. This is further supported by the SEM micrographs of Epoxy/MDPR blends, which is shown in the next section. In line with this, the impact strength values of Epoxy/MDPR blends are higher than that of the unmodified epoxy (Table 2). The impact strength of neat epoxy increases with the increase in loading

of MDPR up to 2 weight percentage and decreases at 3 weight percentage of MDPR concentration. The reason for this behavior has been explained in detail in the next section by considering the phase separation effect of the MDPR in the epoxy matrix.

3.5. Fractography

The SEM photomicrographs of the tensile fractured neat epoxy and Epoxy/MDPR blends are shown in Figure 8a–d. The SEM photo micrographs of Epoxy/MDPR blends show the distribution of globular rubber particles in the epoxy matrix. In the case of sample E1 and E2 the dispersed rubber particles have dimension in the range of 1–6 μm and the rubber particles are uniformly distributed throughout the epoxy matrix. However, in the case of sample E3 the size of the dispersed rubbery domains are much larger and the rubbery particles are not uniformly distributed throughout the epoxy matrix. In the micrographs of samples E1 and E2,

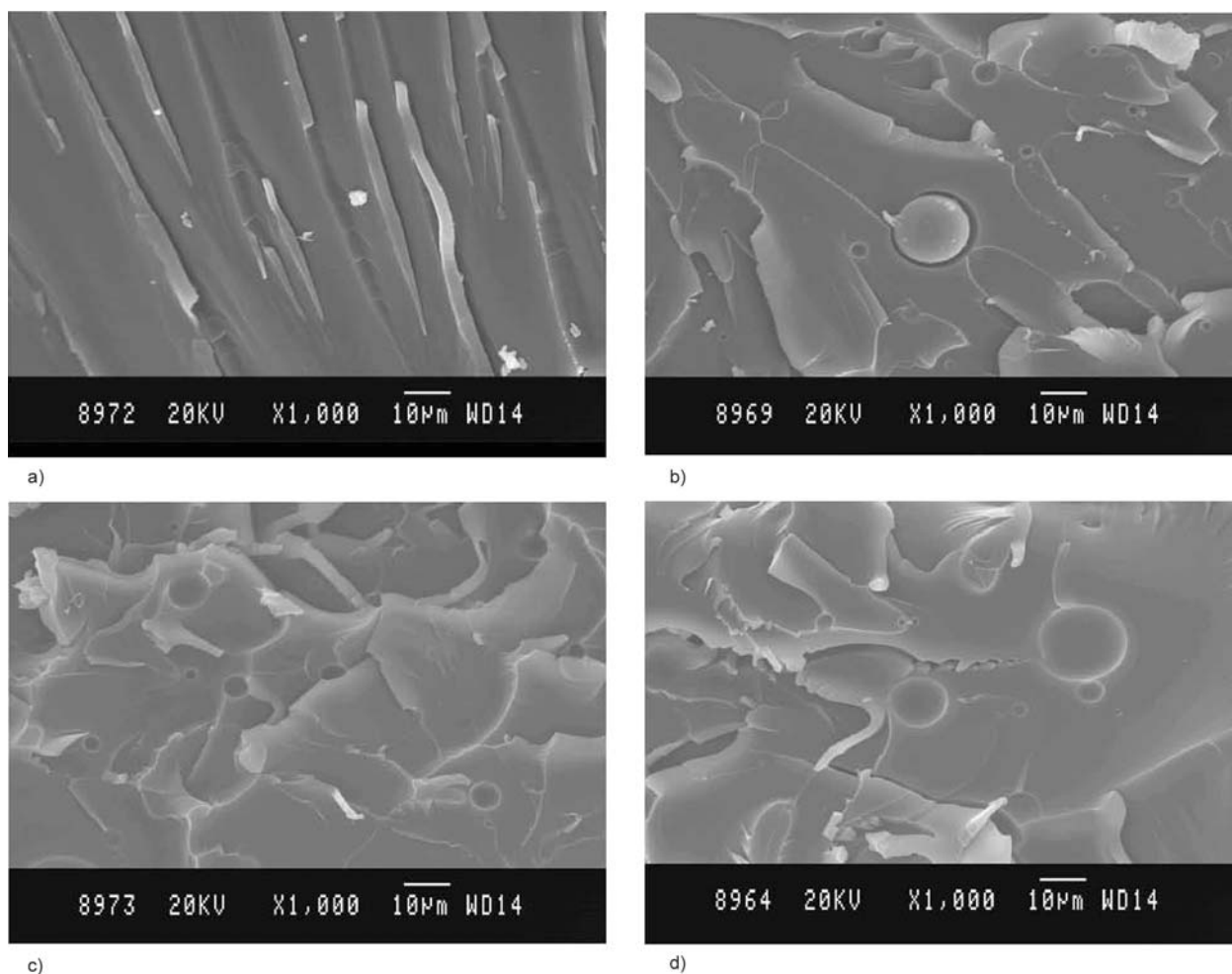


Figure 8. SEM micrograph of fractured surface of sample E0 (a), SEM micrograph of fractured surface of sample E1 (b), SEM micrograph of fractured surface of sample E2 (c), SEM micrograph of fractured surface of sample E3 (d)

one can see shear banding between the rubber particles, which suggest appreciable matrix shear yielding and plastic deformation over a large volume. This is the primary cause for energy absorption mechanism in the case of rubber-toughened epoxy [24–27]. However, this effect is more prominently seen in the case of sample E2. Hence for sample E2, both toughening and flexibilisation effects (mild dilution effect of the epoxy matrix) can be operative, resulting in maximum improvement in impact strength. In the case of neat epoxy resin, there is no evidence of any ductile fracture process (matrix shear yielding) which further substantiates the brittle nature of the fracture process. The poor fracture property of sample E3 can also be explained by considering the morphology as observed in the SEM. The SEM photograph indicates the presence of large particles distributed haphazardly. The larger particles cannot act efficient in dissipating mechanical energy but instead act as defects [25, 26].

3.6. Positron annihilation lifetime studies (PALS)

The data from PALS gives the following information of interest for studies of this type – values of free volume hole size, V_f in nm^3 , I_3 in % which is a measure of the number density of the free volume holes. The product of these two parameters is F_v , which gives the overall fractional free volume. The values of these parameters for the samples E0, E1, E2 and E3 are reported in Table 1. Elongation at break and toughness depend on free volume parameters. They depend on the ease with which the polymer chains can slide past each other under load. Thus increase in V_f values can be expected to provide more space for the chain movements—thus elongation at break increases with modifier content upto 2 phr levels. Since the level of addition of the modifier is very low, the changes in these properties are not dramatic. The V_f and F_v values show the same trend with the level of modifier addition. However, the effect of modifier addition on, I_3 values show a different trend – a slight decrease in these values with modifier addition upto 2 phr addition – this may be due to cross linking of the resin by the modifier – as each anhydride group can react with two epoxy rings. The probability of this reaction is good at high temperature cure as is the case

here – at higher temperatures, the resin has lower viscosity and this can help in the anhydride group in the modifier to react with new epoxy rings in other chains leading to cross linking. At 3 phr level the I_3 value increases – this may be due to the additive effect of the modifier (here a rubbery oligomer) which should have more free volumes compared with the epoxy resin. The glass transition temperature (T_g) values also reflect the trend shown by the free volume parameters.

4. Conclusions

Maleated depolymerised natural rubber (MDPR) has been developed by grafting maleic anhydride with depolymerised natural rubber. The FT-IR spectrum and $^1\text{H-NMR}$ spectroscopy of the MDPR confirms the grafting and explains the reaction mechanism between maleic anhydride and depolymerised natural rubber. The FT-IR spectra of the uncured Epoxy/MDPR blends confirm the reactions between the acid/anhydride moiety of MDPR and the epoxy group of the epoxy resin. The addition of MDPR to epoxy resin does not significantly alter the glass transition temperature (T_g) value of the neat epoxy resin. This is attributed to the limited compatibility between MDPR and epoxy resin. The addition of MDPR to epoxy resin results in an increase in the elongation at break and flexural strain to failure values with some expense in other mechanical properties. The unnotched Izod impact strength values of the 99/1 (E1) and 98/2 (E2) Epoxy/MDPR blends are higher than impact strength value of the unmodified epoxy (E0). However, the impact strength value of 97/3 (E3) blend is lower than the impact strength values of 99/1 (E1) and 98/2 (E2) blends. The SEM micrographs of 99/1 (E1) and 98/2 (E2) blends show shear banding between the uniformly phase separated rubber particles, which advocate appreciable matrix shear yielding and plastic deformation over a large volume. This is attributed to the improvement of the impact strength values of the 99/1 (E1) and 98/2 (E2) Epoxy/MDPR blends. However, in the case of 97/3 (E3) blend, though there is phase separation, the rubber particles are phase separated randomly with irregular particle size. This may explain the poor performance of the 97/3 (E3) blend system. PALS show the usual increase in free volume parameters with the addition of the rubbery modi-

fier but the number density of the free volume holes show a decrease upto 2 phr level addition of the modifier – this may be due to some cross linking between the resin chains by the maleic anhydride group present in the modifier. These trends are reflected by the glass transition (T_g) values measured by differential scanning calorimetry.

Acknowledgements

The authors acknowledge M/S.Carborundum Universal India Private Limited for providing Depolymerised Natural Rubber.

References

- [1] Potter W. G.: Epoxide resins. Springer-Verlag, New York (1970).
- [2] May C. A.: Epoxy resins: Chemistry and technology. Marcell Dekker, New York (1973).
- [3] Bouer R. S.: Epoxy resin chemistry. American Chemical Society, Washington (1979).
- [4] Bascom W. D., Hunston D. L.: Rubber toughened plastics. American Chemical Society, Washington (1989).
- [5] McGarry F. J., Rosner R. B.: Epoxy-rubber interactions. in 'Toughened plastics I. Science and Engineering' (eds.: Riew C. K., Kinloch A. J.) Advances in Chemistry Series, Washington, 305–315 (1993).
- [6] Sultan J. N., McGarry F. J.: Effect of rubber particle size on deformation mechanisms in glassy epoxy. *Polymer Engineering and Science*, **13**, 29–34 (1973).
- [7] Manzione L. T., Gillham J. K., McPherson C. A.: Rubber-modified epoxies, I. Transitions and morphology. *Journal of Applied Polymer Science*, **26**, 889–905 (1981).
- [8] Manzione L. T., Gillham J. K.: Rubber-modified epoxies, II. Morphology and mechanical properties. *Journal of Applied Polymer Science*, **26**, 907–919 (1981).
- [9] Riew C. K.: Amine terminated reactive liquid polymers: Modification of thermoset resins. *Rubber Chemistry and Technology*, **54**, 374–402 (1981).
- [10] Pocius A.: Elastomer modification of structural adhesives. *Rubber Chemistry and Technology*, **58**, 622–636 (1985).
- [11] Reizaifard A. H., Hodd K. A., Tod D. A., Barton J. M.: Toughening epoxy resins with poly (methyl methacrylate)-grafted-natural rubber, and its use in adhesive formulations. *International Journal of Adhesion and Adhesives*, **14**, 153–159 (1994).
- [12] Kemp T. J., Wiford A., Howarth O. W., Lee T. C. P.: Structural and materials properties of a polysulphide-modified epoxide resin. *Polymer*, **33**, 1860–1871 (1992).
- [13] Tong J., Bai R., Pan C., Goethals E. J.: Flexibility improvement of epoxy resin by using polysiloxane-PGMA (MMA) composite particles. *Journal of Applied Polymer Science*, **57**, 895–901 (1995).
- [14] Ratna D., Banthia A. K.: Rubber toughened epoxy. *Macromolecular Research*, **12**, 11–21 (2004).
- [15] Suzuki T., Oki Y., Numajiri M., Miura T., Kondo K., Ito Y.: Positron annihilation and polymerization of epoxy resins. *Polymer*, **34**, 1361–1365 (1993).
- [16] Mogensen O. E., Jacobsen F., Pethrick R. A.: Positron annihilation in a rubber modified epoxy resin. *Polymer*, **20**, 1034–1036 (1979).
- [17] Goyanes S., Rubiolo G., Salgueiro W., Somoza A.: On the free volume evolution in a deformed epoxy composite. A positron annihilation study. *Polymer*, **46**, 9081–9087 (2005).
- [18] Goyanes S., Rubiolo G., Marzocca A., Salgueiro W., Consolati G., Somoza A., Mondragon I.: Yield and internal stresses in aluminum filled epoxy resin. A compression test and positron annihilation analysis. *Polymer*, **44**, 3193–3199 (2003).
- [19] Derouet D., Phinyocheep P., Boccaccio G., Brosse J. C.: Synthesis of photo-crosslinkable elastomers by chemical modification of liquid natural rubber. *Journal of Natural Rubber Research*, **6**, 39–54 (1991).
- [20] Naunton W. J. S.: Applied science of rubber. Edward Arnold Publishing, London (1961).
- [21] Roberts A. D.: Natural rubber science and technology. Oxford University Press, Oxford (1988).
- [22] Brydson J. A.: Rubber chemistry. Applied Science Publishers, London (1978).
- [23] Kothandaraman B., Kulshreshtha A. K.: Rubber modified thermosets. in 'Handbook of polymer blends and composites' (eds.: Vasile C., Kulshreshtha A. K.) Rapra Technology, Shrewsbury, Vol 4, 417–440 (2003).
- [24] Bucknall C. B.: Toughened plastics. Applied Science Publishers, London (1977).
- [25] Kinloch A. J.: Relationship between the microstructure and fracture behavior of rubber-toughened thermosetting polymer. in 'Rubber toughened plastics' (ed.: Riew C. K.) Advances in Chemistry Series, Washington, 67–91 (1989).
- [26] Levita G.: Matrix ductility and toughening of epoxy resins. in 'Rubber toughened plastics' (ed.: Riew C. K.) Advances in Chemistry Series, Washington, 93–118 (1989).
- [27] Banthia A. K., Chaturvedi P. N., Jha V., Pendyala V. N. S.: Synthesis, characterization and evaluation of telechelic acrylate oligomers and related toughened epoxy networks. in 'Rubber toughened plastics' (ed.: Riew C. K.) Advances in Chemistry Series, Washington, 343–359 (1989).